NASA CONTRACTOR REPORT

NASA CR-1491

FEASIBILITY STUDY FOR REMOTE SENSING OF ATMOSPHERIC TURBULENCE PROFILES

by Arthur Peskoff, Robert S. Margulies, and L. Kent Wanlass

Prepared by
TRW INC.
Redondo Beach, Calif.
for Electronics Research Center

NATIONAL AERONAUTICS AND SPACE ADMINISTRATION • WASHINGTON, D. C. • MARCH 1970

FEASIBILITY STUDY FOR REMOTE SENSING OF ATMOSPHERIC TURBULENCE PROFILES

By Arthur Peskoff, Robert S. Margulies, and L. Kent Wanlass

Issued by Originator as Report No. 10636-6001-RO-00

Prepared under Contract No. NAS 12-2023 by
TRW SYSTEMS GROUP
TRW INC.
Redondo Beach, Calif.

for Electronics Research Center

NATIONAL AERONAUTICS AND SPACE ADMINISTRATION

For sale by the Clearinghouse for Federal Scientific and Technical Information
Springfield, Virginia 22151 – Price $3.00

CONTENTS

FEASIBILITY STUDY FOR REMOTE SENSING OF ATMOSPHERIC TURBULENCE PROFILES

by Arthur Peskoff, Robert S. Margulies and L. Kent Wanlass

TRW Systems Group
Redondo Beach, California

SUMMARY

The purpose of this investigation is to perform analytical and experimental studies which will determine the feasibility of a practical implementation of a new technique for the remote sensing of clear-air turbulence profiles. The technique is based on a published mathematical result which demonstrated that the turbulence profile along the line of sight to a plane-wave light source can be calculated uniquely from an integro-differential transform of the correlation function of the logarithmic-amplitude fluctuations of light which has propagated through the turbulence.

A computer program has been developed, which performs the mathematical inversion transform. Numerical calculations to simulate a practical application of the technique are accomplished by applying the inversion formula to the correlation function of a delta-function turbulence profile.

By cutting off the inversion integral at a finite value we simulate the inability to measure correlation functions for spatial separations greater than some finite value. We find that the spatial resolution of the inversion procedure is inversely proportional to the square of the maximum separation, and directly proportional to the square of the distance to the turbulence layer. By varying the number of terms in the summation approximation which the computer program makes for the inversion integral, we simulate the effect of varying the number of points at which the correlation function is sampled in an actual measurement.

The correlation function is calculated for a family of continuous turbulence profiles, and inverted using the above inversion program.

An analytic expression is derived relating the mean-square error in the calculated turbulence profile to the mean-square error in a measured correlation function. The expression is used to calculated the logarithmic-intensity sample size required to keep the error in the computed profile below some tolerable value.

An experiment has been set up to verify the theoretical predictions. The apparatus consists of an artificial turbulence source, a pulsed laser beam which propagates through the turbulence, and a system for photographically recording and scanning the random diffraction pattern induced in the beam.

I. INTRODUCTION

The present study is an evaluation of a passive optical technique for detecting, ranging and determining the strength of clear-air turbulence at an arbitrary separation from an observer. The basis of the technique is a mathematical inversion[1] of the formula[2] for the correlation function of the fluctuations of the logarithmic amplitude of light which has passed through turbulence. The light may be from a star or other plane-wave source. Utilizing the inversion, the profile of turbulence along the line of sight to the light source can be determined uniquely by taking an integro-differential transform of the correlation function. If the correlation function could be obtained exactly, the turbulence profile could be calculated exactly. In practice, however, an actual measurement of the correlation function contains noise. The purpose of our investigation is to determine the degradation of the calculated turbulence profile caused by practical limitations on the measurement of the correlation function. In addition, we are setting up an experiment to verify the inversion technique under controlled laboratory conditions.

In an application of the method to the remote sensing of atmospheric turbulence, the simplest method of obtaining the correlation function is by using an array of small-aperture telescopes, which are each aimed at the same star. The time history of the intensity measured by a photomultiplier at the output of each telescope is passed through a logarithmic amplifier and recorded on magnetic tape. The logarithmic-intensity recordings from a pair of telescopes are then correlated electronically by multiplying the two signals and averaging over their time duration. This yields the value of the correlation function corresponding to the separation of the two telescopes. The multiplication and averaging is then repeated for all possible pairs of telescopes to obtain the correlation function at all possible separations available in the given array of telescopes. The measured correlation function, thus obtained, can then be inverted by a digital computer programmed to perform the appropriate integro-differential transform. The result is the profile of turbulence along the line of sight to the star.

The correlation function is maximum for zero separation (i.e., correlation of the signal from one telescope with itself) and then decreases in magnitude as the separation between telescopes increases. Beyond a certain spatial separation, noise in the measurement overshadows the correlation function, and no useful data can be obtained. Thus, in practice, the correlation function can be obtained only for separations from zero to some maximum, finite value. In this report (Sec. III) we present the results of our study of the effect of this finite cutoff, and find that it limits the spatial resolution in the calculated profile. As the maximum separation between telescopes increases, the size of the smallest irregularities in the turbulence profile that can be seen decreases. The spatial resolution is found to be inversely proportional to the square of the maximum separation.

By the measurement technique described above, the correlation function is only sampled at a finite number of spatial separations, rather than continuously. We have therefore investigated the dependence of the calculated profile on the number of sample points.

There will be random noise present in any measured correlation function. It arises from such causes as unwanted stars and stray light in the field of view, instrument noise, and the error introduced because in practice the time averages to obtain the correlation function are performed over a finite sample of the intensity (rather than an infinite sample). We have derived the general relation between the mean-square noise in the correlation function and the resultant mean-square noise in the calculated profile. This allows us to determine the precision requirements on the correlation function measurement for a given desired precision in the calculated profile. We have applied the noise relation thus far to determine the size of the intensity sample required. In the device outlined above, for example, we have found the time interval necessary for recording the intensity.

We are performing a laboratory experiment in which artificial turbulence is generated in a wind tunnel by placing a heated-wire grid in the flow. A pulsed-laser beam propagates through the turbulence (normal to the flow). The logarithmic intensity in a cross section of the beam is recorded on a

photographic plate, after propagating approximately ten meters beyond the turbulence. The correlation function will be obtained by performing a spatial average over the area of the photograph (instead of the time average in the example above) and subsequently averaging over a number of photographs.

We now present a brief outline of the mathematical background which is the basis for the remote turbulence sensing technique. The reader is referred to References 1 and 2 for more datails.

The correlation function of the fluctuations of the logarithmic amplitude of the wave is defined by

$$B_\chi(\rho) = \left\langle \left[\chi(\vec{r}, t) - \langle\chi\rangle\right] \left[\chi(\vec{r} + \vec{\rho}, t) - \langle\chi\rangle\right] \right\rangle, \tag{1.1}$$

where

$$\chi(\vec{r}, t) = \frac{1}{2} \ell n\, I(\vec{r}, t) \tag{1.2}$$

is the logarithmic amplitude of the wave of intensity $I(\vec{r}, t)$, at position $\vec{r}$ in a plane perpendicular to the propagation direction. The angular brackets denote an average, which may be either an ensemble average, an average over $\vec{r}$, or an average over the time, t. For a plane wave and isotropic turbulence, the correlation function (1.1) depends only on the magnitude $\rho = |\vec{\rho}|$.

The theory relating the correlation function for a plane wave to the turbulence through which the wave has propagated has been given by Tatarski[2]. He describes the statistical fluctuations of the index of refraction, $n(\vec{r}, t)$, by defining the structure function

$$D_n(\vec{\rho}, \vec{r}, t) = \left\langle [n(\vec{r}, t) - n(\vec{r} + \vec{\rho}, t)]^2 \right\rangle. \tag{1.3}$$

The structure function (1.3) is assumed to be a relatively slowly varying function of $\vec{r}$ (compared to its functional dependence on $\vec{\rho}$) and hence is expressible as the product of a function of $\vec{r}$ and a function of $\vec{\rho}$. For the special case of Kolmogorov turbulence (which usually exists in the atmosphere[1, 2]), the structure function has the form

$$D_n(\rho, \vec{r}) = C_n^2(\vec{r})\, \rho^{2/3} \text{ for } \ell_o << \rho << L_o, \tag{1.4}$$

where $C_n^2(\vec{r})$ is the "structure constant," and ℓ_o and L_o are, respectively, the smallest and largest turbulent eddy sizes. The turbulence is isotropic in this case, and hence D_n is a function of $\rho = |\vec{\rho}|$. The spectral density of the refractive-index fluctuations is related to the structure function, in the isotropic case, by the transform[2]

$$D_n(\rho, \vec{r}) = 8\pi \int_0^\infty \left(1 - \frac{\sin \kappa\rho}{\kappa\rho}\right) \Phi_n(\kappa, \vec{r}) \kappa^2 d\kappa , \qquad (1.5)$$

and $\Phi_n(\kappa, \vec{r})$ may be written as a product

$$\Phi_n(\kappa, \vec{r}) = C_n^2(\vec{r})\, \Phi_n^{(0)}(\kappa) . \qquad (1.6)$$

If the functional dependence of $\Phi_n^{(0)}(\kappa)$ on the turbulence wavenumber is known, the nature of the turbulence at any spatial location $\vec{r}$ is completely determined by the structure constant $C_n^2(\vec{r})$, which will henceforth be referred to simply as the turbulence profile.

In the special case when the structure function of the index fluctuations is given by Eq. (1.4), the κ-dependence of the spectral density may be found, by using Eq. (1.5), to be[2]

$$\Phi_n^{(0)}(\kappa) = \frac{\sqrt{3}}{8\pi^2} \Gamma\left(\frac{8}{3}\right) \kappa^{-11/3} , \text{ if } 2\pi L_o^{-1} << \kappa << 2\pi \ell_o^{-1} . \qquad (1.7)$$

Using the Rytov perturbation solution of the wave equation, and the statistical functions defined in Eqs. (1.3), (1.5) and (1.6), Tatarski has shown that the correlation function for the fluctuations in the logarithmic amplitude of the electromagnetic wave (1.1) may be expressed as the following double integral over z, the distance measured along the propagation path from the observation point, and over κ, the turbulent wave number,[2]

$$B_\chi(\rho) = 4\pi^2 k^2 \int_0^\infty dz\, C_n^2(z) \int_0^\infty \kappa d\kappa\, \Phi_n^{(0)}(\kappa)\, J_0(\kappa\rho) \sin^2\left(\frac{\kappa^2 z}{2k}\right). \qquad (1.8)$$

where k is the wave number of the electromagnetic wave, and z is the coordinate measured from the observation point backwards along the propagation path.

If we define the integrated turbulence profile by

$$S(z) = \int_z^\infty C_n^2(z')dz' , \tag{1.9}$$

then it may be shown by inverting Eq. (1.8), with $\Phi_n^{(0)}$ given by Eq. (1.4), that[2]

$$S(z) = \frac{8\Gamma(\frac{11}{6})z^{-11/6}k^{-1/6}}{\pi\sqrt{3}\,\Gamma(8/3)} \int_0^\infty d\rho\, \rho B_\chi(\rho)\, \mathrm{Im}\left\{e^{i\pi/12}\, F\left(\frac{11}{6}\middle|1\middle|\frac{i\rho^2 k}{4z}\right)\right\}. \tag{1.10}$$

In Eq. (1.10), $F(a|b|w) = {}_1F_1(a|b|w) = M(a|b|w)$ is the confluent hypergeometric (Kummer) function[3].

The convergence of Eq. (1.10) may be improved by subtracting a function $h(\rho)$ from $B_\chi(\rho)$, which has the identical asymptotic behavior as $B_\chi(\rho)$ in the limit $\rho \to \infty$, that is,

$$h(\rho) \sim B_\chi(\rho) \sim -\frac{\sqrt{3}}{32\pi}\Gamma(\tfrac{8}{3})\,\Gamma^2(\tfrac{7}{6}) \int_0^\infty z^2 C_n^2(z)dz\,(\tfrac{\rho}{2})^{-7/3} \tag{1.11}$$

Furthermore, the moment of the turbulence, $\int_0^\infty z^2 C_n^2(z)dz$, which appears in Eq. (1.11) can be related to the correlation function by

$$\int_0^\infty z^2 C_n^2(z)dz = \frac{16\,\Gamma(\frac{5}{6})k^{-1/6}}{\pi\sqrt{3}\,\Gamma(8/3)} \int_0^\infty dz\, z^{-5/6} \int_0^\infty d\rho\, \rho\, B_\chi(\rho)\, \mathrm{Im}$$

$$\left\{e^{i\pi/12}\, F\left(\frac{5}{6}\middle|1\middle|\frac{i\rho^2 k}{4z}\right)\right\}. \tag{1.12}$$

The more rapidly converging form of Eq. (1. 10) is then

$$S(z) = \frac{8\Gamma(\frac{11}{6})z^{-11/6}k^{-1/6}}{\pi\sqrt{3}\ \Gamma(8/3)}\left[\int_0^\infty d\rho\ \rho\ [B_\chi(\rho) - h(\rho)]\ \mathrm{Im}\right.$$

$$\left\{e^{i\pi/12}\ F\left(\frac{11}{6}\ |1|\ \frac{i\rho^2 k}{4z}\right)\right\} + \int_0^\infty d\rho\ \rho\ h(\rho)\ \mathrm{Im}$$

$$\left.\left\{e^{i\pi/12}\ F\left(\frac{11}{6}\ |1|\ \frac{i\rho^2 k}{4z}\right)\right\}\right] \qquad (1.13)$$

The first integral in Eq. (1. 13) and the integral in Eq. (1. 12) converge more rapidly than the integral in Eq. (1. 10). The second integral in Eq. (1. 13) can be calculated to any desired precision because the ρ-dependence of $h(\rho)$ is known exactly. Hence Eq. (1. 13) appears to be more suitable for inverting experimental correlation functions (which can be measured only over a finite range $0 < \rho < \rho_m$) than Eq. (1. 10). We can obtain greater precision for $S(z)$ from $B_\chi(\rho)$ data which is taken over a given range of ρ using Eq. (1. 13) rather than Eq. (1. 10).

The purpose of the current investigation is to evaluate the practicality of using Eq. (1.10) or (1.13) to accomplish remote sensing of turbulence profiles. In Section III, Eqs. (1.10) and (1.13) are applied to the inversion of the correlation function of a delta-function turbulence profile,

$$C_n^2(z) = A\delta(z - z_o). \qquad (1.14)$$

The integrals are carried out numerically, on a CDC 6500 computer, from $\rho = 0$ to a finite value ρ_m. This inversion leads to a turbulence profile which has finite width. The dependence of the width on ρ_m is studied and it is found to vary inversely with ρ_m^2. The integrals are, of course, approximated by sums. The dependence on the number of terms in the sum is studied.

In Section IV, an analytic expression is found for the correlation function corresponding to a particular smooth turbulence profile,

$$C_n^2(z) = \frac{A}{z_o \Gamma(\mu)} \left(\frac{\mu z}{z_o}\right)^{\mu} e^{-\mu z/z_o}. \qquad (1.15)$$

The correlation function is obtained numerically on the CDC 6500 using the power series for the analytic expression, and the inversions of Eqs. (1.10) and (1.13) applied to it. As expected, the integrated profile S(z) is found to converge for much smaller values of ρ_m than in the case of the delta-function profile of Section III.

In Section IV an expression is derived for the mean-square noise in the calculated value of S(z), in terms of the noise in the measured correlation function. The noise in $B_\chi(\rho)$ resulting from performing the averages in Eq. (1.1) over a finite statistical sample is calculated. This result is applied to determine the noise in S(z) from using a finite sample.

Section VI contains a description of the experimental apparatus and data reduction technique used to measure correlation functions in the laboratory. Some partially reduced data are shown.

II. SYMBOLS

A = total area under turbulence profile

$B_\chi(\rho)$ = correlation function of logarithmic amplitude fluctuations

${}^{\ell}B_\chi(\rho)$ = sample of $B_\chi(\rho)$

$C_n^2(z)$ = structure constant or turbulence profile

D = width of turbulence profile

D_n = structure function of refractive index

$F(a\,|b|\,w)$ = confluent hypergeometric (Kummer) function

${}_1F_1(a\,|b|\,w) = F(a\,|b|\,w)$

${}_1F_2(a\,|b, c|\,w)$ = hypergeometric function

$g = \ell n\, C_n^2(z)$

$h(\rho)$ = asymptotic limit of $B_\chi(\rho)$

I = intensity

J_0 = zeroth-order Bessel function

k = wavenumber of electromagnetic wave

L = intensity sample length

L_o = outer scale of turbulence

ℓ_o = inner scale of turbulence

$M(a\,|b|\,w) = {}_1F_1(a\,|b|\,w)$

m = total number of sample points

n = refractive index

$N(\rho)$ = noise in measurement of correlation function

$Q(a, \rho; b, \rho') = \rho\rho'\, \mathrm{Im}\{e^{i\pi/12}\, F(a\,|1|\,i\rho^2 k/4z)\}\, \mathrm{Im}\{e^{i\pi/12}\, F(b\,|1|\,i\rho'^2 k/4z)$

$\vec{r}$ = position vector

$S(z) = \int_z^\infty C_n^2(z')dz'$ = integrated turbulence profile

t = time

T = sample duration

V = velocity of turbulent flow

X, Y = dimensions of photograph

$y = \rho^2 k/4z_o$

z = position measured backwards along line of sight

z_o = distance from observer to maximum of profile

$\alpha = \kappa^2 z_o/k$

Γ = gamma function

$\delta S(z)$ = error in $S(z)$

$\delta(z-z_o)$ = Dirac delta function

$\delta_{j\ell}$ = Kronecker delta

$\xi = \mu z/z_o$

κ = turbulence wavenumber

ν = rms noise amplitude

$\vec{\rho}$ = vector connecting two observation points

$\rho = |\vec{\rho}|$

$\rho_o = (4z_o/k)^{1/2}$

ρ_1 = first zero-crossing of $B_\chi(\rho)$

ρ_m = maximum value of ρ for which $B_\chi(\rho)$ is sampled

$\sigma^2_{B\chi}(\rho, L)$ = variance of ${}^{\ell}B_\chi(\rho)$ for sample length L

$\sigma_s = [<(\delta s)^2>]^{1/2}$ = standard deviation in $s(z)$

$\Phi_n^{(0)}(\kappa)$ = spectral density function of refractivity

$\chi = \frac{1}{2}\ell n\, I$ = logarithmic intensity

III. INVERSION OF THE CORRELATION FUNCTION OF A DELTA-FUNCTION TURBULENCE PROFILE

A. Calculation of the Correlation Function

If $B_\chi(\rho)$ were known precisely, for all values of ρ in the range $0 < \rho < \infty$, the turbulence profile $C_n^2(z)$ could be obtained to any desired precision by a numerical calculation from Eq. (1.10) or (1.13). However, in any actual measurement of $B_\chi(\rho)$, noise will be present, resulting in some error in the turbulence profile which is calculated from the noisy correlation function. In this section we study how Eqs. (1.10) and (1.13) are affected by a deficiency in our measurement of $B_\chi(\rho)$, which will be present in any practical application. We consider here, the effect of obtaining $B_\chi(\rho)$ only in the finite range $0 < \rho < \rho_m$.

Unfortunately, because of the complicated form of Eqs. (1.10) and (1.13) it is not possible to make further progress without resorting to numerical calculations. We can, however, learn a great deal about the detailed properties of Eqs. (1.10) and (1.13) by applying them to the numerical inversion of the correlation function of a delta-function turbulence profile. As a preliminary step, it is first necessary for us to obtain this correlation function, which has never been done previously.

The correlation function of Eq. (1.8), with the Kolmogorov spectral density (1.7), and the delta-function profile (1.14), can be expressed in terms of a confluent hypergeometric function,[5]

$$B_\chi(\rho) = -\frac{3\sqrt{3}}{20}\,\Gamma\left(\frac{8}{3}\right)\Gamma\,\frac{1}{6}\,k^{7/6}z_o^{5/6}\,A\left[\mathrm{Re}\left\{e^{-i7\pi/12}\,F\left(-\frac{5}{6}\,|1|\,\frac{i\rho^2 k}{4z_o}\right)\right\}\right.$$

$$\left. + \frac{3}{5\pi}\,\Gamma\left(\frac{1}{6}\right)\left(\frac{\rho^2 k}{4z_o}\right)^{5/6}\right] \qquad (3.1)$$

This function has been computed on the CDC 6500.

In the range $0 < \rho^2 k/4z_o \leq 10$, the power series was used for the confluent hypergeometric function,[6]

$$F\left(-\frac{5}{6}\middle|1\middle|iy\right) = \sum_{n=o}^{\infty} \frac{\left(-\frac{5}{6}\right)_n}{(n!)^2} (iy)^n, \tag{3.2}$$

where $(a)_n = \Gamma(a+n)/\Gamma(a)$ and $y = \rho^2 k/4z_o$. The summation was carried out to a value of n for which the last term in (3.2) was less than 10^{-3} in magnitude. In the range $10 < \rho^2 k/4z_o < 100$, the asymptotic expansion of the hypergeometric function was used. The leading term in the asympotic expansion of the first term in square brackets in Eq. (3.1) exactly cancels the second term in square brackets. The asymptotic expansion of the bracketed expression in Eq. (3.1) is[7]

$$\frac{-1}{\Gamma\left(\frac{11}{6}\right)} y^{5/6} \sum_{m=1}^{R} \left(-\frac{5}{6}\right)_{2m}^2 \frac{(-y^2)^{-m}}{(2m)!} + \frac{y^{-11/6}}{\Gamma\left(-\frac{5}{6}\right)} \mathrm{Re}\left\{ie^{iy} \sum_{n=o}^{S} \left(\frac{11}{6}\right)_n^2 \frac{(iy)^{-n}}{n!}\right\} \tag{3.3}$$

The first five terms in each summation of (3.3) were used in the calculation. The resulting correlation function is shown in Fig. 1 as a function of the variable $y = \rho^2 k/4z_o$. In the range $\rho^2 k/4z_o > 10$, the curve is magnified by a factor of 100 for clarity.

B. Numerical Inversion Using Eq. (1.6)

The kernel function in Eqs. (1.10) and (1.13), $\mathrm{Im}\{\exp(i\pi/12) F(11/6 \mid 1 \mid i\rho^2 k/4z)_o\}$, is calculated in the same way, from the power series

$$F\left(\frac{11}{6}\middle|1\middle|\frac{i\rho^2 k}{4z}\right) = \sum_{n=o}^{\infty} \left(\frac{11}{6}\right)_n \frac{1}{(n!)^2} \left(\frac{i\rho^2 k}{4z}\right)^n, \tag{3.4}$$

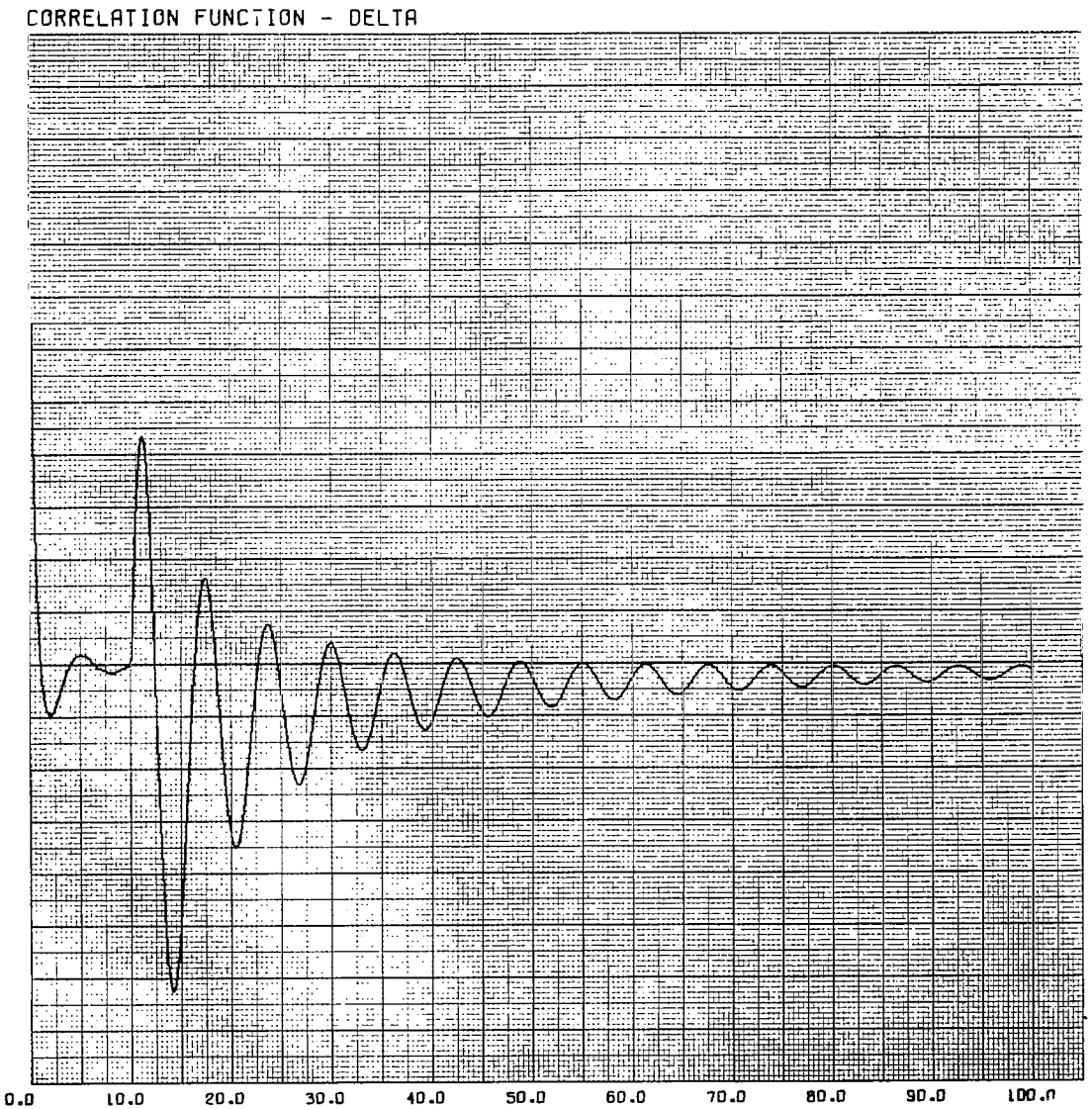

Figure 1. The logarithmic-amplitude correlation function, $B_\chi(\rho)$, for delta-function turbulence, $C_{n_2}^2(z) = A\,\delta(z-z_o)$, versus $\rho^2 k/4z_o$ (vertical scale arbitrary, 100X magnification for $\rho^2 k/4z_o > 10$).

and the asymptotic expansion

$$\mathrm{Im}\left\{ e^{i\pi/12} F\left(\frac{11}{6} \,\middle|\, 1 \,\middle|\, \frac{i\rho^2 k}{4z}\right)\right\} \sim \frac{-1}{\Gamma\left(-\frac{5}{6}\right)} \sum_{m=0}^{R} \frac{(-1)^m}{(2m)!} \left(\frac{11}{6}\right)_{2m}^{2} \left(\frac{\rho^2 k}{4z}\right)^{-2m}$$

$$+ \frac{1}{\Gamma\left(\frac{11}{6}\right)} \left(\frac{\rho^2 k}{4z}\right)^{5/6} \sum_{n=0}^{S} \frac{1}{n!} \left(\frac{-5}{6}\right)_{n}^{2} \left(\frac{\rho^2 k}{4z}\right)^{-n} \mathrm{Im}\left\{ i^{1-n} e^{i\rho^2 k/4z}\right\}. \tag{3.5}$$

The kernel function is shown in Figure 2 as a function of $\rho^2 k/4z$ in the interval $0 \le \rho^2 k/4z < 100$. The function is reduced by a factor of 10 for $\rho^2 k/4z > 10$.

We have carried out the inversion of Eq. (1.10) numerically, utilizing the calculated correlation function (with A = 1 $cm^{1/3}$) and kernel function. This has been done for z/z_o = 0.1, 0.2, 0.4, 0.6, 0.8, 0.9, 0.92, 0.94, 0.96, 0.97, 0.98, 0.99, 1.00, 1.01, 1.02, 1.03, 1.04, 1.06, 1.08, 1.10, 1.20, 2.00, 5.00 and 10.00. For each of these values of z/z_o, the integral (1.10) is carried out from $\rho^2 k/4z_o = 0$ to $\rho^2 k/4z_o = 100$. The integral is calculated by Simpson's rule with 2,001 uniformly spaced points in the interval $0 \le \rho^2 k/4z_o \le 100$.

The argument of the kernel function in Eq. (1.10) runs from $\rho^2 k/4z = 0$ to $\rho^2 k/4z = 100\, z_o/z$, and hence as z/z_o decreases, the kernel function becomes increasingly more oscillatory as a function of the integration variable $y = \rho^2 k/4z_o$. When $z/z_o = 0.1$ (the smallest value used in the numerical inversion), the kernel function is required in the range $0 \le \rho^2 k/4z \le 1000$. The upper curves in Figures 3a-3h show sample results of the computer calculations of the S(z) integral in Eq. (1.10) (with the upper limit ∞ replaced by ρ_m) as a function of $\rho_m{}^2 k/4z_o$, in the range $0 < \rho_m{}^2 k/4z_o < 100$. The horizontal scale printed on the figures is $\rho_m{}^2 k/4z_o$. The right-hand vertical scale corresponds to the upper curves.

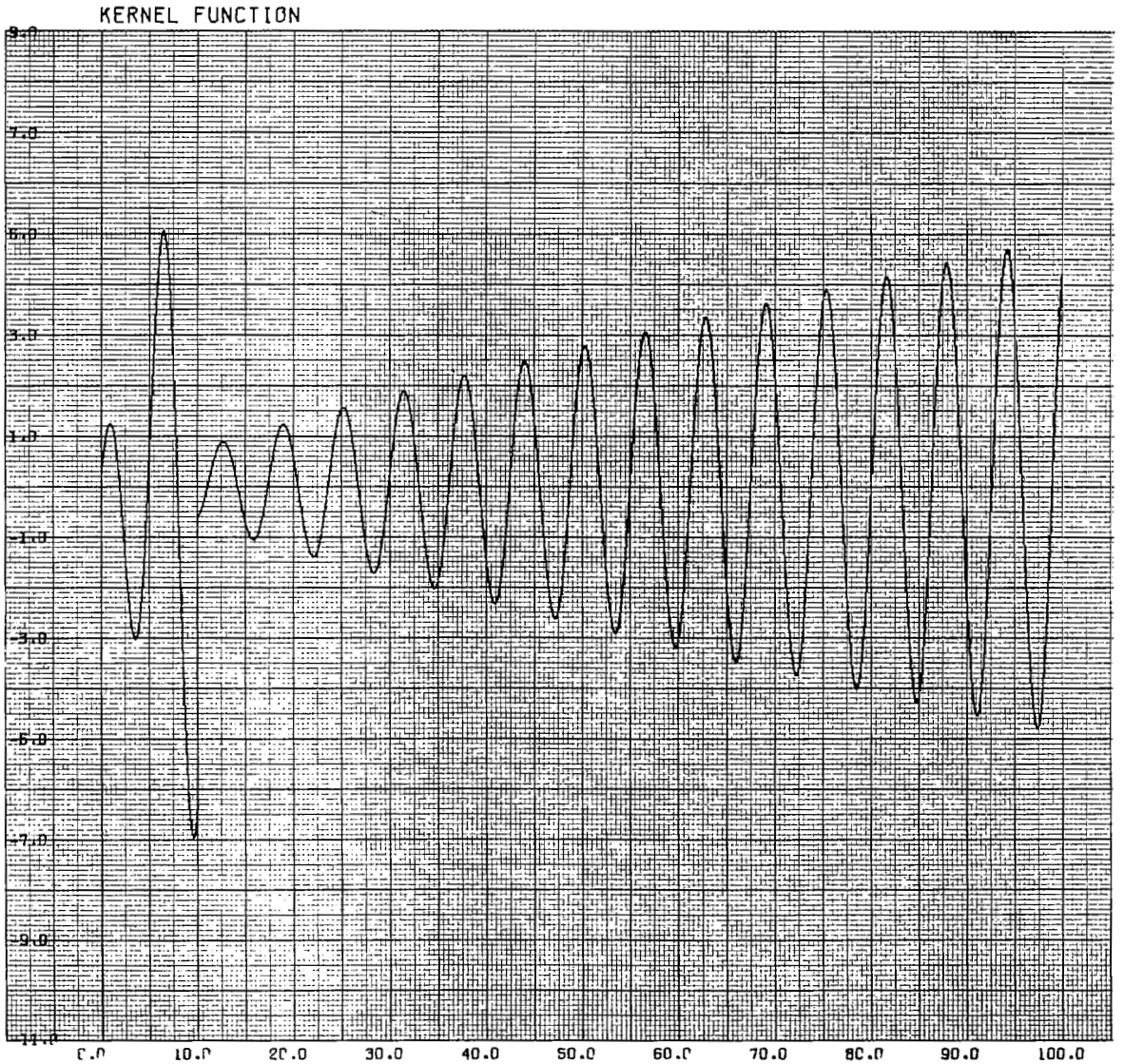

Figure 2. The kernel of the integral transform, Im $\{\exp(i\pi/12)\ F(11/6|1|i\rho^2 k/4z)\}$ versus $\rho^2 k/4z_o$ (1/10 vertical magnification for $\rho^2 k/4z > 10$.

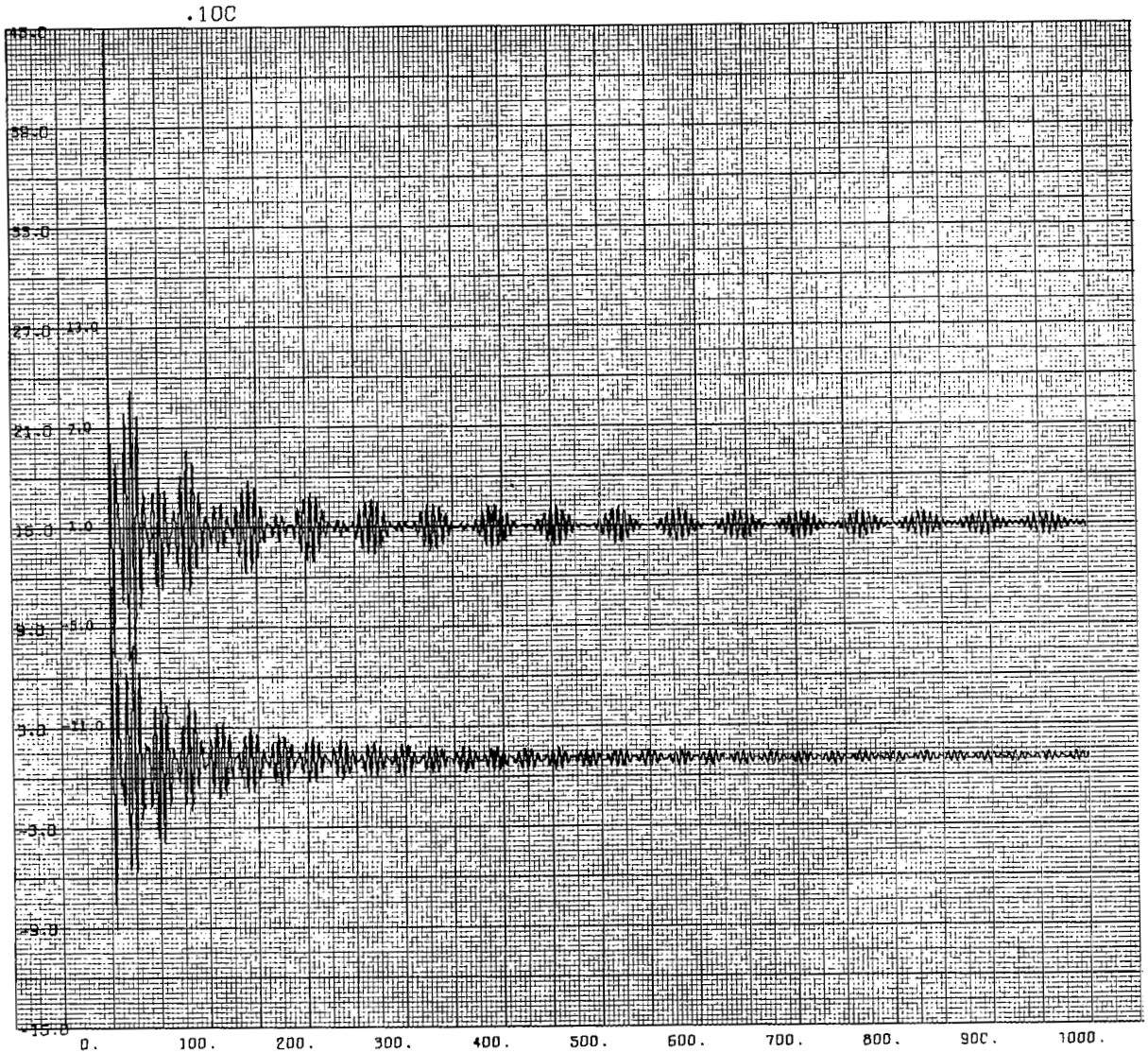

Figure 3. Calculated integrated turbulence profile S(z) for delta-function profile, versus $\rho_m^2 k/4z$. Upper curve is from Eq. (1.6), lower curve from Eq. (3.10). (a) $z/z_o = 0.10$

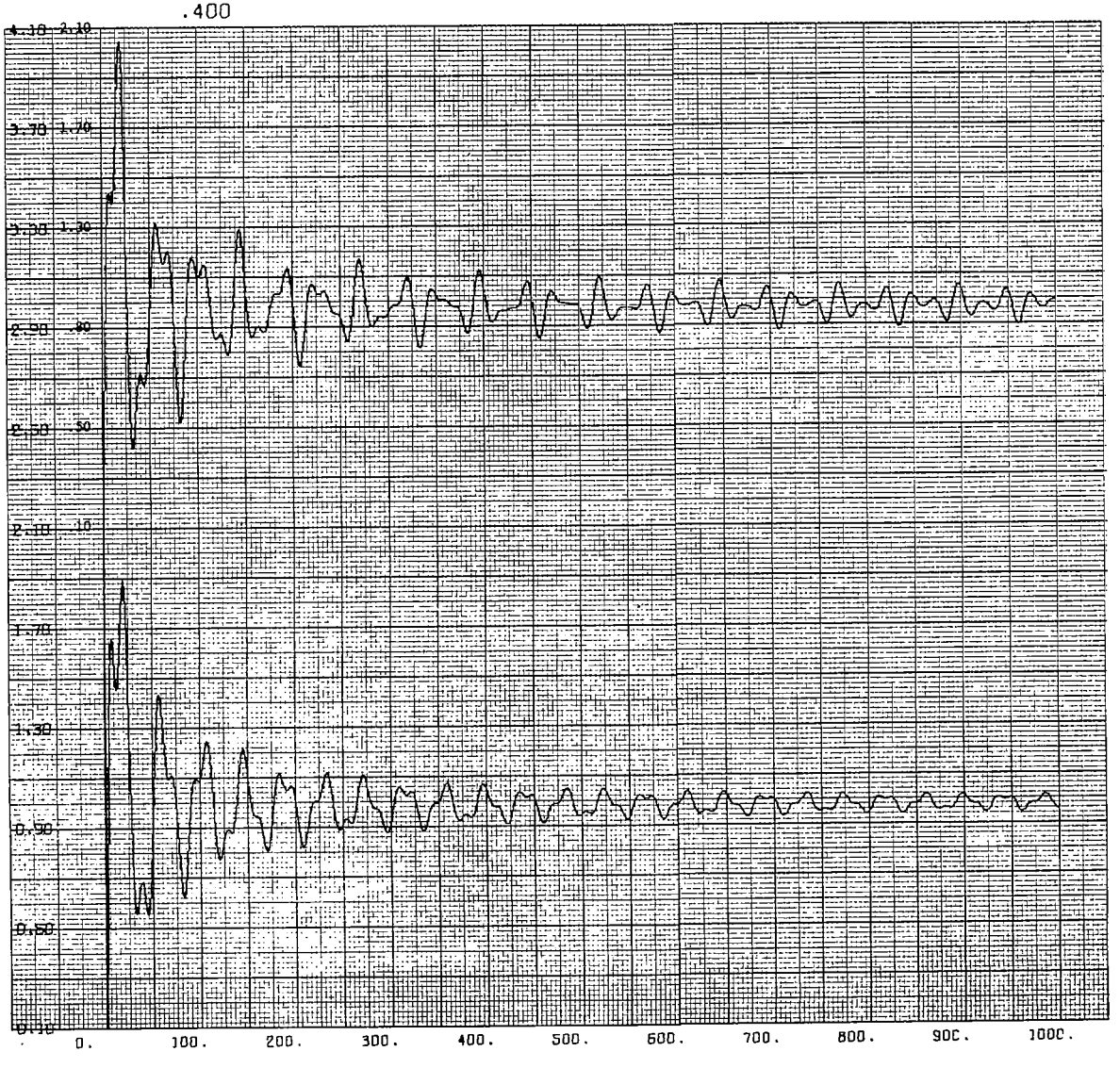

Figure 3b. $z/z_o = 0.40$

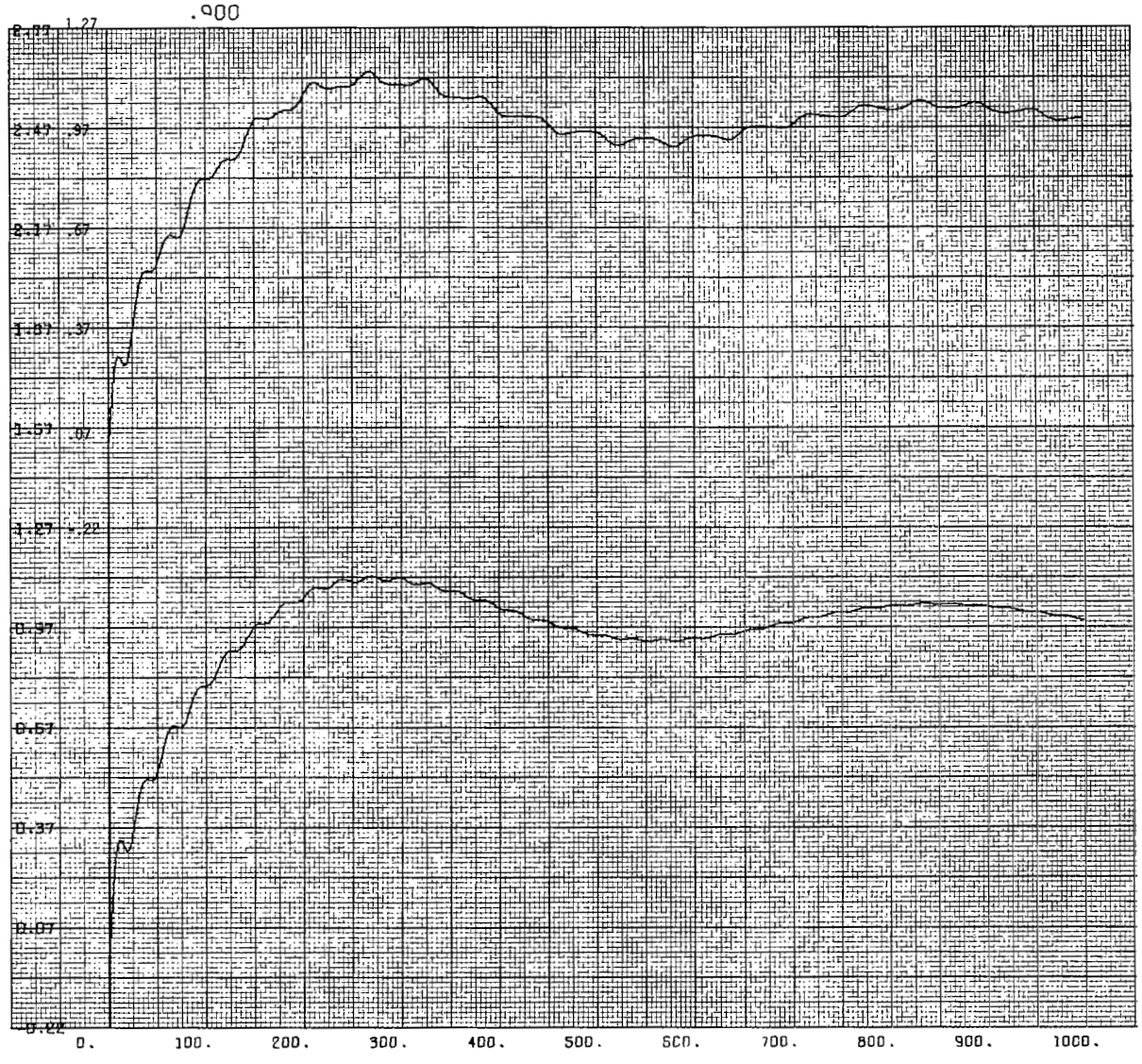

Figure 3c. $z/z_o = .90$

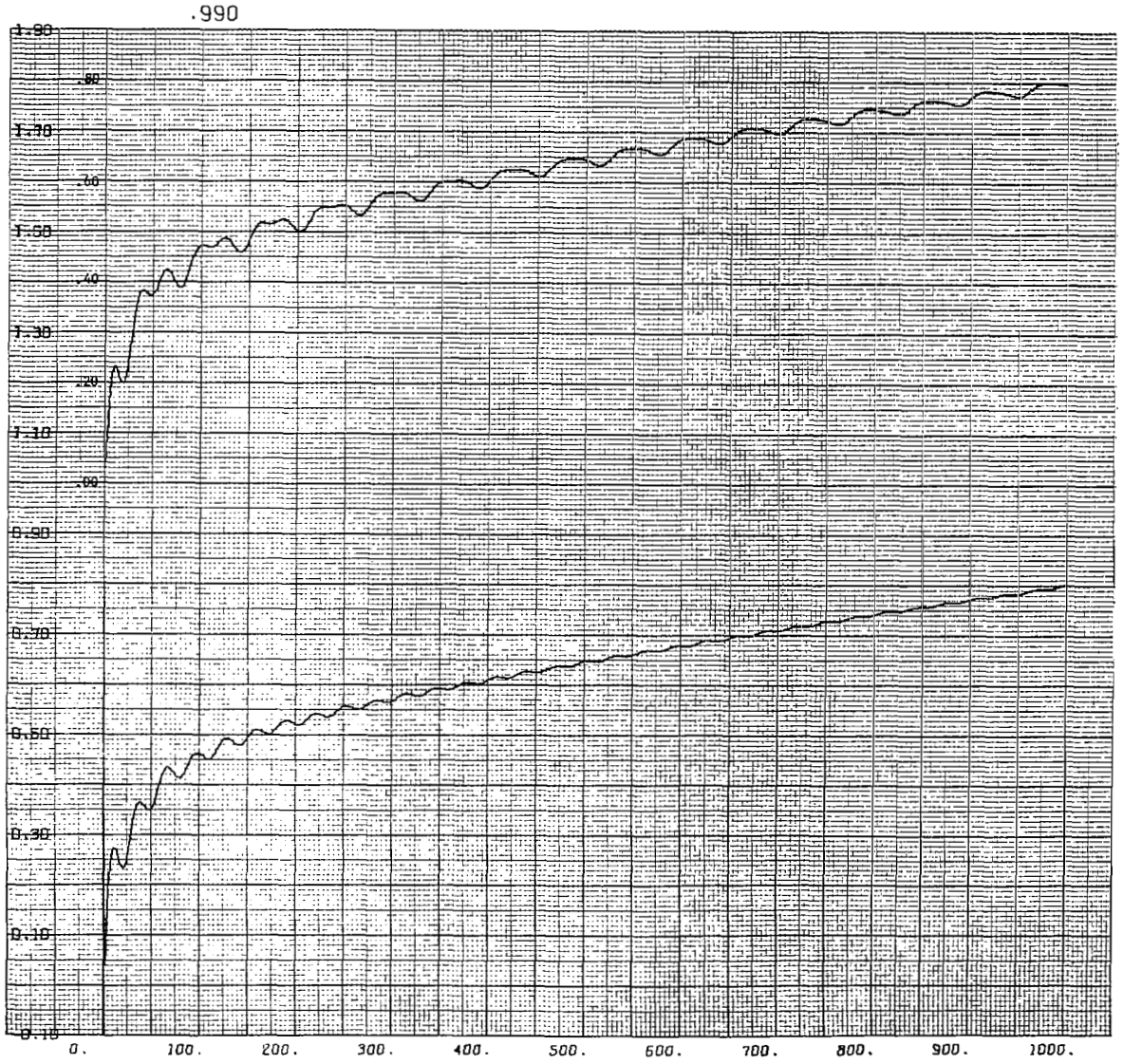

Figure 3d. z/z_o = .99

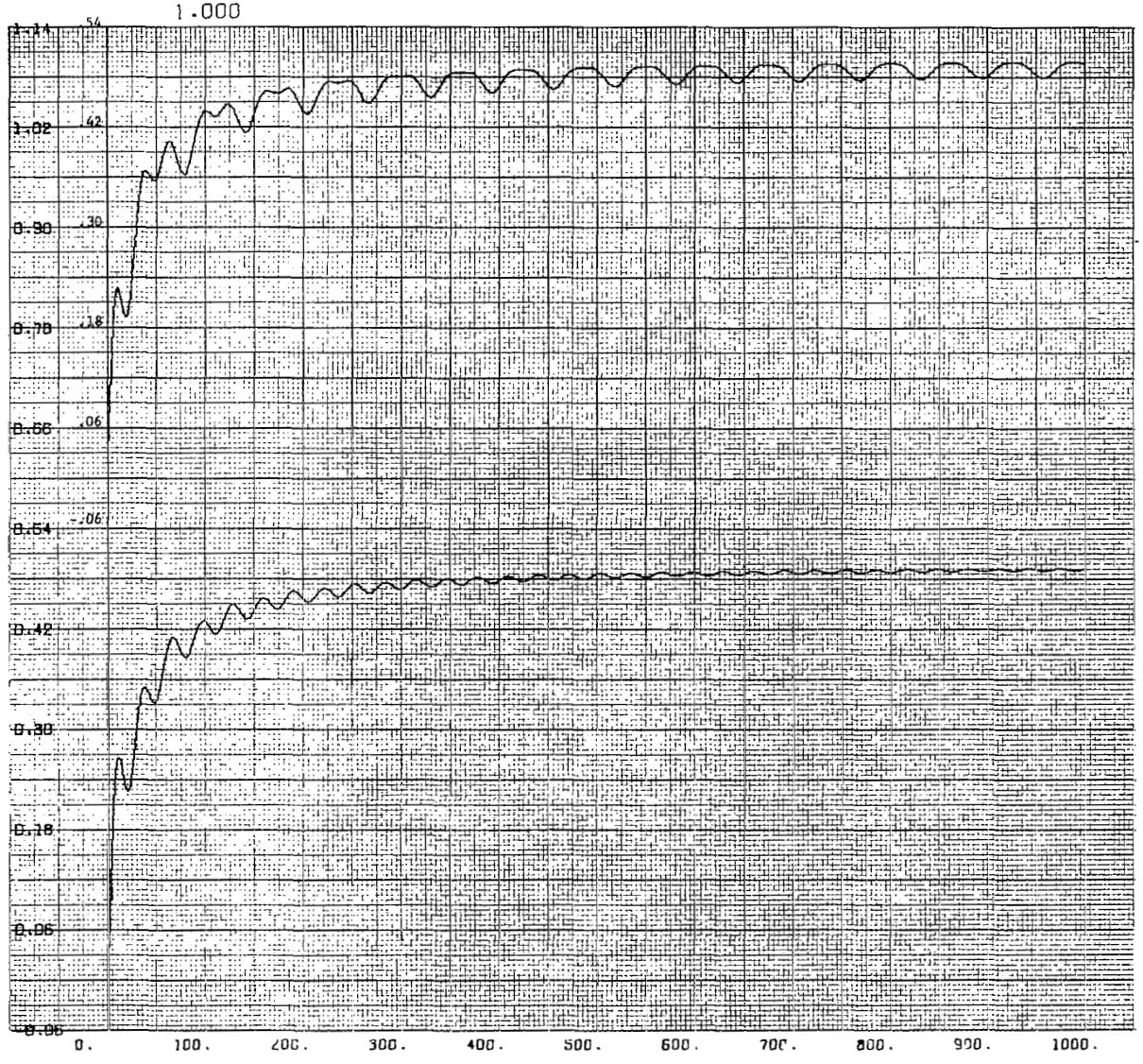

Figure 3e. $z/z_o = 1.00$

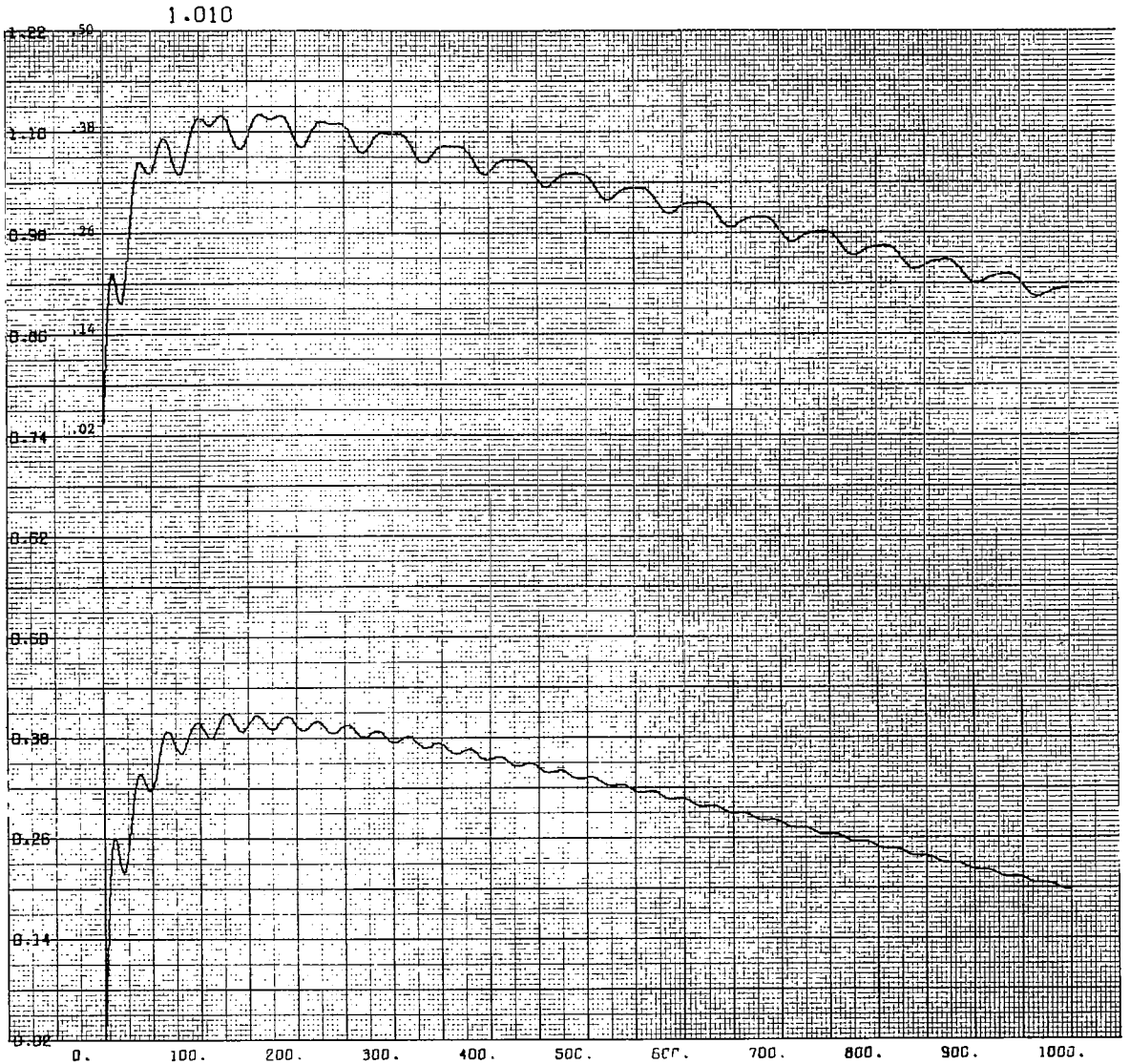

Figure 3f. $z/z_o = 1.01$

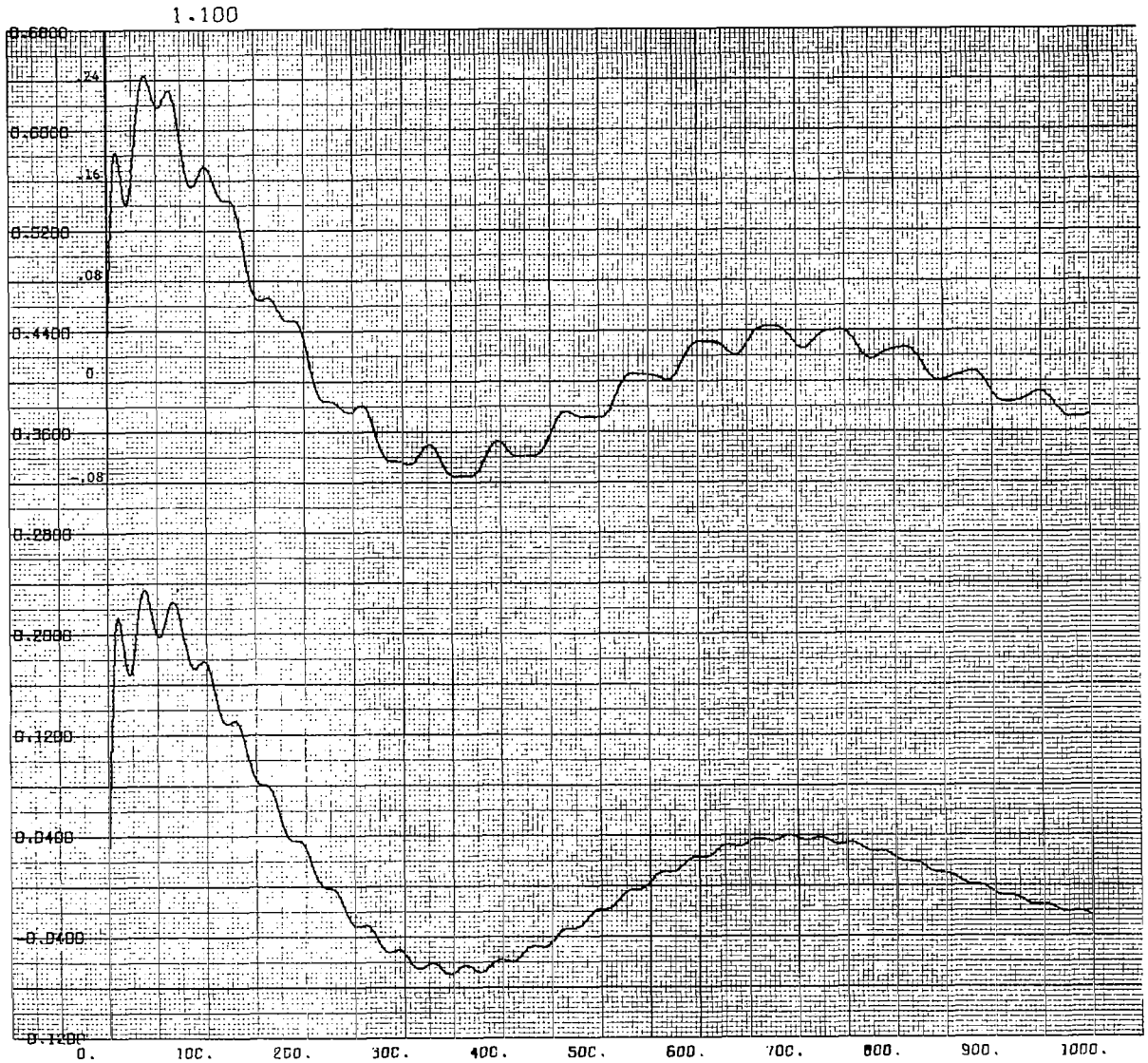

Figure 3g. $z/z_o = 1.10$

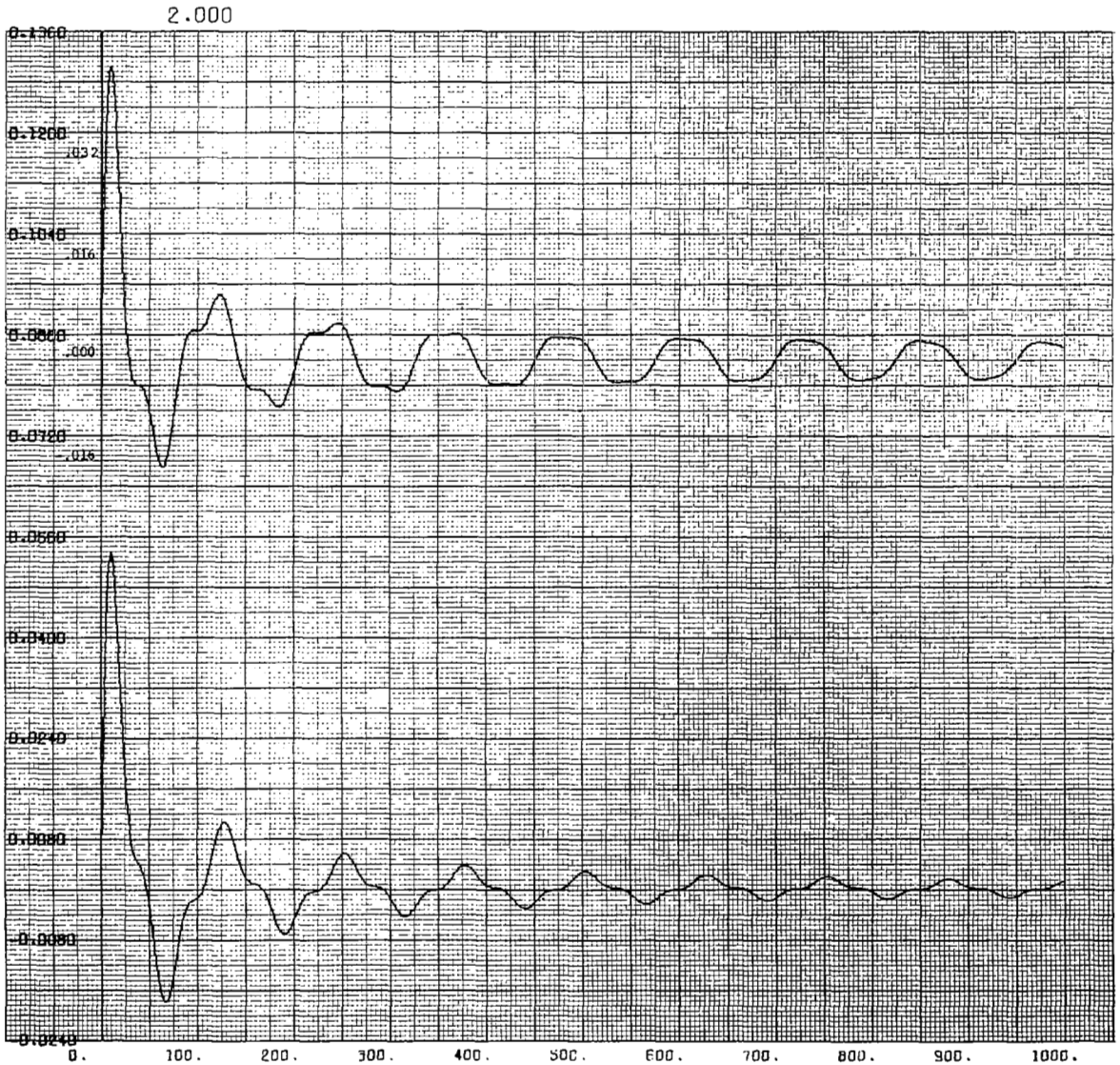

Figure 3h. $z/z_o = 2.00$

C. Numerical Inversion Using Eq. (1.13)

The asymptotic behavior of the function $h(\rho)$ in the limit $\rho \to \infty$ is prescribed by Eq. (1.7). Its behavior for small ρ is arbitrary. If we take $h(\rho) = 0$ for $\rho < \rho_m$, Eq. (1.13) becomes

$$S(z) = \frac{8\Gamma\left(\frac{11}{6}\right) z^{-11/6} k^{-1/6}}{\pi \sqrt{3}\ \Gamma(8/3)} \left(\int_0^{\rho_m} B_\chi(\rho) + \int_{\rho_m}^{\infty} \left[B_\chi(\rho) - h(\rho) \right] \right. \tag{3.6}$$

$$\left. + \int_{\rho_m}^{\infty} h(\rho) \right) \rho\ \mathrm{Im}\left\{ e^{i\pi/12}\ F\left(\frac{11}{6} \,\middle|\, 1 \,\middle|\, \frac{i\rho^2 k}{4z} \right) \right\} d\rho$$

The second integral in Eq. (3.6) is small compared to the third because in the former, $h(\rho)$ just cancels the leading term in the asymptotic series of $B_\chi(\rho)$, and hence, being of higher order in the small quantity $4z_o/\rho_m{}^2 k$, it is negligible. For $\rho > \rho_m$, $h(\rho)$ is taken equal to the leading term in the asymptotic series of $B_\chi(\rho)$,

$$h(\rho) = \begin{cases} 0, & \rho < \rho_m, \\ -\frac{\sqrt{3}}{32\pi}\ \Gamma\left(\frac{8}{3}\right)\ \Gamma^2\left(\frac{7}{6}\right) \int_0^{\infty} z^2 C_n^2(z)\, dz\ \left(\frac{\rho}{2}\right)^{-7/3}, & \rho > \rho_m. \end{cases} \tag{3.7}$$

In the remaining integral from ρ_m to ∞ in Eq. (3.6), the confluent hypergeometric function may be approximated by the first term in its asymptotic series.

$$\mathrm{Im}\left\{ e^{i\pi/12}\ F\left(\frac{11}{6} \,\middle|\, 1 \,\middle|\, \frac{i\rho^2 k}{4z} \right) \right\} \sim \frac{1}{\Gamma(11/6)} \left(\frac{\rho^2 k}{4z} \right)^{5/6} \cos\left(\frac{\rho^2 k}{4z} \right) \tag{3.8}$$

The integral from ρ_m to ∞ is therefore approximated by

$$\int_{\rho_m}^{\infty} d\rho\ \rho\ \rho^{-7/3} \left(\rho^2 k/4z \right)^{5/6} \cos\left(\rho^2 k/4z \right) = \frac{1}{2} \left(\frac{k}{4z} \right)^{1/6} \int_{\rho_m{}^2 k/4z}^{\infty} d\left(\frac{\rho^2 k}{4z} \right) \tag{3.9}$$

$$\left(\frac{\rho^2 k}{4z} \right)^{-1/3} \cos\left(\frac{\rho^2 k}{4z} \right) \sim -\frac{1}{2} \left(\frac{k}{4z} \right)^{1/6} \left(\frac{\rho_m{}^2 k}{4z} \right)^{-1/3} \sin\left(\frac{\rho_m{}^2 k}{4z} \right).$$

Substituting Eqs. (3.7), (3.8) and (3.9) in Eq. (3.6), we obtain

$$S(z) \cong \frac{8\,\Gamma\left(\frac{11}{6}\right) z^{-11/6} k^{-1/6}}{\pi\sqrt{3}\,\Gamma(8/3)} \int_0^{\rho_m} d\rho\ \rho B_\chi(\rho)\,\mathrm{Im}\left\{ e^{i\pi/12}\, F\left(\frac{11}{6}\,\middle|\,1\,\middle|\,\frac{i\rho^2 k}{4z}\right)\right\}$$

$$+ \frac{\Gamma^2(7/6)}{2\pi^2} \frac{\int_0^{\infty} z'^2\, C_n^2(z')\,dz'}{z^2} \left(\frac{\rho_m^2 k}{4z}\right)^{-1/3} \sin\left(\frac{\rho_m^2 k}{4z}\right). \tag{3.10}$$

The significance of Eq. (3.10) is that if data is available for $B_\chi(\rho)$ only over a finite range of ρ $(0 < \rho < \rho_m)$, the second term in Eq. (3.10) provides a first-order approximation to the missing part $(\rho_m < \rho < \infty)$ of the integral in Eq. (1.10). The correction term in Eq. (3.10) is related to $B_\chi(\rho)$ approximately by the expression[4]

$$\frac{8\,\Gamma\left(\frac{7}{6}\right)}{3\sqrt{3}\,\pi^2\,\Gamma\left(\frac{8}{3}\right)} \left(\frac{\rho_m^2 k}{4z}\right)^{-1/3} \sin\left(\frac{\rho_m^2 k}{4z}\right) z^{-2} \int_0^{\infty} dz'\, z'^{-5/6} \int_0^{\rho_m} d\rho\ \rho B_\chi(\rho)$$

$$\mathrm{Im}\left\{ e^{i\pi/12}\, F\left(\frac{5}{6}\,\middle|\,1\,\middle|\,\frac{i\rho^2 k}{4z}\right)\right\}, \tag{3.11}$$

where we have replaced the upper limit in the ρ integral in Eq. (1.8) by ρ_m.

The lower curves in Figures 3a-3h show selected results of the computer calculations of S(z) using Eq. (3.10) with $\int_0^{\infty} z^2 C_n^2(z)\,dz = z_o^2$ to invert the correlation function (3.1) of a delta-function turbulence profile. It can be seen from a comparison of the lower curves with the upper curves that the effect of the correction term in Eq. (3.10) is to eliminate the dominant oscillatory component [proportional to $(yz_o/z)^{-1/3} \sin(yz_o/z)$ according to (3.10)] in the upper curves, for large ρ.

We can see a trend from Figure 3 as z/z_o varies from 0.1 to 2. In Figure 3a, $z/z_0 = 0.1$, there is a high-frequency oscillation, which originates from the kernel function shown in Figure 2, and a lower-frequency modulation,

which originates from the correlation function shown in Figure 1. In Figure 3b, $z/z_o = 0.4$, the high-frequency oscillation has decreased by a factor of 4 in frequency and the lower-frequency modulation is virtually unchanged. These curves appear to be converging to unity (within the precision of the calculation). In Figure 3c, $z/z_o = 0.9$, the higher-frequency due to the kernel has decreased to 10/9 of the lower-frequency of the correlation function, and the low-frequency beats are evident. This is analogous to the Gibbs phenomenon of Fourier analysis. In Figure 3d, $z/z_o = 0.99$, the beat-frequency has become very small and we see that the entire curve from $\rho^2 = 0$ to $\rho^2 = 400\ z_o/k$ represents a small fraction of a cycle, and the integration range is too small for the integral to reach unity. In Figure 3e, $z/z_o = 1.0$, the beat frequency is zero and the curve appears to be heading for 1/2. In Figure 3f, $z/z_o = 1.01$, the trend reverses. The beat frequency is very small but the curve is now starting downward toward zero. In Figure 3g, $z/z_o = 1.1$, the appearance is similar to Figure 3c, $z/z_o = 0.9$, except the beat-frequency oscillation is centered on zero rather than one. In Figure 3h, $z/z_o = 2.0$, the beat frequency has increased and the amplitude of oscillation around zero decreased.

D. Dependence of Spatial Resolution on ρ_m

We can now use these results to answer the important practical question of how the spatial resolution obtainable in the turbulence profile depends on the value of ρ_m in Eq. (3.10). Figure 4 is a plot of S(z) versus z/z_o for four different values of ρ_m ($\rho_m^2 k/4z_o = 12.5$, 25, 50, and 100). The points in Figure 4 are obtained from the results shown in Figures 3a-3h, as well as the results of calculations for other values of z/z_o not illustrated in this report. The curves in Figure 5 are the negative derivatives of the curves in Figure 4. They show the calculated turbulence profiles, $C_n^2(z)$, for the four values of ρ_m.

The width of these four profiles is a measure of the loss in resolution (i.e., departure from a delta function at $z = z_o$), which increases as ρ_m decreases. The width of the profile can be defined in a number of ways, e.g., the distance between the two points on the profile, $C_n^2(z)$, where $C_n^2(z) = \frac{1}{2} C_n^2(z_o)$. We choose rather to define the width as the distance between the points, z_1, z_2 closest to z_o where $S(z_1) = 1$ and $S(z_2)$, 0, respectively. Referring to Figures 4 and 5, it can be seen that this gives a width

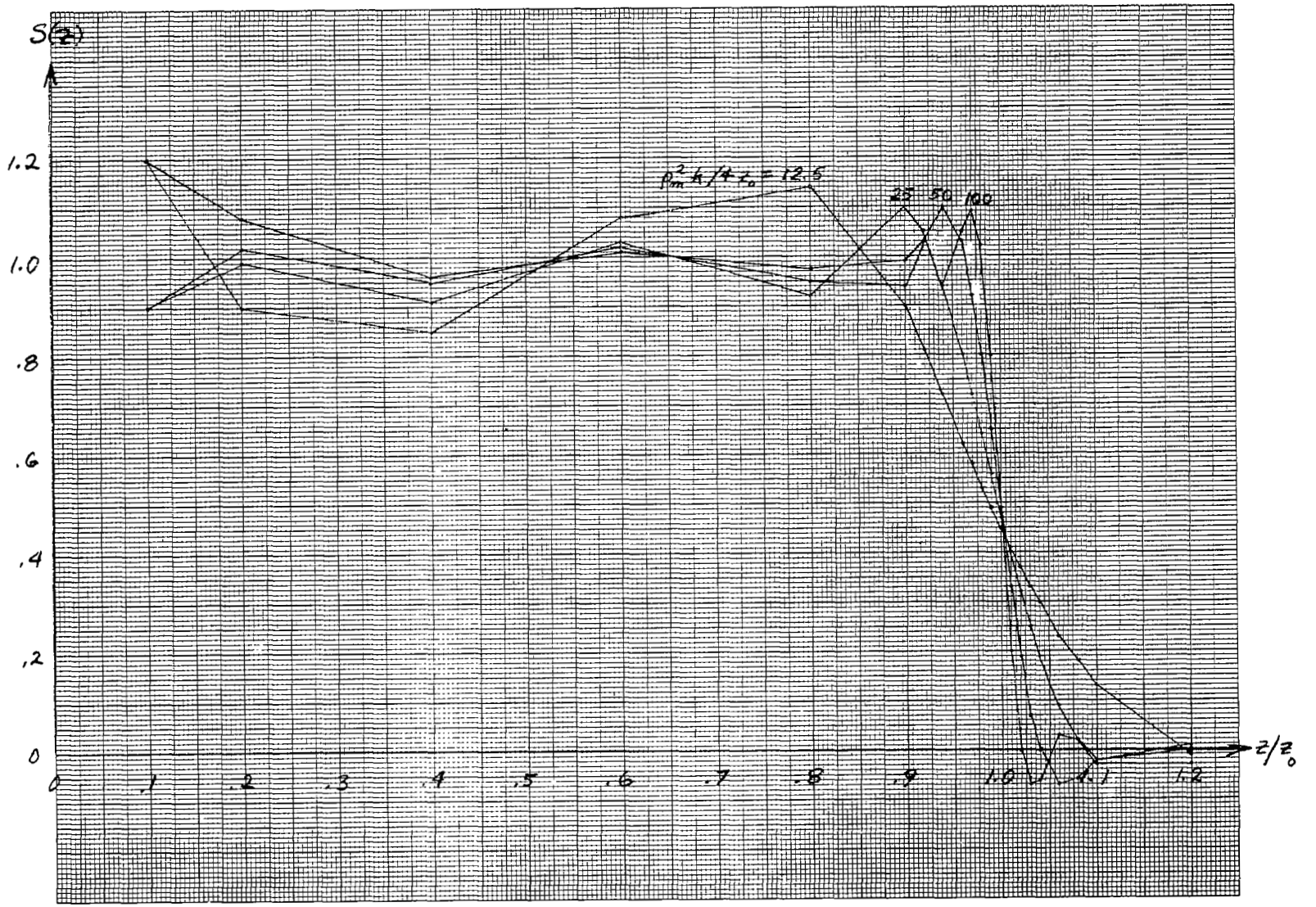

Figure 4. Calculated integrated turbulence profile S(z) for delta-function profile, versus z/z_o for $\rho_m^2 k/4z_o$ = 12.5, 25, 50 and 100.

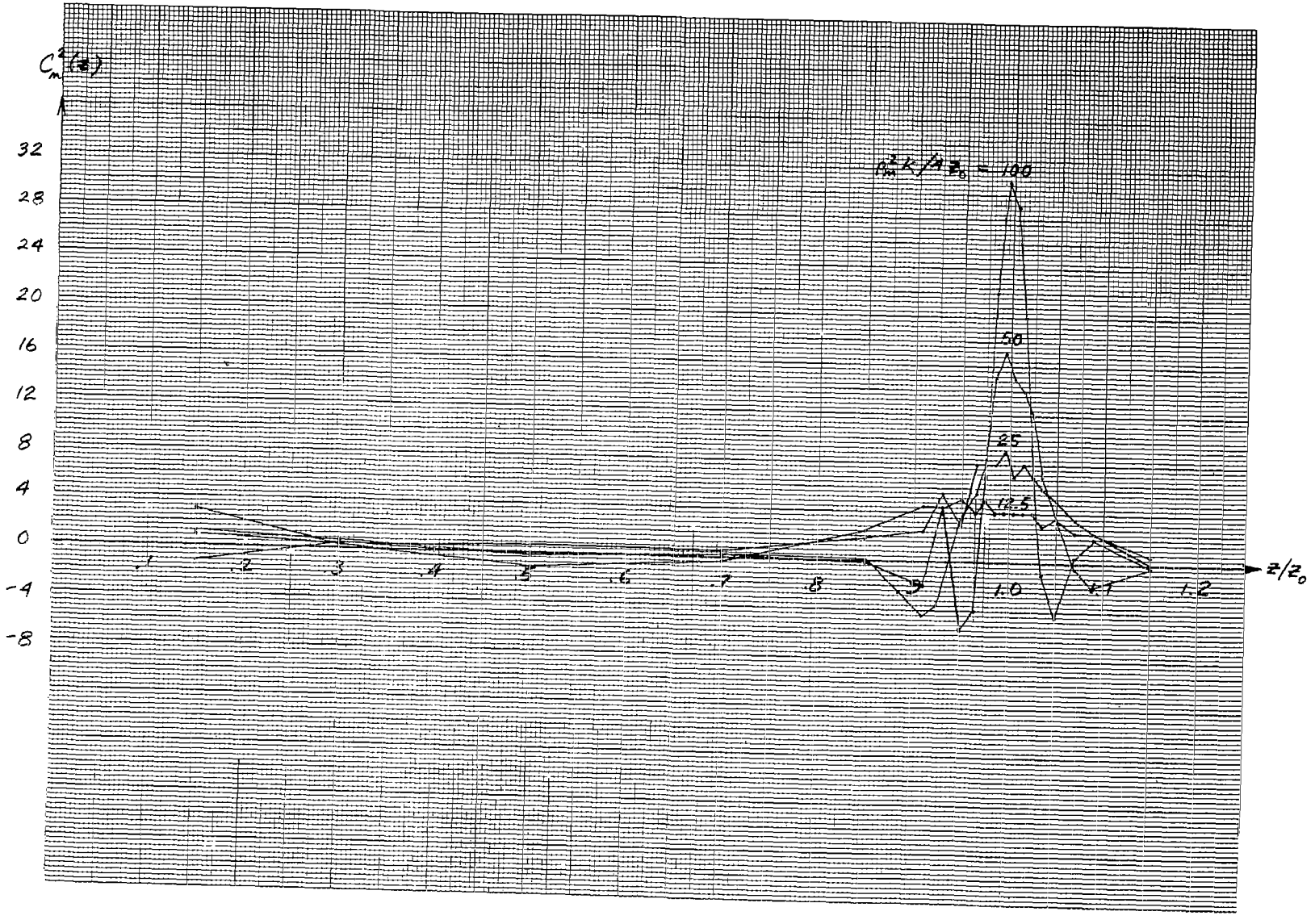

Figure 5. Calculated profile $C_n^2(z)$ for delta-function profile versus z/z_o for $\rho_m^2 k/4z_o$ = 12.5, 25, 50 and 100.

about one-third larger than the width defined between the two $\frac{1}{2} C_n^2(z_o)$ points. Note that the integrated turbulence under the portion of the profile $z_1 < z < z_2$ equals the total integrated turbulence; the integrated turbulence outside $z_1 < z < z_2$ is as much positive as negative, with a net area of zero.

In Figure 6 we have fitted a straight line (A) to the points taken from Figure 3c and other results not shown for z/z_o from .92 to .98, of the one-crossing closest to z_o, and from Figure 3g and other results not shown for z/z_o from 1.02 to 1.08, of the zero-crossing closest to z_o (B). Figure 6 is a plot of $\left| 1 - z_\alpha / z_o \right|$ versus $\rho_m^2 k/4z_o$, where $\alpha = 1, 2$, correspond to the distance from z_o to the one-crossing, divided by z_o, and to the zero-crossing, divided by z_o, respectively. We have also plotted the normalized width, D/z_o, defined by $D = z_2 - z_1$. The line labeled C in Figure 6 was obtained by fitting a straight line to the points found by adding the ordinates of the two lines A and B. The slope of the line C is minus one, and we obtain the relation

$$\frac{D}{z_o} = 4\left(\frac{\rho_m^2 k}{4z_o}\right)^{-1} = \frac{16 z_o}{\rho_m^2 k} \tag{3.12}$$

The coefficient 4 in Eq. (3.12) is somewhat arbitrary, and depends on the particular way in which we defined the width. The inverse dependence of D on the variable $\rho_m^2 k/4z_o$ is reminiscent of the identical relationship occurring in Fourier transforms. D may also be interpreted more generally as the spatial resolution obtainable in an arbitrary turbulence profile. Thus, at range z, variations in the profile that occur in distances less than $D = 16\, z^2/\rho_m^2 k$ cannot be resolved.

E. Dependence of Spatial Resolution on Step-Size

In our numerical studies, the integral transforms appearing in Eqs. (1.10) and (3.10) are approximated by sums. In most actual measurements of $B_\chi(\rho)$, the correlation function will be measured at a discrete set of points, ρ_i, in the range $0 < \rho_i < \rho_m$. Thus, the natural way to handle the inversion of an experimentally obtained correlation function is by performing a sum rather than an integral. In addition to the sensitivity of the profile calculation to ρ_m, which was considered in the last section, there is also a dependence on the number

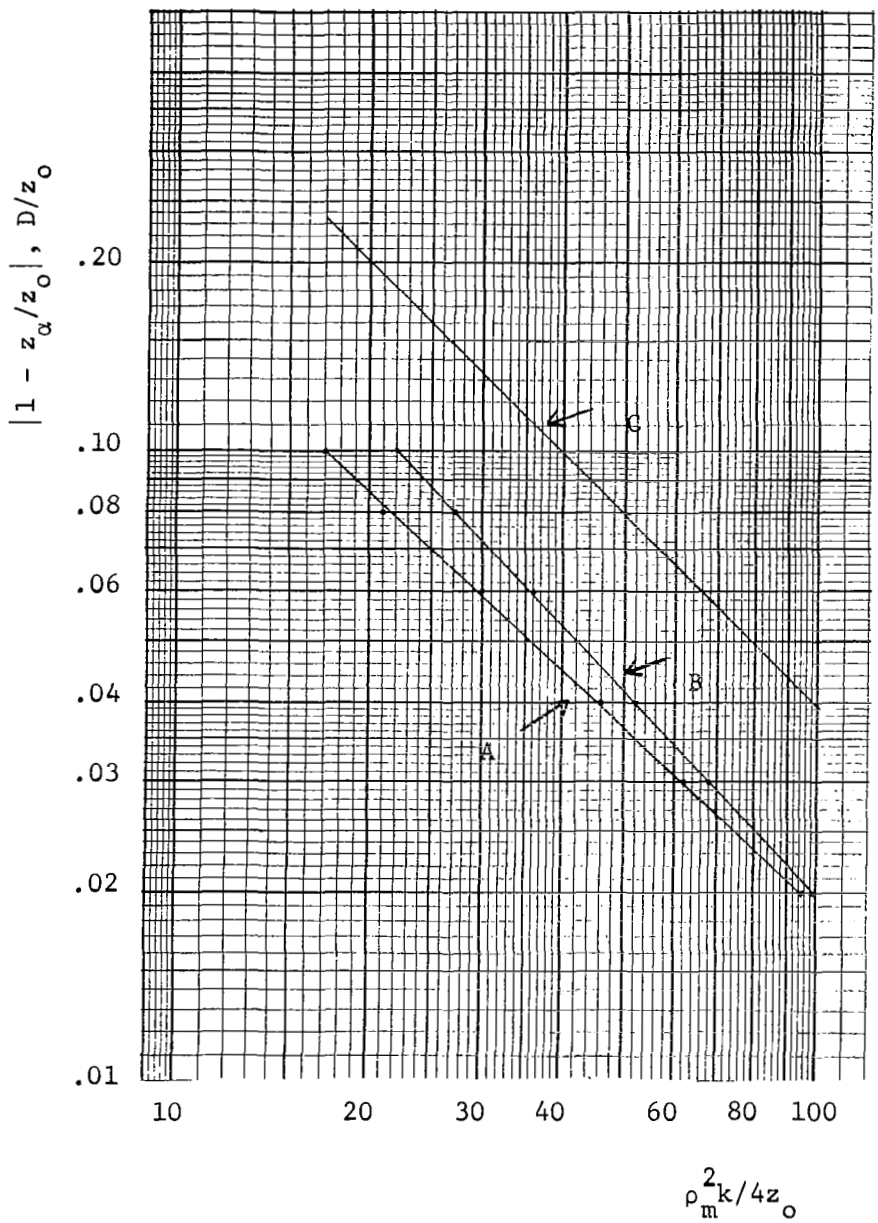

Figure 6. Width of calculated profile versus $\rho_m^2 k/4z_o$.

A. Normalized distance from z_o to closest one crossing of S(z),

B. Normalized distance from z_o to closest zero crossing of S(z),

c. Normalized width, D/z_o (sum of A and B).

of elements in the sum (2,001 in the above calculations). By observing the effect of varying the number of summands, we can obtain a measure of the number of sample points, ρ_i, necessary to obtain a given precision in the calculated integrated profile, S(z).

We have repeated the above calculations with a smaller number of summands. Representative results are shown in Figures 7, 8 and 9 for z/z_o = 0.4, 0.8, and 1.2, respectively. The results in the figures are shown for (a) 1,001; (b) 501; (c) 201, and (d) 101 points. In Figure 10 we show the integrated profiles S(z) obtained for $\rho_m^2 k/4z_o = 100$ and the five different choices of total number of terms in the summation.

For the more distant portion of the profile, $z > z_o$, the five cases are in good agreement. But for smaller ranges, the calculated profiles depart more from the actual profile as the number of summands decreases. The departure occurs because we are not sampling enough points to adequately represent the fine structure in Figures 3a-3h or, equivalently, in the kernel function $\text{Im}\left\{\exp(i\pi/12)\, F(11/6 \mid 1 \mid i\rho^2 k/4z)\right\}$ of Eqs. (1.10) and (3.10), shown in Figure 2. The scale size of the kernel becomes smaller as z/z_o decreases.

By studying the detailed behavior of the calculations shown in Figures 7-9 (as well as the other cases performed but not shown in this report) we observe that the deviation between the calculated and actual profile arises mostly from the portion of the integrals taken over small ρ ($\rho << \rho_m$). Therefore, we expect that better results would be obtained for a fixed number of summands, if the sample points were spaced relatively more densely at small values of ρ. In the present calculations, we have used uniform spacing in ρ^2. Uniform spacing in ρ should be more advantageous, and we will rewrite the computer programs to verify this assertion.

In a practical application it is important to know the number of points at which the correlation function must be sampled. For example, if an array of photomultiplier tubes is utilized to obtain $B_\chi(\rho)$, the required number of tubes depends on the number of sample points needed.

According to Eq. (3.12), when $\rho_m^2 k/4z_o = 100$, the spatial resolution, D, at $z = z_o$ is $0.04z_o$. The results illustrated by Figure 10 (for which $\rho_m^2 k/4z_o = 100$) indicate that if this resolution is required at $z = z_o$, then with

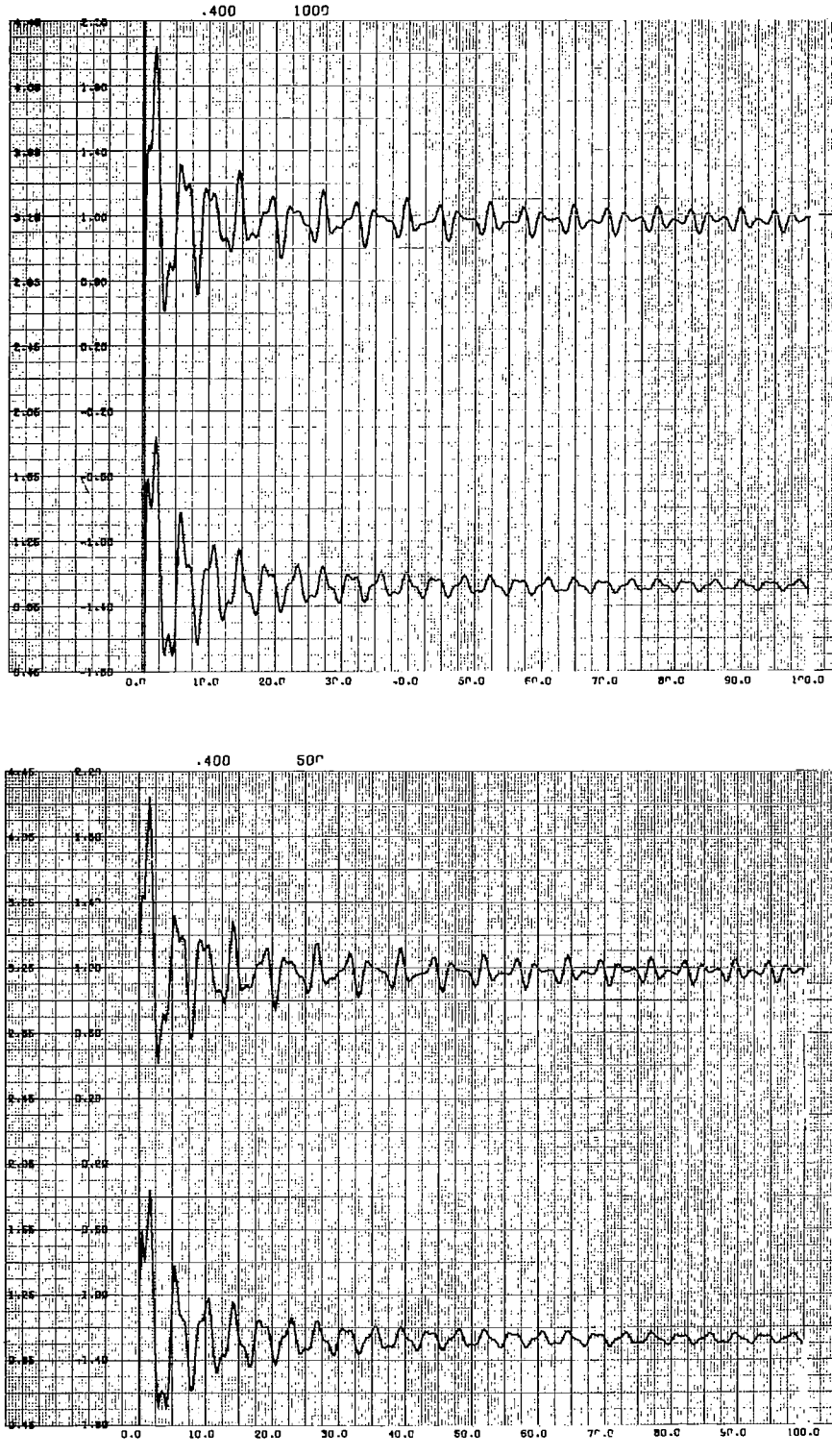

Figure 7. Calculated integrated turbulence profile S(z) versus $\rho_m^2 k/4z_o$ for z/z_o = 0.4, for a (a) 1001, (b) 501, term summation approximation to Eq. (1.6) (upper curve) and Eq. (3.10) (lower curve).

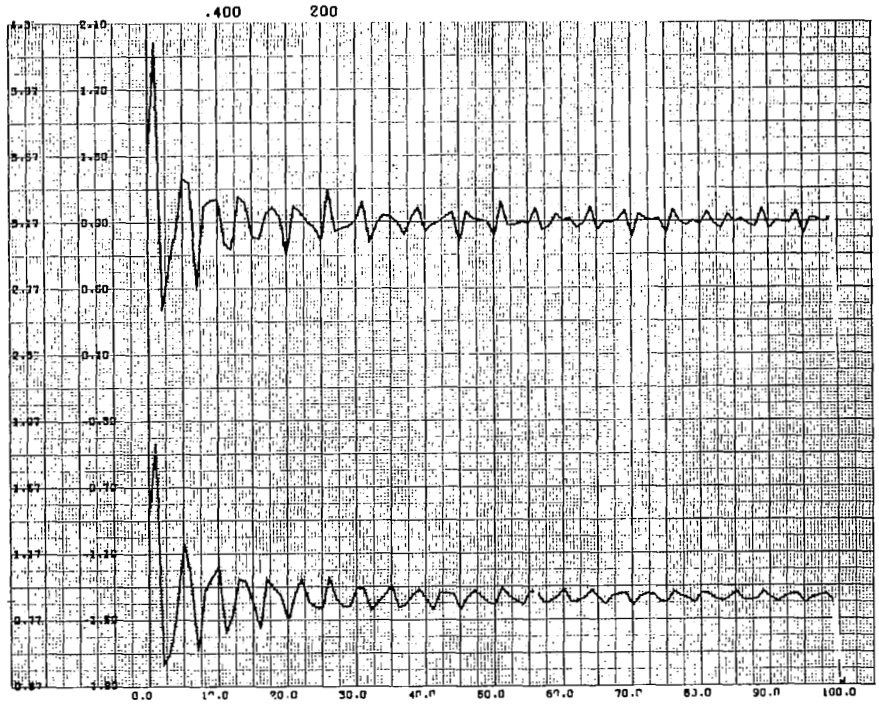

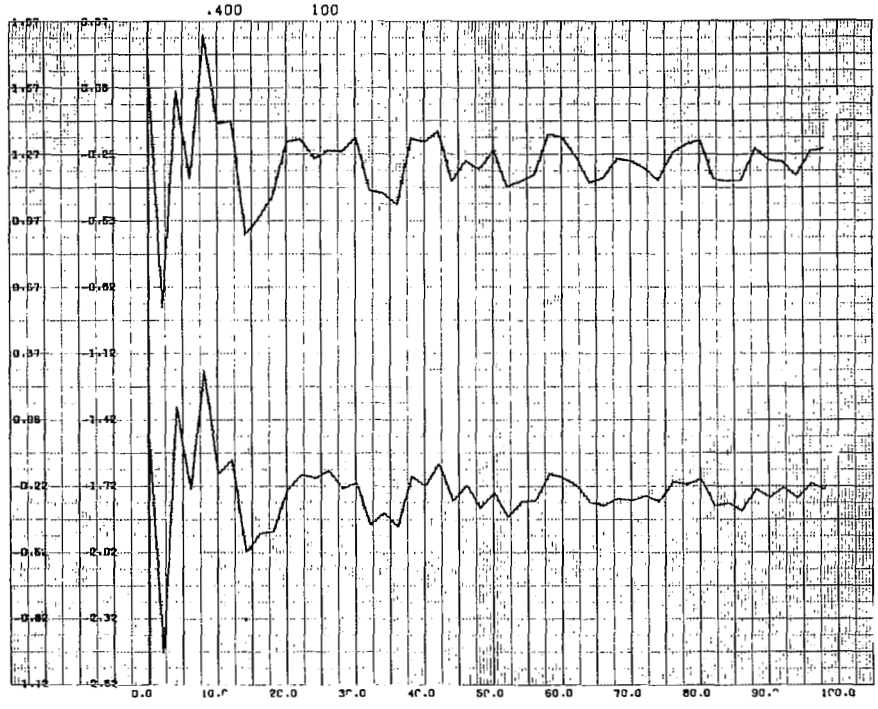

Figure 7 (c) z/z_o = 0.4, 201 term summation

(d) z/z_o = 0.4, 101 term summation

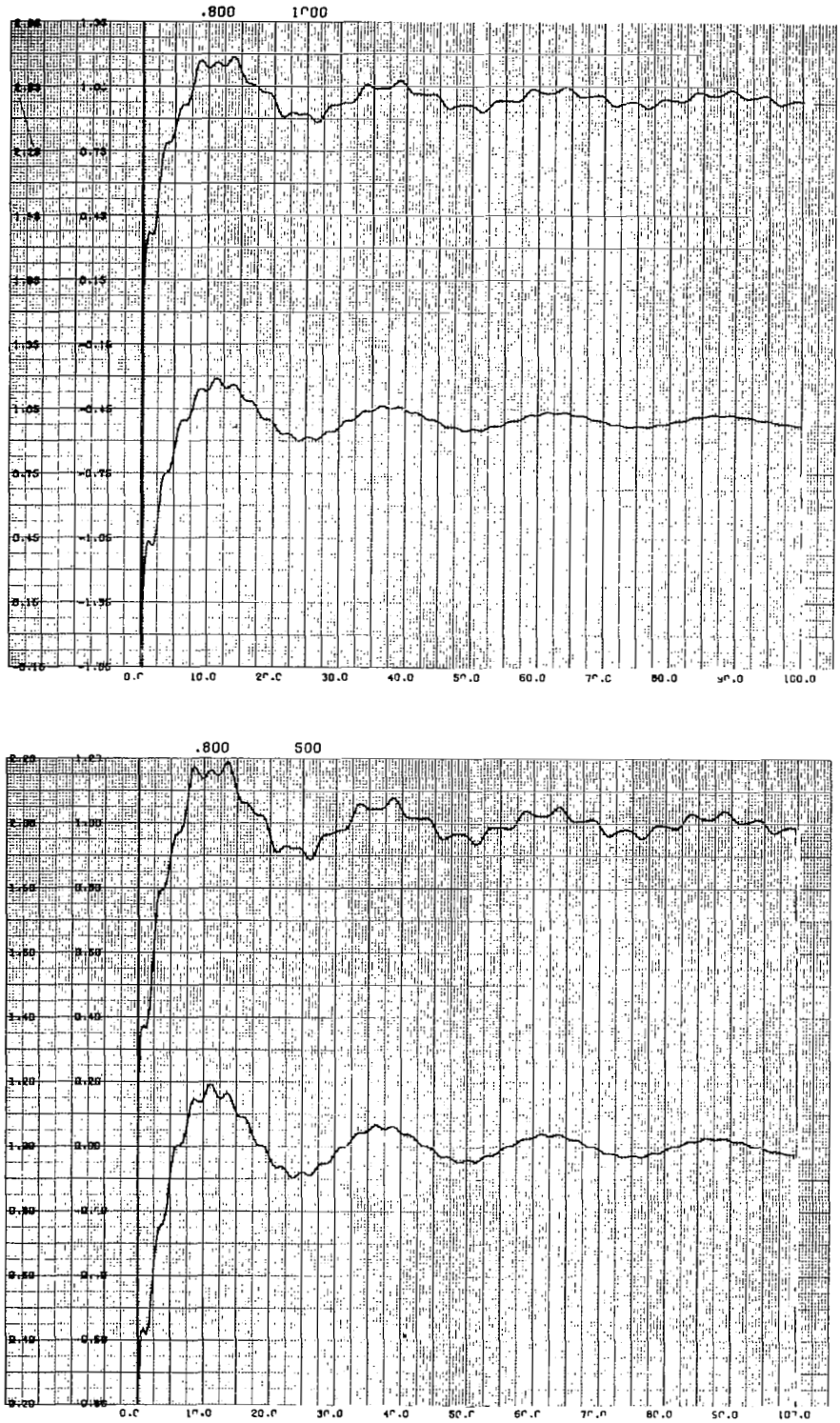

Figure 8. Calculated integrated turbulence profile S(z) versus $\rho_m^2 k/4z_o$ for $z/z_o = 0.8$, for a (a) 1001, (b) 501, term summation approximation to Eq. (1.6) (upper curve) and Eq. (3.10) (lower curve).

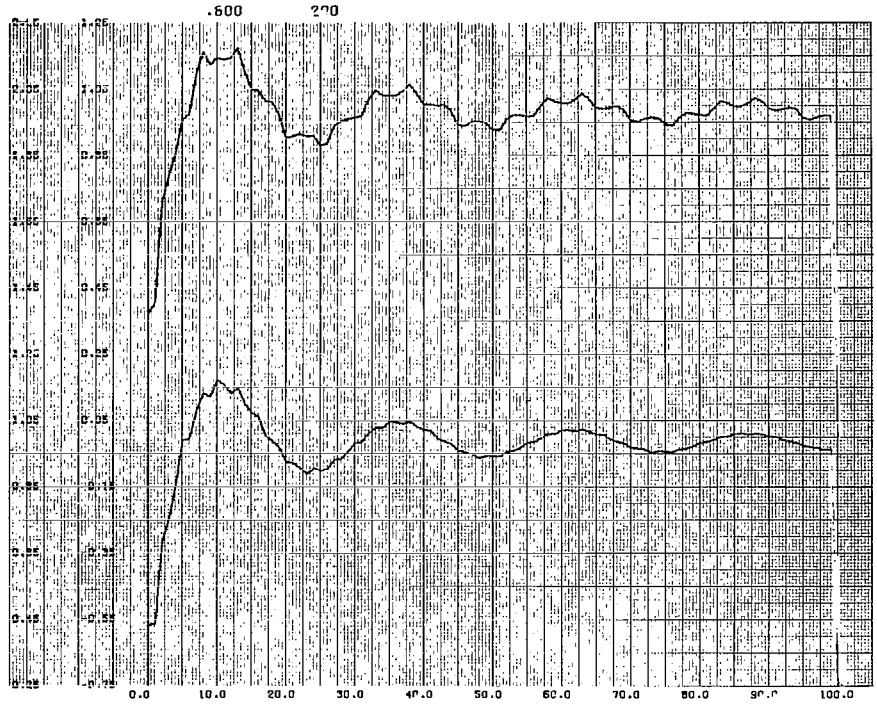

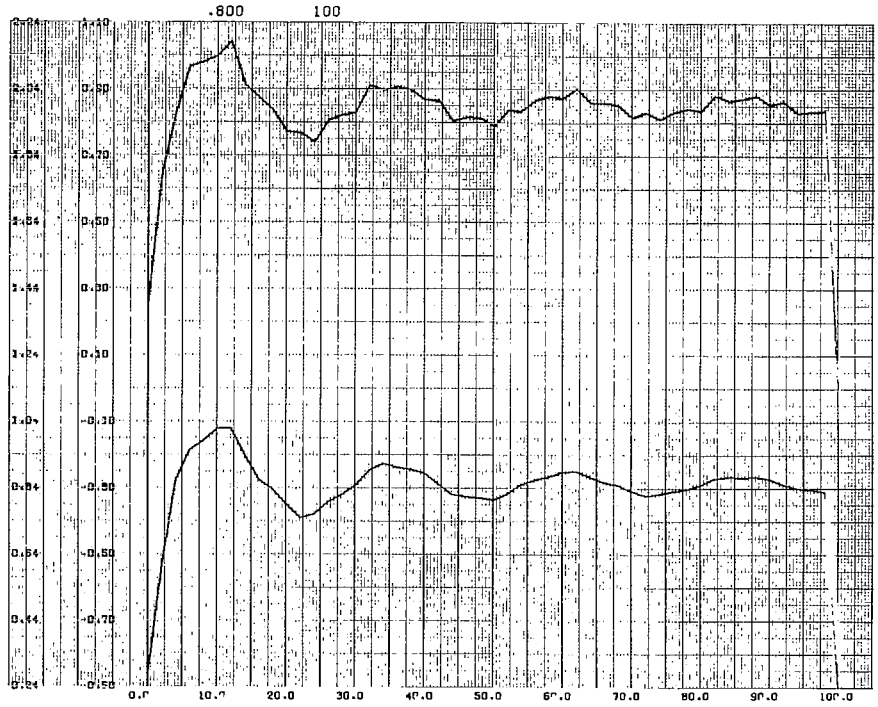

Figure 8 (c) z/z_o = 0.8, 201 term summation

(d) z/z_o = 0.8, 101 term summation

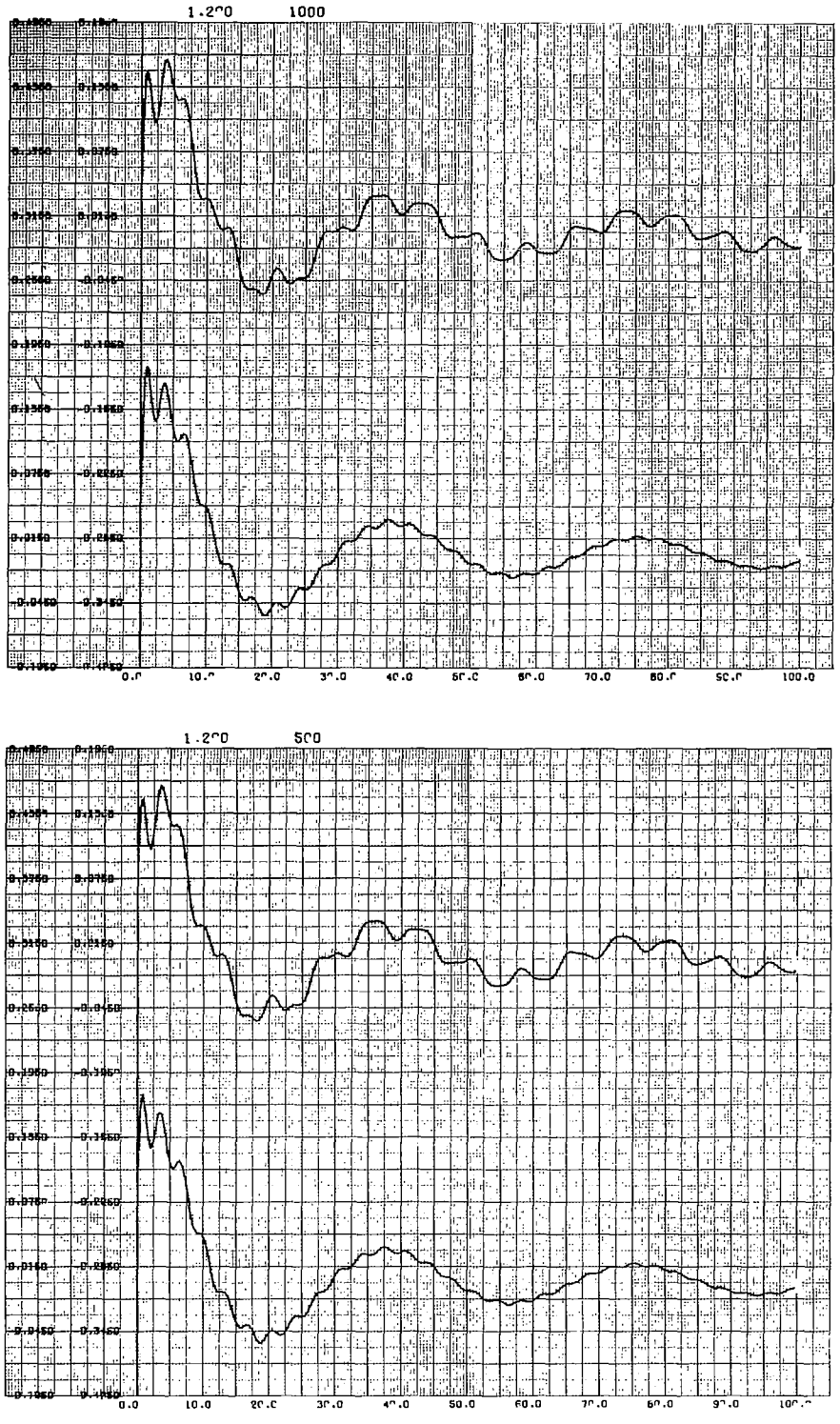

Figure 9. Calculated integrated turbulence profile S(z) versus $\rho_m^2 k/4z_o$ for $z/z_o = 1.2$, for a (a) 1001, (b) 501, term summation approximation to Eq. (1.6) (upper curve) and Eq. (3.10) (lower curve).

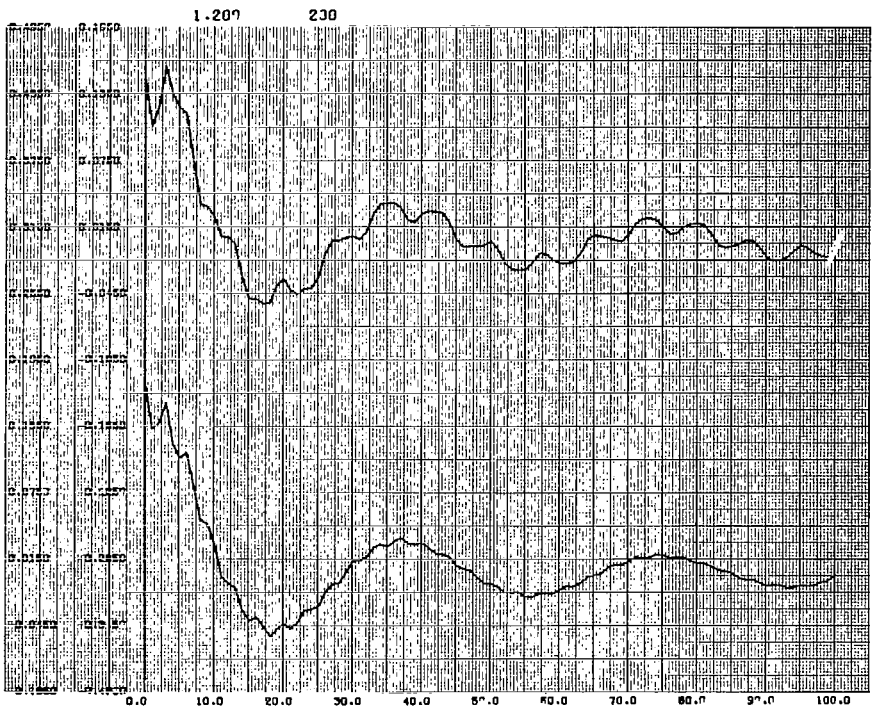

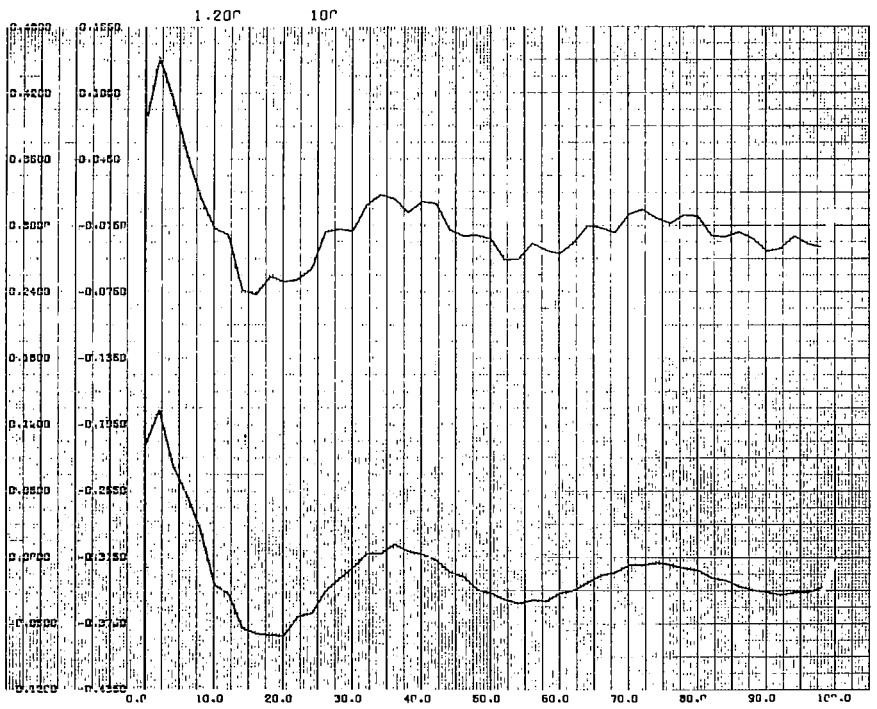

Figure 9 (c) z/z_o = 1.2, 201 term summation

(d) z/z_o = 1.2, 101 term summation

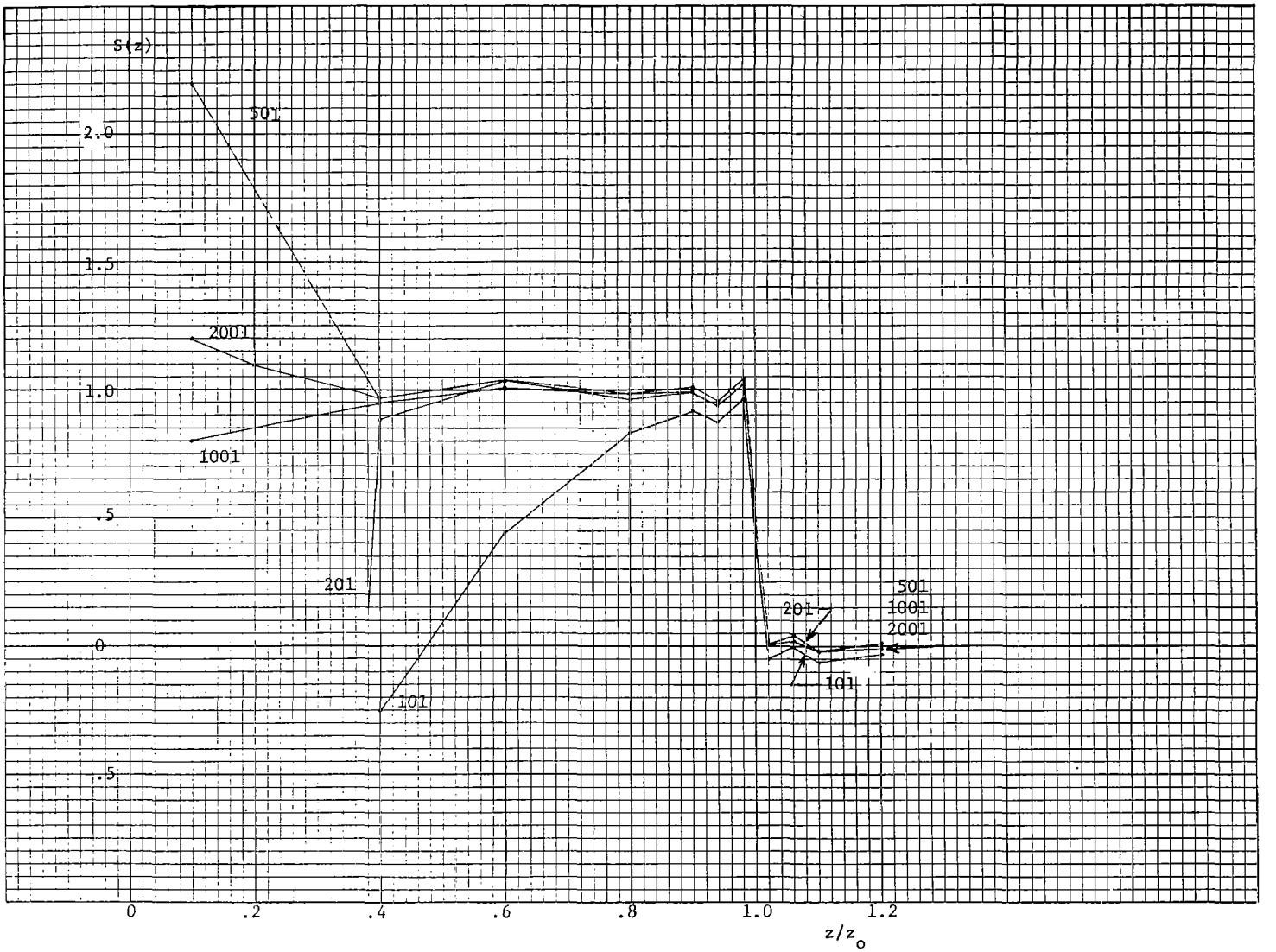

Figure 10. Calculated integrated profile S(z) for delta-function profile versus z/z_o for $\rho_m^2 k/4z_o = 100$ and number of summands equal to 2001, 1001, 501, 201 and 101.

200 terms in the summation the profile can also be calculated from $B_\chi(\rho)$ at $z = 0.4z_o$ and that 1000 terms are necessary to calculate it at $z = 0.1z_o$.

If we relax the resolution requirement at $z = z_o$, and thereby reduce ρ_m^2, we can, of course, obtain the profile at small values of z with correspondingly fewer terms. The number of terms required at a small value of z is inversely proportional to $\rho_{m_2}^2$. However, it is expected that with uniform spacing in ρ_m (rather than ρ_m^2) we will require fewer terms, because the number required for calculating S(z) at $z << z_o$ will be inversely proportional to ρ_m.

IV. INVERSION OF CORRELATION FUNCTION FOR A CONTINUOUS TURBULENCE PROFILE

A. Correlation Function for Continuous Turbulence Profile

We have thus far studied the properties of the inversion of the correlation function of a delta-function turbulence profile. It is also of interest to study the inversion process when the turbulence profile is a smoothly-varying function of position. For convenience, we choose a particular family of progressively more-sharply-peaked smooth curves (whose limit is the delta function) for $C_n^2(z)$, for which it is possible to obtain analytic expressions for $B_\chi(\rho)$. In this way we avoid the inconvenience of having to do a numerical integration to obtain $B_\chi(\rho)$.

A suitable turbulence profile is

$$C_n^2(z) = \frac{A}{z_o \Gamma(\mu)} \left(\frac{\mu z}{z_o}\right)^\mu e^{-\mu z / z_o} . \tag{4.1}$$

The normalization of Eq. (4.1) is such that

$$\int_0^\infty C_n^2(z)dz = A \text{ cm}^{1/3}.$$

Taking the z-derivative of Eq. (4.1),

$$\frac{d}{dz} C_n^2(z) = \frac{A(\mu/z_o)^{\mu+1}}{\Gamma(\mu)} \left[z^{\mu-1} - z^\mu z_o^{-1}\right],$$

we see that it vanishes when $z=z_o$, so that the peak of the profile occurs at $z=z_o$, independent of μ. As μ increases, the peak becomes narrower and higher. We can investigate the dependence of the shape of the peak on μ in the following way. Let $C_n^2(z) = \exp(g)$. Then

$$g = \log C_n^2(z) = \log\left(\frac{A \mu^\mu z_o^{\mu-1}}{\Gamma(\mu)}\right) + \mu \log z - \mu \frac{z}{z_o} . \tag{4.2}$$

The first derivative of g with respect to z vanishes at z_o. The second derivative is

$$g'' = -\frac{\mu}{z^2}. \tag{4.3}$$

In the vicinity of $z=z_o$, g may be approximated by the first two nonvanishing terms in its Taylor series,

$$g(z) \cong g(z_o) + \frac{1}{2} g''(z_o)\,(z - z_o)^2, \tag{4.4}$$

and hence $C_n^2(z)$ is approximated by

$$C_n^2(z) = e^{g(z_o) + \frac{1}{2} g''(z_o)\,(z - z_o)^2}$$

$$= C_n^2(z_o)\, e^{-\mu(z - z_o)^2/2z_o^2} \tag{4.5}$$

in the neighborhood of $z=z_o$. Thus we find that in the limit $\mu \gg 1$, the width of the peak varies inversely as the square root of μ. The profiles for $\mu = 1$, 2, and 4 are shown in Fig. 11.

The equation giving the correlation function $B_\chi(\rho)$ in terms of the turbulence profile $C_n^2(z)$ is

$$B_\chi(\rho) = \frac{1}{4}\sqrt{3}\,\Gamma\left(\frac{8}{3}\right) k^2 \int_0^\infty dz\, C_n^2(z) \int_0^\infty d\kappa\, \kappa^{-8/3} J_0(\kappa\rho) \left[1 - \cos\left(\frac{\kappa^2 z}{k}\right)\right] \tag{4.6}$$

Substituting Eq. (4.1) in Eq. (4.6) we obtain

$$B_\chi(\rho) = \frac{A}{4}\sqrt{3}\,\frac{\Gamma\left(\frac{8}{3}\right)}{\Gamma(\mu)}\,\frac{k^2}{z_o} \int_0^\infty dz \left(\frac{\mu z}{z_o}\right)^\mu e^{-\mu z/z_o} \int_0^\infty d\kappa\, \kappa^{-8/3} J_0(\kappa\rho) \left[1 - \cos\left(\frac{\kappa^2 z}{k}\right)\right]$$

$$= \frac{A}{4}\sqrt{3}\,\frac{\Gamma\left(\frac{8}{3}\right)}{\Gamma(\mu)}\,\frac{k^2}{z_o} \int_0^\infty d\kappa\, \kappa^{-8/3} J_0(\kappa\rho) \int_0^\infty dz \left(\frac{\mu z}{z_o}\right)^\mu e^{-\mu z/z_o} \left[1 - \cos\left(\frac{\kappa^2 z}{k}\right)\right]$$

$$= \frac{A}{4}\sqrt{3}\,\frac{\Gamma\left(\frac{8}{3}\right) k^2}{\Gamma(\mu+1)} \int_0^\infty d\kappa\, \kappa^{-8/3} J_0(\kappa\rho) \int_0^\infty d\xi\, \xi^\mu e^{-\xi} \left[1 - \cos\left(\frac{\kappa^2 z_o}{k\mu}\,\xi\right)\right], \tag{4.7}$$

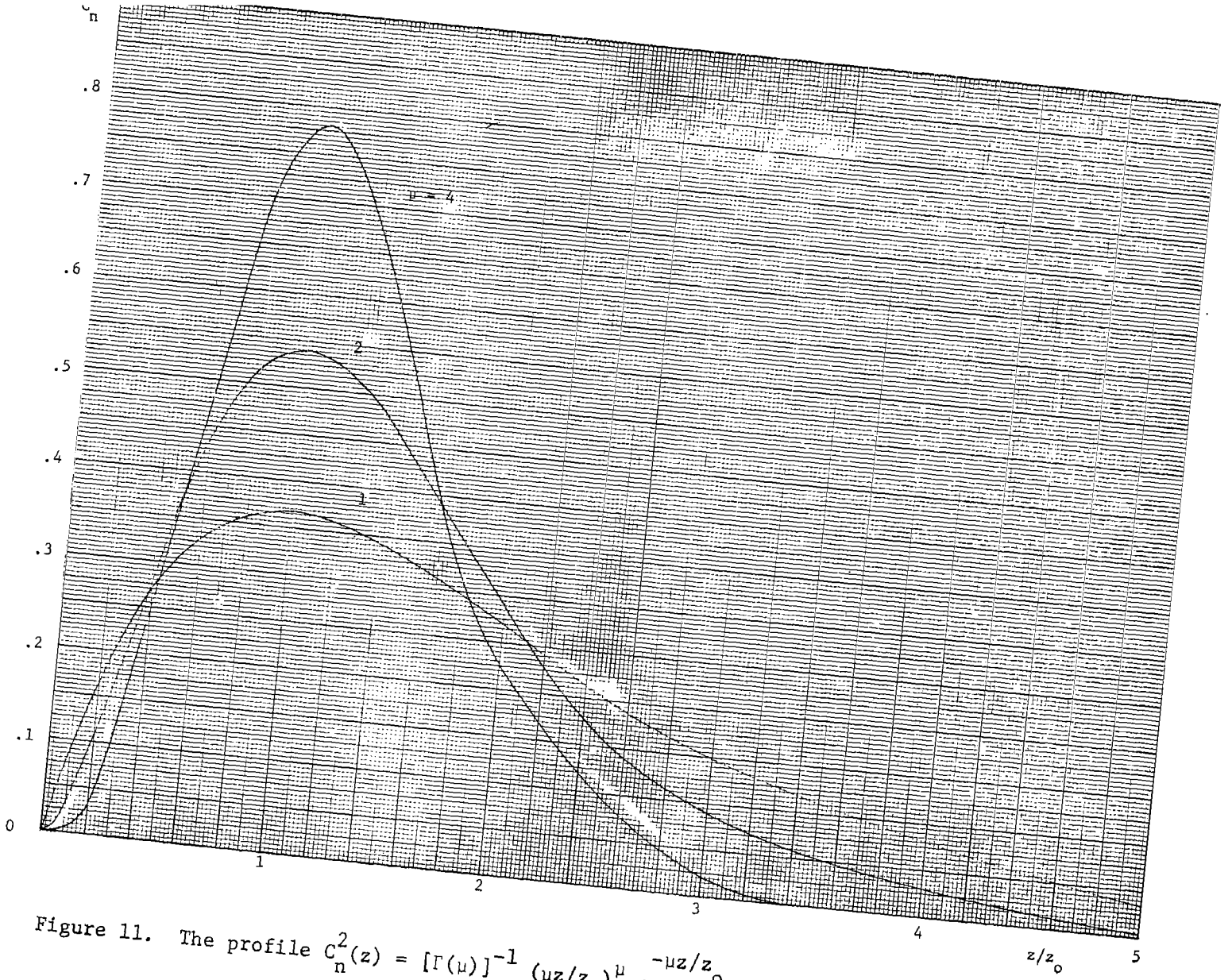

Figure 11. The profile $C_n^2(z) = [\Gamma(\mu)]^{-1} (\mu z/z_o)^{\mu} e^{-\mu z/z_o}$ versus z/z_o for $\mu = 1$, 2 and 4.

where we have interchanged the order of integration and made the change of variable $\xi = \mu z/z_o$.

The ξ-integral can be evaluated.

$$\int_0^\infty d\xi\ \xi^\mu e^{-\xi} = \Gamma(\mu+1), \tag{4.8}$$

and

$$\int_0^\infty d\xi\ \xi^\mu e^{-\xi}\cos(\alpha\xi) = \mathrm{Re}\left\{\int_0^\infty d\xi\ \xi^\mu e^{-(1-i\alpha)\xi}\right\}$$

$$= \mathrm{Re}\left\{(1-i\alpha)^{-(\mu+1)}\,\Gamma(\mu+1)\right\}. \tag{4.9}$$

Substituting Eqs. (4.8) and (4.9) in Eq. (4.7), we find

$$B_\chi(\rho) = \frac{A}{4}\sqrt{3}\,\Gamma\left(\frac{8}{3}\right)k^2 \int_0^\infty d\kappa\,\kappa^{-8/3} J_0(\kappa\rho)\left[1 - \mathrm{Re}\left\{\left(1 - i\frac{\kappa^2 z_o}{k\mu}\right)^{-\mu-1}\right\}\right]. \tag{4.10}$$

The first term in the κ-integral is tabulated.[8]

$$\int_0^\infty d\kappa\,\kappa^{-8/3} J_0(\kappa\rho) = \frac{\rho^{5/3}\,\Gamma\left(-\frac{5}{6}\right)}{2^{8/3}\,\Gamma\left(\frac{11}{6}\right)}. \tag{4.11}$$

The second term is related to a tabulated integral,[9]

$$\int_0^\infty \kappa^{\lambda-1}(1 - i\beta^2\kappa^2)^{-\mu-1} J_0(\kappa\rho)\,d\kappa$$

$$= \frac{\Gamma\left(\frac{\lambda}{2}\right)\Gamma\left(\mu - \frac{\lambda}{2} + 1\right)}{2(-i\beta^2)^{\lambda/2}\,\Gamma(\mu+1)}\ {}_1F_2\left(\frac{\lambda}{2}\,\middle|\,\frac{\lambda}{2} - \mu,\ 1\,\middle|\,\frac{i\rho^2}{4\beta^2}\right)$$

$$+ \frac{(-i\beta^2)^{-(\mu+1)}\left(\frac{\rho}{2}\right)^{2\mu-\lambda+2}\Gamma\left(\frac{\lambda}{2} - \mu - 1\right)}{2\,\Gamma\left(-\frac{\lambda}{2} + \mu + 2\right)}\ {}_1F_2\left(\mu+1\,\middle|\,\mu+2 - \frac{\lambda}{2},\ \mu+2 - \frac{\lambda}{2}\,\middle|\,\frac{i\rho^2}{4\beta^2}\right), \tag{4.12}$$

in which

$$ {}_1F_2\,(a\,|\,b,c\,|\,w) = \sum_{i=0}^{\infty} \frac{(a)_n}{(b)_n (c)_n}\,\frac{\mu^n}{n!}, \tag{4.13} $$

is a hypergeometric function. In (4.13), $(a)_n = \Gamma(a+n)/\Gamma(a)$. Equation (4.12) is valid when Re $\left(\beta^{-1}\, e^{i\pi/4}\right)>0$, and $0 < \text{Re}\ \lambda < 2\ \text{Re}\ \mu + \frac{7}{2}$.[7] The only one of these three requirements not satisfied is Re $\lambda > 0$, since $\lambda = -5/3$ in Eq. (4.10). This causes the integral in Eq. (4.12) to diverge at the lower limit. However, the singularities of the two terms in square brackets in Eq. (4.10) cancel and the integral in Eq. (4.10) does converge. By analytic continuation with respect to the complex variable λ, the difference of Eq. (4.11) and Eq. (4.12), with $\lambda = -5/3$, is a valid representation of Eq. (4.10). Consequently, Eq. (4.10) becomes

$$ B_\chi(\rho) = \frac{A}{4}\sqrt{3}\,\Gamma\left(\frac{8}{3}\right) k^2 \left[\frac{1}{2}\left(\frac{\rho}{2}\right)^{5/3} \frac{\Gamma\left(-\frac{5}{6}\right)}{\Gamma\left(\frac{11}{6}\right)} \right. $$

$$ - \text{Re}\left\{ \frac{\Gamma\left(-\frac{5}{6}\right)\Gamma\left(\mu+\frac{11}{6}\right)}{2\left(-iz_o/k\mu\right)^{-5/6}\,\Gamma(\mu+1)}\ {}_1F_2\left(\frac{5}{6}\,\middle|\,\frac{5}{6}-\mu,\,1\,\middle|\,\frac{i\rho^2 k\mu}{4z_o}\right)\right\} $$

$$ \left. - \text{Re}\left\{ \frac{\left(-iz_o/k\mu\right)^{-(\mu+1)}\left(\frac{\rho}{2}\right)^{2\mu+\frac{11}{3}}\Gamma\left(-\mu-\frac{11}{6}\right)}{2\,\Gamma\left(\mu+\frac{17}{6}\right)}\ {}_1F_2\left(\mu+1\,\middle|\,\mu+\frac{17}{6},\,\mu+\frac{17}{6}\,\middle|\,\frac{i\rho^2 k\mu}{4z_o}\right)\right\}\right] $$

$$ = A\,\frac{\sqrt{3}}{8}\,\Gamma\left(\frac{8}{3}\right) k^{7/6}\,(z_o/\mu)^{5/6} \left[\frac{\Gamma\left(-\frac{5}{6}\right)}{\Gamma\left(\frac{11}{6}\right)}\left(\frac{\rho^2 k\mu}{4z_o}\right)^{5/6} \right. $$

$$ \left. - \text{Re}\left\{ e^{-i5\pi/12}\,\frac{\Gamma\left(-\frac{5}{6}\right)\Gamma\left(\mu+\frac{11}{6}\right)}{\Gamma(\mu+1)}\ {}_1F_2\left(-\frac{5}{6}\,\middle|\,-\frac{5}{6}-\mu,\,1\,\middle|\,\frac{i\rho^2 k\mu}{4z_o}\right)\right.\right. $$

$$+ e^{-i(\mu+1)\pi/2} \frac{\Gamma\left(-\mu-\frac{11}{6}\right)}{\Gamma\left(\mu+\frac{17}{6}\right)} \left(\frac{\rho^2 k\mu}{4z_o}\right)^{\mu+\frac{11}{6}} {}_1F_2\left(\mu+1 \,\middle|\, \mu+\frac{17}{6}, \mu+\frac{17}{6} \,\middle|\, \frac{i\rho^2 k\mu}{4z_o}\right)\Bigg\}\Bigg] \tag{4.14}$$

Using the power series (4.13) for the hypergeometric function, the correlation function (4.14) (with A = 1 $cm^{1/3}$) has been calculated on the CDC 6500 digital computer. The results of the computation for μ = 1, 2, and 4 are shown plotted as a function of $\rho^2 k/4z_o$ in Fig. 12. The μ = 1, 2, 4 correlation functions have been magnified 100 times for $\rho^2 k/4z_o \geq 15$, 8 and 7, respectively, and the curves calculated to $\rho_m^2 k/4z_o$ = 100, 58 and 27, respectively. It was not possible to calculate the correlation functions for μ = 2 and larger, to large values of $\rho^2 k/4z_o$ using the power series (4.13). To calculate for larger μ's and larger $\rho^2 k/4z_o$ requires use of asymptotic expansions which are apparently not in the literature for the ${}_1F_2$ hypergeometric function. We hope to obtain them in the future to make possible calculation of correlation functions for profiles with sharper peaks (but not so sharp as the delta-function, $\mu = \infty$). We see by comparing the correlation functions shown in Fig. 12 (μ = 1, 2, 4) and Fig. 1 ($\mu = \infty$) that the functions have more oscillations in their tails as μ increases. The value of ρ at the first zero-crossing decreases as μ increases, varying from $\rho^2 k/4z_o$ = 3.2 for μ=1 to $\rho^2 k/4z_o$ = 1.07 for $\mu=\infty$.

The functions S(z) corresponding to Eq. (4.1) were obtained using tables of incomplete gamma functions and are shown in Fig. 13. In the limit $\mu\to\infty$, the profile of Eq. (4.1) becomes a delta function,

$$\lim_{\mu\to\infty} \frac{A}{z_o \Gamma(\mu)} \left(\frac{\mu z}{z_o}\right)^{\mu} e^{-\mu z/z_o} = A\,\delta(z-z_o). \tag{4.15}$$

Consequently, the correlation function of Eq. (4.14) must become the correlation function of Eq. (3.1) in the limit $\mu\to\infty$.

We now demonstrate that this is actually the case. The first term in Eq. (4.14) is

$$A\frac{\sqrt{3}}{8}\,\Gamma\left(\frac{8}{3}\right) k^{7/6}\, z_o^{5/6} \frac{\Gamma\left(-\frac{5}{6}\right)}{\Gamma\left(\frac{11}{6}\right)} \left(\frac{\rho^2 k}{4z_o}\right)^{5/6}, \tag{4.16}$$

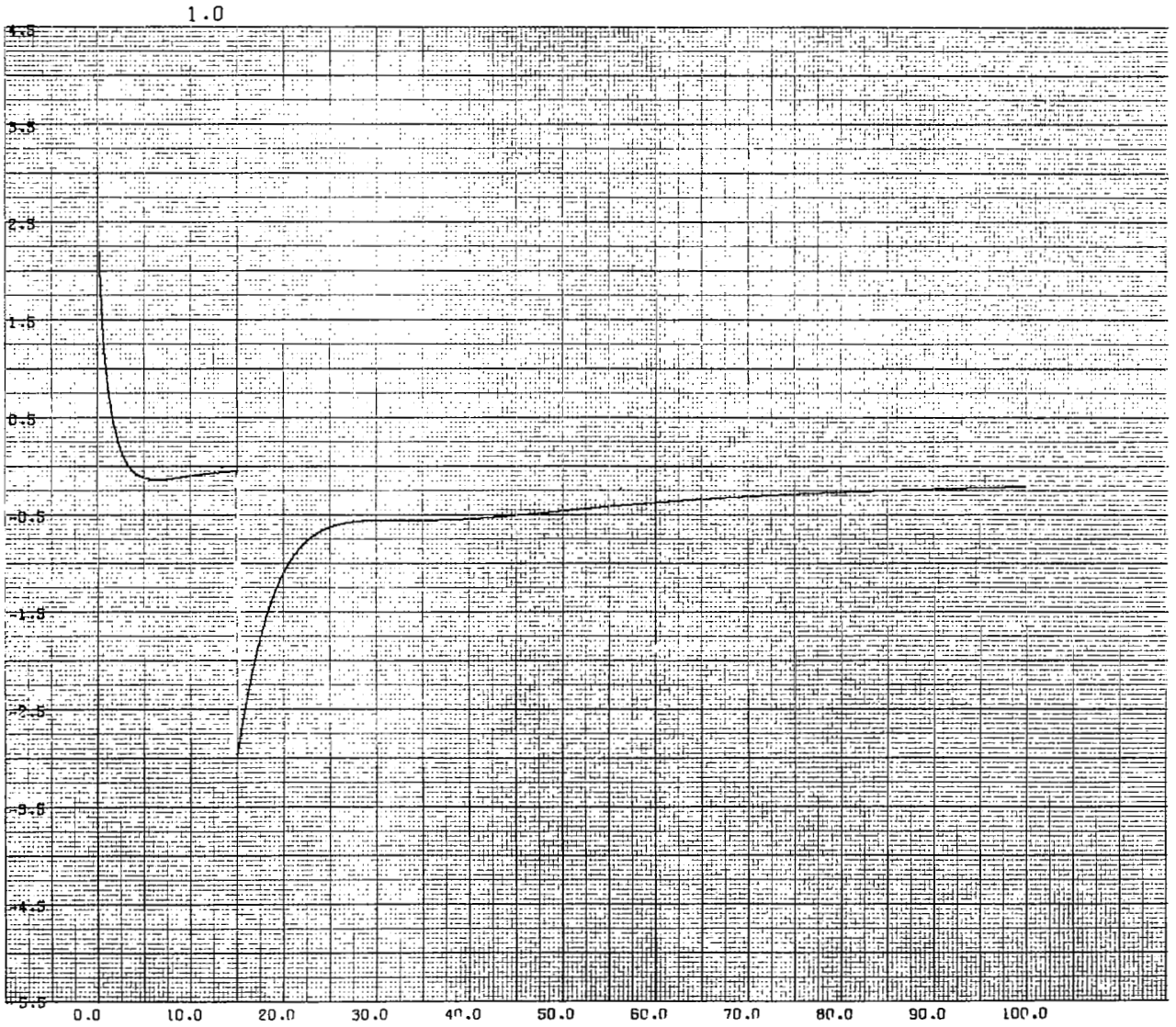

Figure 12a. The logarithmic-amplitude correlation function, $B_\chi(\rho)$, for $C_n^2(z) \sim (z/z_o)\exp(-z/z_o)$ versus $\rho^2 k/4z_o$ (vertical scale arbitrary, 100X magnification for $\rho^2 k/4z_o > 15$).

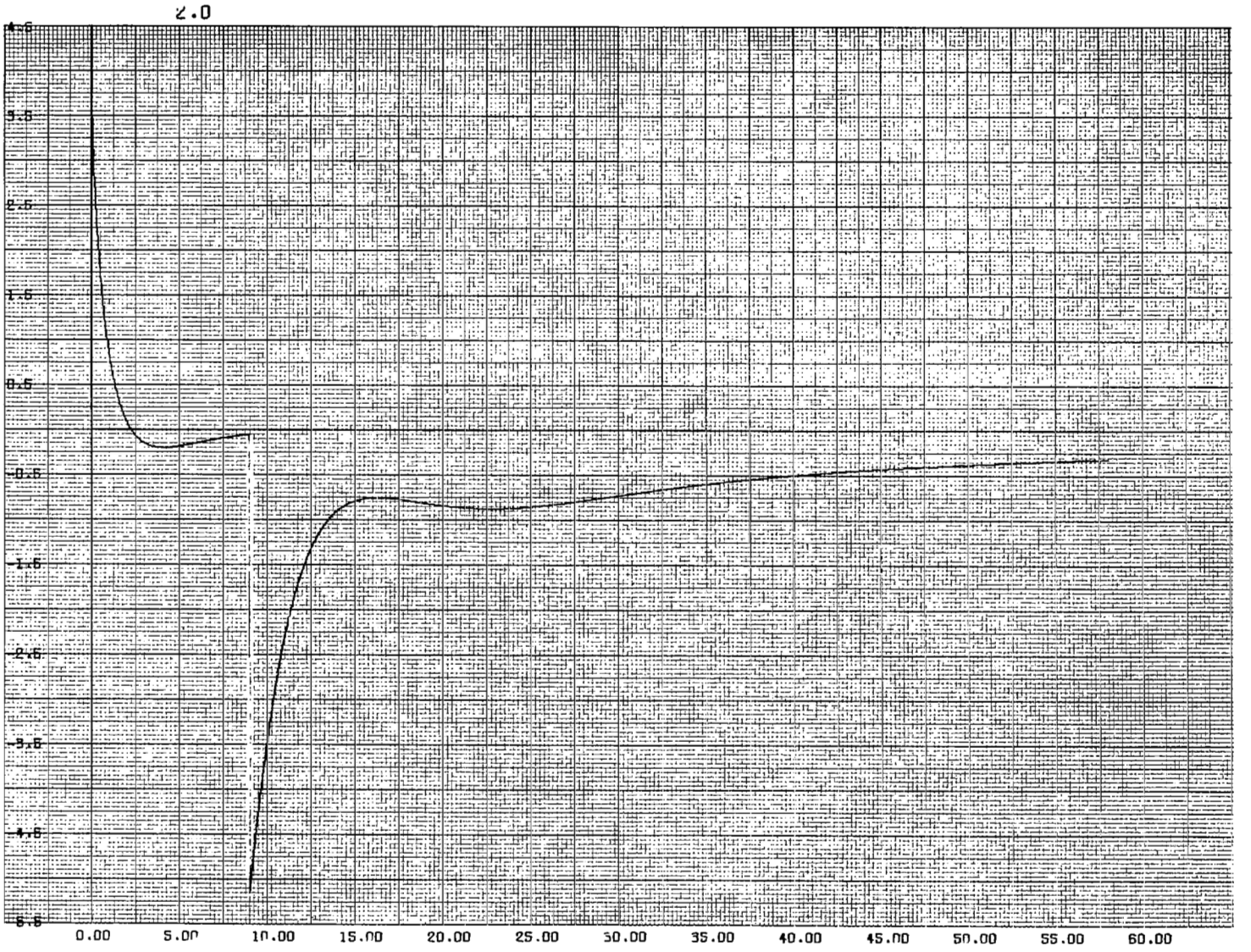

Figure 12b. The logarithmic-amplitude correlation function, $B_\chi(\rho)$, for $C_n^2(z) \sim (z/z_o)^2 \exp(-2z/z_o)$ versus $\rho^2 k/4z_o$ (vertical scale arbitrary, 100X magnification for $\rho^2 k/4z_o > 9$).

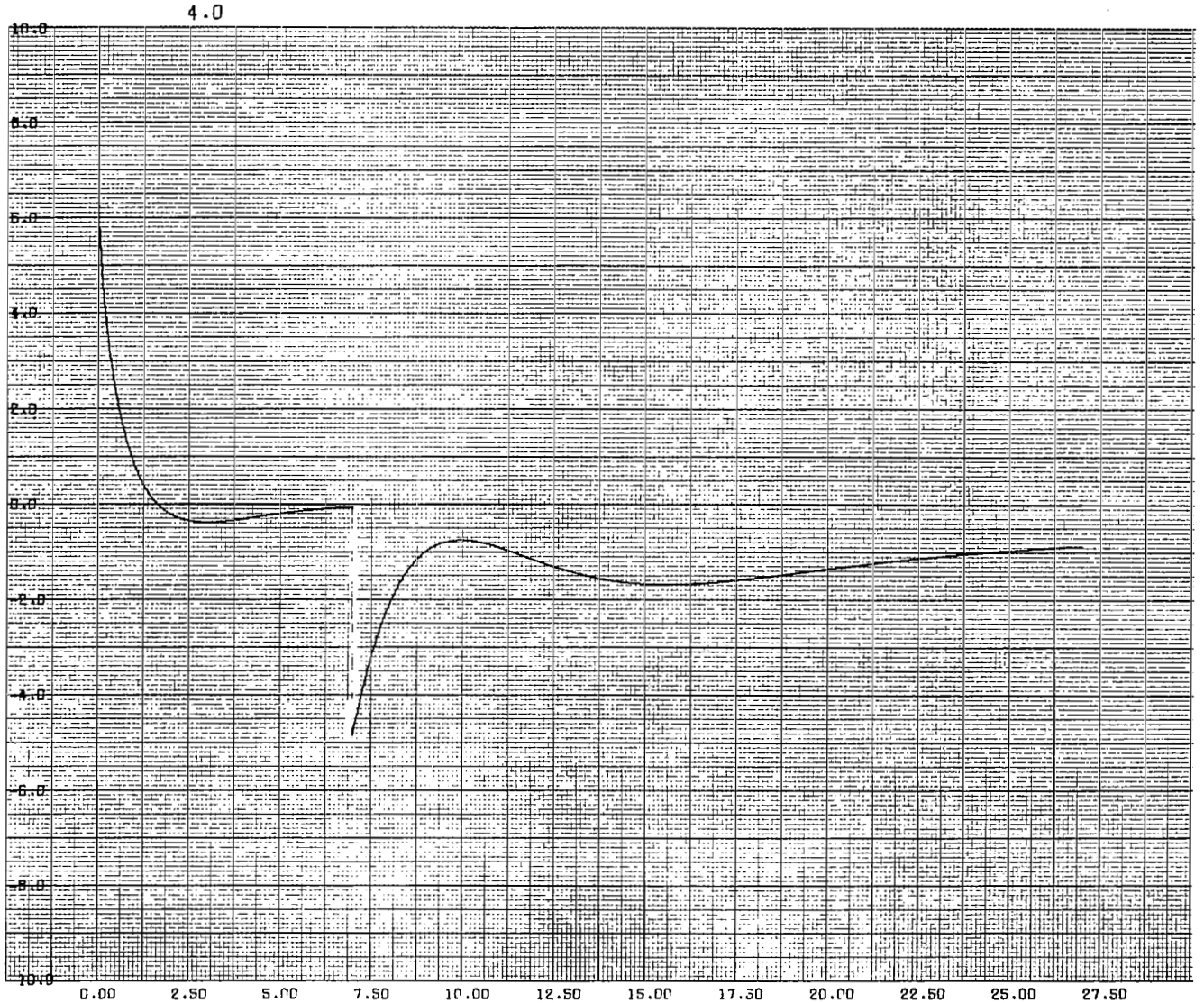

Figure 12c. The logarithmic-amplitude correlation function, $B_\chi(\rho)$, for $C_n^2(z) \sim (z/z_o)^4 \exp(-4z/z_o)$ versus $\rho^2 k/4z_o$ (vertical scale arbitrary, 100X magnification for $\rho^2 k/4z_o > 7$).

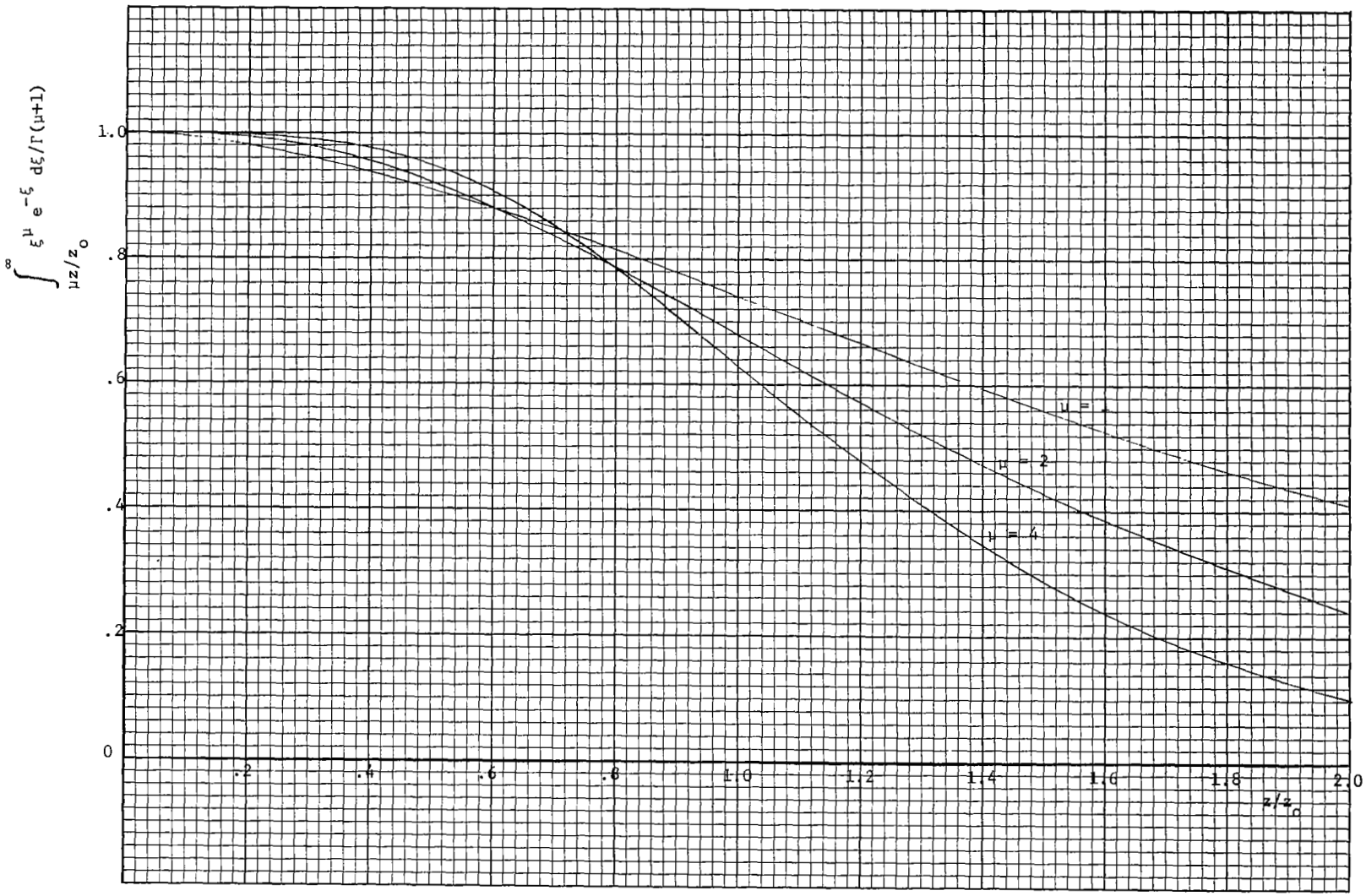

Figure 13. The incomplete gamma function $\int_{\mu z/z_o}^{\infty} \xi^{\mu} e^{-\xi} d\xi/\Gamma(\mu+1)$ versus z/z_o for $\mu = 1$, 2, and 4.

which is seen to be identical to the second term of Eq. (3.1), if we note that

$$\frac{\Gamma\left(-\frac{5}{6}\right)}{\Gamma\left(\frac{11}{6}\right)} = \frac{-\frac{6}{5}\,\Gamma\left(\frac{1}{6}\right)}{\frac{5}{6}\,\Gamma\left(\frac{5}{6}\right)} = -\frac{18}{25\pi}\,\Gamma^2\left(\frac{1}{6}\right).$$

The μ-dependent part of the second term in Eq. (4.14) is

$$\mu^{-5/6}\,\frac{\Gamma\left(\mu+\frac{11}{6}\right)}{\Gamma(\mu+1)}\;{}_1F_2\left(-\frac{5}{6}\,\middle|\,-\frac{5}{6}-\mu,\,1\,\middle|\,\frac{i\rho^2 k\mu}{4z_o}\right)$$

$$= \mu^{-5/6}\,\frac{\Gamma\left(\mu+\frac{11}{6}\right)}{\Gamma(\mu+1)}\sum_{n=0}^{\infty}\frac{\left(-\frac{5}{6}\right)_n}{\left(-\frac{5}{6}-\mu\right)_n}\,\frac{1}{(n!)^2}\left(\frac{i\rho^2 k\mu}{4z_o}\right)^n \qquad (4.17)$$

For large μ we obtain

$$\lim_{\mu\to\infty}\frac{\mu^n}{\left(-\frac{5}{6}-\mu\right)_n} = (-1)^n, \qquad (4.18)$$

and, using Stirling's formula,

$$\lim_{\mu\to\infty}\mu^{-5/6}\,\frac{\Gamma\left(\mu+\frac{11}{6}\right)}{\Gamma(\mu+1)} = \lim_{\mu\to\infty}\mu^{-5/6}\,e^{-5/6}\,\frac{\left(\mu+\frac{11}{6}\right)^{\mu+\frac{4}{3}}}{(\mu+1)^{\mu+\frac{1}{2}}}$$

$$= \lim_{\mu\to\infty} e^{-5/6}\,\frac{\left(\mu+\frac{11}{6}\right)^{\mu}}{(\mu+1)^{\mu}}$$

$$= \lim_{\mu\to\infty} e^{-5/6}\left(1+\frac{5}{6\mu}\right)^{\mu}$$

$$= \lim_{\nu\to\infty} e^{-5/6}\left(1+\frac{1}{\nu}\right)^{\frac{5}{6}\nu}$$

$$= 1, \qquad (4.19)$$

where we obtained the last equality using the relation $\lim_{x\to\infty}\left(1+\frac{1}{x}\right)^x = e$.

Substituting the limits of Eq. (4.18) and (4.19) in Eq. (4.17) we find

$$\lim_{\mu\to\infty} \mu^{-5/6} \frac{\Gamma\left(\mu+\frac{11}{6}\right)}{\Gamma(\mu+1)} {}_1F_2\left(-\frac{5}{6}\,\middle|\,-\frac{5}{6}-\mu, 1\,\middle|\, \frac{i\rho^2 k\mu}{4z_o}\right)$$

$$= \sum_{n=0}^{\infty} \left(-\frac{5}{6}\right)_n \frac{1}{(n!)^2} \left(\frac{-i\rho^2 k}{4z_o}\right)^n$$

$$= F\left(-\frac{5}{6}\,|1|\, \frac{-i\rho^2 k}{4z_o}\right), \qquad (4.20)$$

where $F(a\,|\,b\,|\,w) = {}_1F_1(a\,|\,b\,|\,w)$ is the confluent hypergeometric (Kummer) function. Substituting (4.20) in Eq. (4.14), we obtain for the second term in Eq. (4.14) in the limit of large μ,

$$-A\frac{\sqrt{3}}{8}\Gamma\left(\frac{8}{3}\right)k^{7/6} z_o^{5/6}\Gamma\left(-\frac{5}{6}\right) \mathrm{Re}\left\{e^{-i5\pi/12} F\left(-\frac{5}{6}\,|1|\, \frac{-i\rho^2 k}{4z_o}\right)\right\}$$

$$= A\frac{3\sqrt{3}}{20}\Gamma\left(\frac{8}{3}\right)k^{7/6} z_o^{5/6}\Gamma\left(\frac{1}{6}\right) \mathrm{Re}\left\{e^{i5\pi/12} F\left(-\frac{5}{6}\,|1|\, \frac{i\rho^2 k}{4z_o}\right)\right\}, \qquad (4.21)$$

where we have noted that $-\frac{5}{6}\Gamma\left(-\frac{5}{6}\right) = \Gamma\left(\frac{1}{6}\right)$, and have taken the complex conjugate of the quantity in brackets to obtain the equality. Since $e^{i5\pi/12} = -e^{-i7\pi/12}$, Eq. (4.21) is identical to the first term in Eq. (3.1). Thus, the first two terms in Eq. (4.14), in the limit $\mu\to\infty$, reduce to Eq. (3.1). It is now necessary to show that the last term in Eq. (4.14) vanishes in the limit $\mu\to\infty$, and therefore Eq. (4.14) in the limit $\mu\to\infty$ reduces to Eq. (3.1).

The limit of the μ-dependent part of the third term in Eq. (4.14) is

$$\lim_{\mu\to\infty} e^{-i\mu\pi/2}\, \mu^{\mu+1} \frac{\Gamma\left(-\mu-\frac{11}{6}\right)}{\Gamma\left(\mu+\frac{17}{6}\right)} {}_1F_2\left(\mu+1\,\middle|\, \mu+\frac{17}{6}, \mu+\frac{17}{6}\,\middle|\, \frac{i\rho^2 k\mu}{4z_o}\right)$$

$$= \lim_{\mu\to\infty} \frac{\pi\, e^{-i\mu\pi/2}\, \mu^{\mu+1}}{\sin\pi\left(\mu+\frac{5}{6}\right)\Gamma^2\left(\mu+\frac{17}{6}\right)} \sum_{n=0}^{\infty} \frac{(\mu+1)_n}{\left[\left(\mu+\frac{17}{6}\right)_n\right]^2} \frac{1}{n!}\left(\frac{i\rho^2 k\mu}{4z_o}\right)^n \qquad (4.22)$$

The $\mu \to \infty$ limit of the sum in (4.22) is

$$\sum_{n=0}^{\infty} \frac{1}{n!} \left(\frac{i\rho^2 k}{4z_o} \right)^n = e^{i\rho^2 k/4z_o} .$$

Using Stirling's formula,

$$\Gamma^2 \left(\mu + \frac{17}{6} \right) \sim 2\pi \, e^{-2\mu - 17/3} \left(\mu + \frac{17}{6} \right)^{2\mu + \frac{14}{3}}$$

$$\sim 2\pi \, e^{-2\mu - 17/3} \left(1 + \frac{17}{6\mu} \right)^{2\mu} \mu^{2\mu + \frac{14}{3}}$$

$$\sim 2\pi \, e^{-2\mu} \, \mu^{2\mu + \frac{14}{3}} ,$$

so that the limit of Eq. (4.22) is

$$\lim_{\mu \to \infty} \frac{1}{2} \csc \pi \left(\mu + \frac{5}{6} \right) e^{i\rho^2 k/4z_o} \, e^{-i\mu\pi/2} \, e^{2\mu} \, \mu^{-\mu - \frac{11}{3}} = 0 . \qquad (4.23)$$

B. Numerical Inversion of Equation (4.14)

The results of the numerical inversion of the correlation function (4.14) with $\mu = 1$, 2, and 4 are shown in Fig. 14, 15, and 16, respectively as functions of $\rho_m^2 k/4z_o$. The calculations are shown for $z/z_o = 0.1$ and 1.0. The number of summands in the calculations was 2,001. The upper curves (right-hand scale) are the inversions of Eq. (1.10); the lower curves (left-hand scale) are the inversions of Eq. (3.10), with

$$\int_o^{\infty} z^2 C_n^2(z) dz = z_o^2 (\mu+1)(\mu+2)/\mu^2 .$$

The improvement in convergence using Eq. (3.10) rather than (1.10) is apparently more significant in these calculations than it was in the delta-function case. The reason is that the relatively less oscillatory correlation functions (4.14) for the smooth profiles, are more closely represented for large ρ by the first term in their asymptotic expansions, (1.11), than is the more oscillatory delta-function correlation function, (3.1). Consequently, the

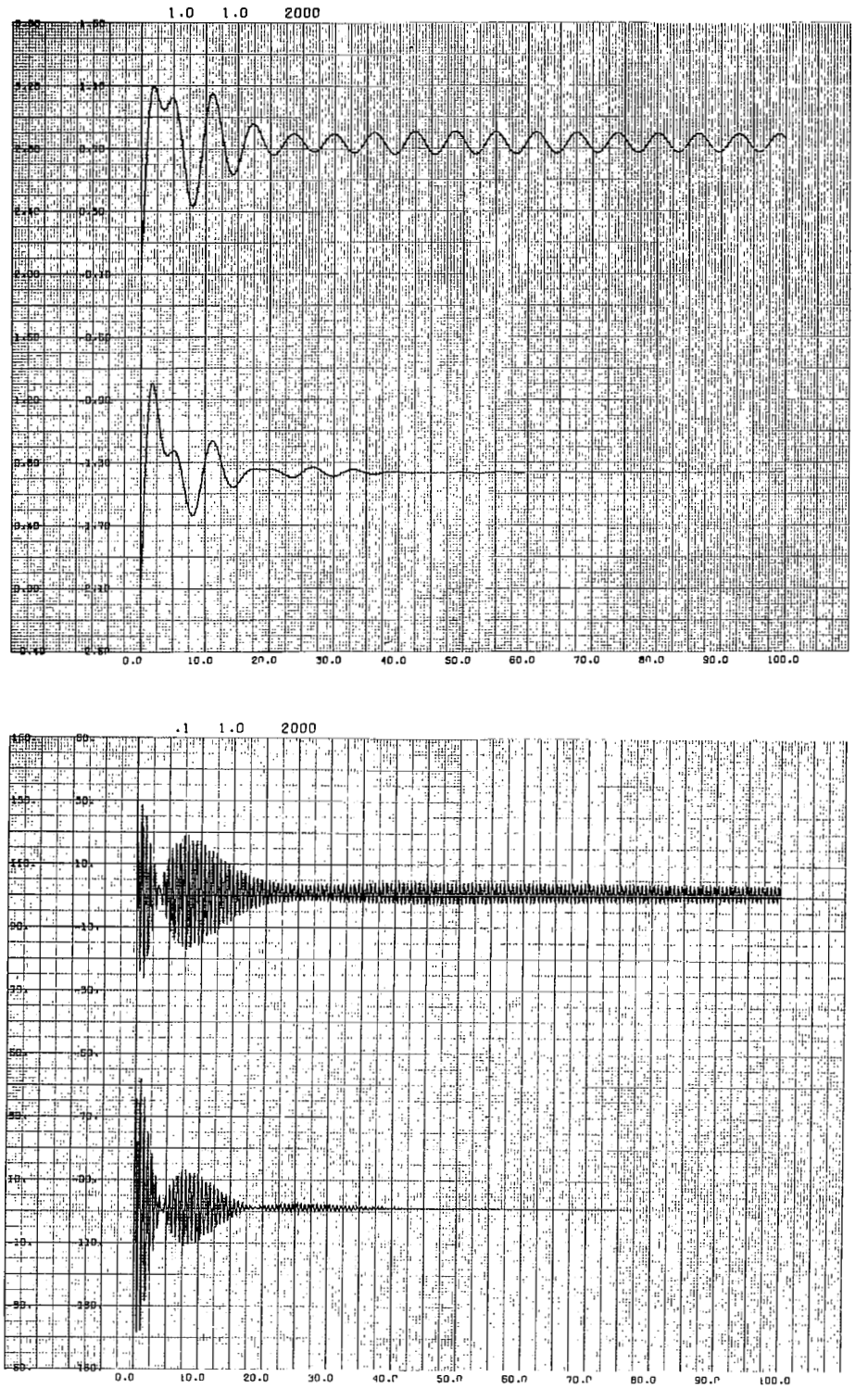

Figure 14. Calculated integrated turbulence profile for $\mu = 1$ versus $\rho_m^2 k/4z_o$. (a) $z/z_o = 0.1$, (b) $z/z_o = 1.0$.

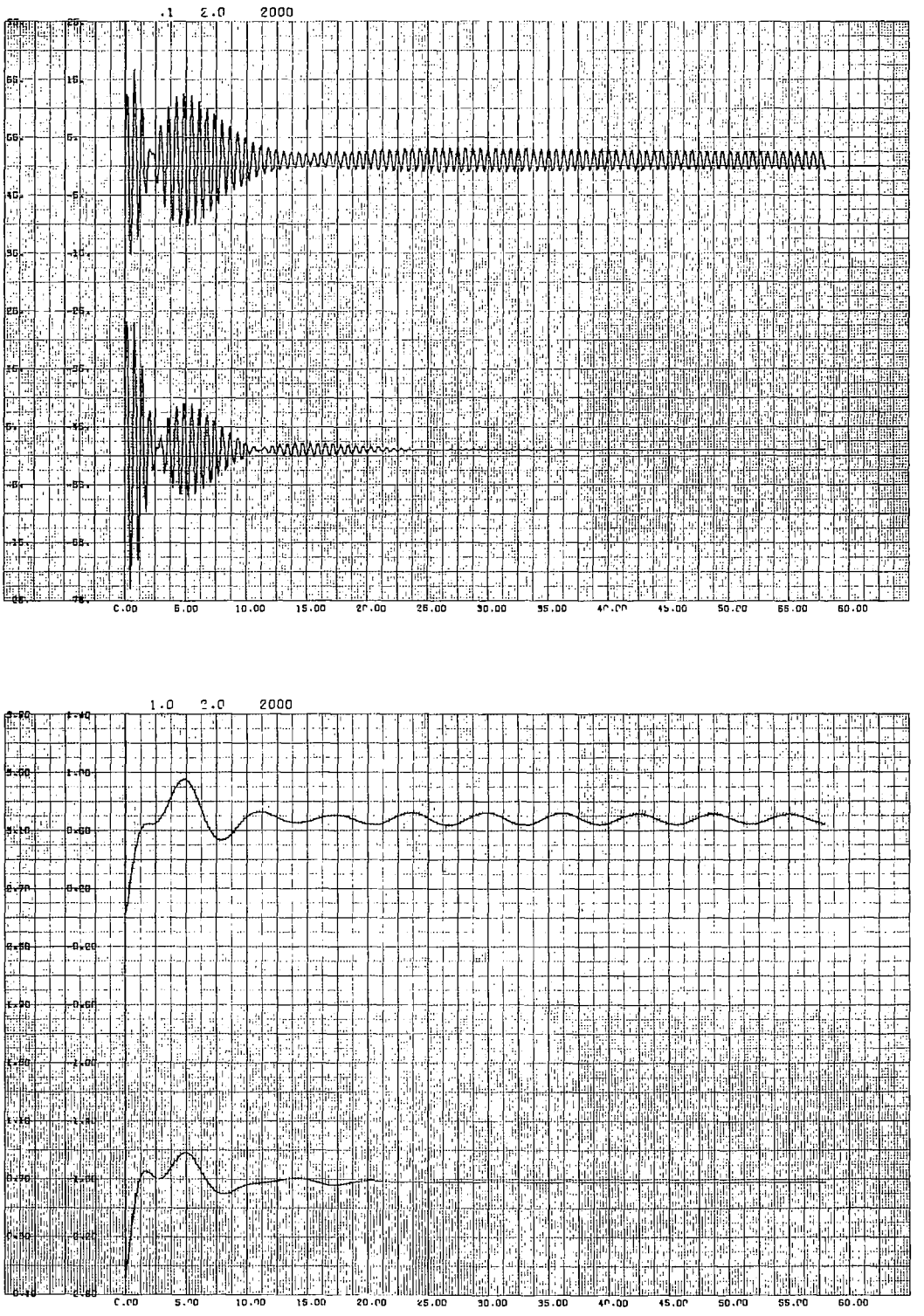

Figure 15. Calculated integrated turbulence profile for $\mu = 2$ versus $\rho_m^2 k/4z_o$. (a) $z/z_o = 0.1$, (b) $z/z_o = 1.0$.

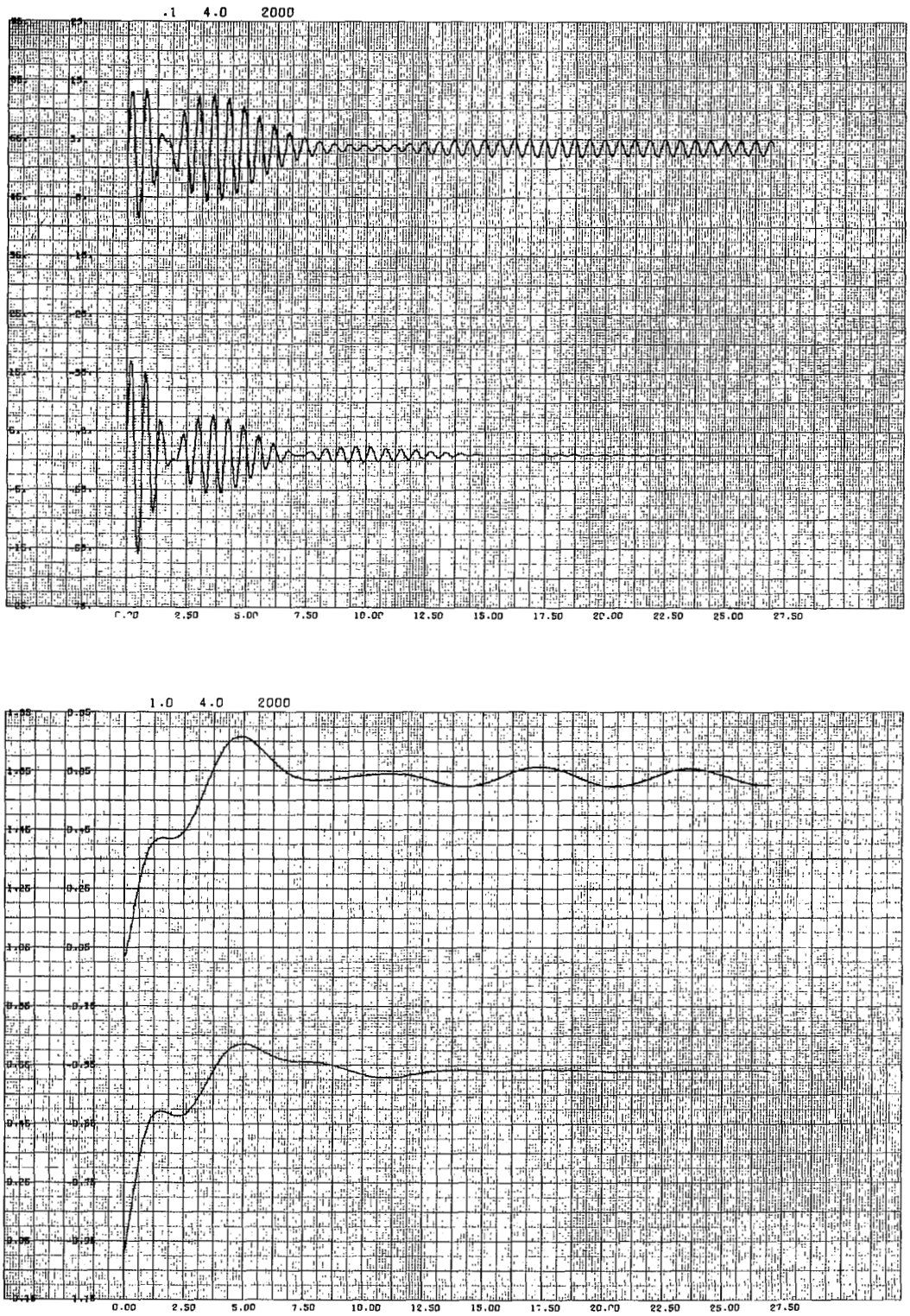

Figure 16. Calculated integrated turbulence profile for $\mu = 4$ versus $\rho_m^2 k/4z_o$. (a) $z/z_o = 0.1$, (b) $z/z_o = 1.0$.

second term in Eq. (3.10) is a better approximation to the portion of the integral in Eq. (1.10) from ρ_m to ∞ when applied to the smooth profile case than to the delta-function case.

The large-ρ limit of the twelve lower curves in Figs. 14-16 fit exactly, within the precision of the calculations, on the integrated profile curves shown in Fig. 13. It can be seen that the calculation of the smooth profiles from Eq. (3.10) shown in Figs. 14-16 converges for much smaller values of ρ_m than the calculation of the delta-function case shown in Figs. 3a-3h. This is in general accord with Eq. (3.12), which predicts that the value of ρ_m required for convergence of Eq. (3.10) decreases as the profile becomes smoother.

However, the μ = 1, 2, and 4 profiles shown in Fig. 11 are outside the range of validity of Eq. (3.12). For these profiles, $D/z_o > 1$, and Eq. (3.12) would predict $\rho_m^2 k/4z_o < 4$. Clearly, there is a lower limit on the value of $\rho_m^2 k/4z_o$ for which Eq. (3.12) is applicable. We would expect that it could not be valid when it predicts ρ_m of the order of ρ_1, the first zero-crossing of the correlation function.

We observe from Figs. 14-16 that the required ρ_m actually increases as μ decreases from μ = 4 to μ = 1. This is evidently because ρ_1^2 increases from 1.6 $(4z_o/k)$ to 3.2 $(4z_o/k)$ as μ varies from 4 to 1. The asymptotic value for large μ (Fig. 1) is $\rho_1^2 = 1.07\ (4z_o/k)$. It would be of interest to carry out the inversion for larger values of μ in order to verify the asserted applicability of Eq. (3.12) to smooth profiles. In the range $8 < \mu < 800$ the width D, between the 1/e times maximum points of the profile (4.1), is in the range $1 > D > 0.1$, according to Eq. (4.5). An attempt will be made in the future to calculate the correlation function (4.14) by obtaining asymptotic formulas for ${}_1F_2\ (\mu+1 \,|\, \mu+17/6, \mu+17/6 \,|\, i\mu y)$ and ${}_1F_2\ (-5/6 \,|\, -5/6 - \mu,\ 1 \,|\, i\mu y)$ for large μ.

V. NOISE

A. Derivation of Relation between Noise in S(z) and $B_\chi(\rho)$

In Sections III and IV we considered the effect of truncating $B_\chi(\rho)$ at ρ_m, a finite value of ρ. The result was a loss in spatial resolution in the calculated profile S(z) as given by Eq. (3.12). It is necessary to truncate in any practical application, because $B_\chi(\rho)$ becomes small for large ρ (see Figs. 1 and 12 and Eq. (1.7)) and eventually, for $\rho > \rho_m$, the noise in the measurement of $B_\chi(\rho)$ dominates the signal. In the above analysis, however, we have not included the effect of noise in $B_\chi(\rho)$ for $\rho < \rho_m$, or given any considerations to the determination of the value of ρ_m which should be used in a practical application of Eq. (3.10) for calculating real turbulence profiles. We do so in this section, by deriving a relation between the error in the calculated S(z) and the noise in $B_\chi(\rho)$.

An experimentally obtained correlation function consists of a sum of the correlation function, $B_\chi(\rho)$, and noise, $N(\rho)$. If we define $\delta S(z)$ to be the error in S(z) resulting from the noise, then from Eqs. (3.10) and (3.11) we obtain

$$\delta S(z) = \frac{8k^{-1/6}}{\pi\sqrt{3}\,\Gamma\left(\frac{8}{3}\right)}\left[\Gamma\left(\frac{11}{6}\right)z^{-11/6}\int_0^{\rho_m} d\rho\ \rho N(\rho)\ \mathrm{Im}\left\{e^{i\pi/12}\ F\left(\frac{11}{6}\,|1|\,\frac{i\rho^2 k}{4z}\right)\right\}\right.$$

$$+\ \frac{\Gamma^2\left(\frac{7}{6}\right)\Gamma\left(\frac{5}{6}\right)}{\pi^2 z^2}\left(\frac{\rho_m^2 k}{4z}\right)^{-1/3}\sin\left(\frac{\rho_m^2 k}{4z}\right)\int_0^{\infty} dz'\, z'^{-5/6}\int_0^{\rho_m} d\rho\ \rho N(\rho)$$

$$\left.\mathrm{Im}\left\{e^{i\pi/12}\ F\left(\frac{5}{6}\,|1|\,\frac{i\rho^2 k}{4z}\right)\right\}\right] \qquad (5.1)$$

The mean-square error in S(z) is found by squaring and averaging Eq. (5.1).

$$
\begin{aligned}
\langle [\delta S(z)]^2 \rangle = {} & \left(\frac{8k^{-1/6}\,\Gamma\left(\frac{11}{6}\right) z^{-11/6}}{\pi\sqrt{3}\,\Gamma\left(\frac{8}{3}\right)} \right)^2 \int_0^{\rho_m} d\rho \int_0^{\rho_m} d\rho' \langle N(\rho) N(\rho') \rangle Q\left(\frac{11}{6}; \rho, \frac{11}{6}, \rho'\right) \\
& + \left(\frac{\Gamma^2\left(\frac{7}{6}\right)\Gamma\left(\frac{5}{6}\right)}{\pi^2 z^2} \left(\frac{\rho_m^2 k}{4z}\right)^{-1/3} \sin\left(\frac{\rho_m^2 k}{4z}\right) \right)^2 \int_0^{\infty} dz' z'^{-5/6} \int_0^{\infty} dz'' z''^{-5/6} \\
& \int_0^{\rho_m} d\rho \int_0^{\rho_m} d\rho' \cdot Q\left(\frac{5}{6}, \rho; \frac{5}{6}, \rho'\right) \langle N(\rho)\, N(\rho') \rangle \\
& + \frac{40k^{-1/6}\,\Gamma^2\left(\frac{5}{6}\right) z^{-11/6}\,\Gamma^2\left(\frac{7}{6}\right)}{3\pi^3\sqrt{3}\,\Gamma\left(\frac{8}{3}\right) z^2} \left(\frac{\rho_m^2 k}{4z}\right)^{-1/3} \sin\left(\frac{\rho_m^2 k}{4z}\right) \\
& \cdot \int_0^{\infty} dz' z'^{-5/6} \int_0^{\rho_m} d\rho \int_0^{\rho_m} d\rho' \langle N(\rho) N(\rho') \rangle Q\left(\frac{11}{6}, \rho; \frac{5}{6}, \rho'\right),
\end{aligned}
\tag{5.2}
$$

where we have introduced the quantity

$$
Q(a, \rho; b, \rho') = \rho\rho' \operatorname{Im}\left\{ e^{i\pi/12} F\left(a \,|\, 1 \,|\, \frac{i\rho^2 k}{4z}\right) \right\} \operatorname{Im}\left\{ e^{i\pi/12} F\left(b \,|\, 1 \,|\, \frac{i\rho'^2 k}{4z}\right) \right\}
\tag{5.3}
$$

In a practical application, the ρ integrals in Eq. (5.2) are replaced by sums. If we assume that the correlation function is sampled at the points

$$
\rho_j = j\Delta\rho,
\tag{5.4}
$$

where j takes on integral values between 0 and $m = \rho_m/\Delta\rho$, and $\Delta\rho$ is the spacing between points, the first double integral in Eq. (5.2) becomes

$$\int_0^{\rho_m} d\rho \int_0^{\rho_m} d\rho' \langle N(\rho)\, N(\rho')\rangle\, Q\left(\frac{11}{6}, \rho; \frac{11}{6}, \rho'\right)$$

$$\approx \sum_{j=0}^{M} \sum_{\ell=0}^{M} \langle N(\rho_j)\, N(\rho_\ell)\rangle\, Q\left(\frac{11}{6}, \rho_j; \frac{11}{6}, \rho_\ell\right) (\Delta\rho)^2. \qquad (5.5)$$

To obtain Eq. (5.5), we have assumed the spacing to be uniform in ρ since, as was stated in Sec. 3, we expect this to give improved spatial resolution compared to uniform ρ^2 spacing, for a given number of sample points, m. We assume in Eq. (5.5) a simpler trapezoidal summation approximation, rather than Simpson's rule which was used in our computer calculations, but we do not expect this to effect the results significantly.

Before proceeding further, to evaluate the summation (5.5) it is necessary to assume a functional form for the noise autocorrelation function $\langle N(\rho_j)\, N(\rho_\ell)\rangle$. If the noise at distinct sample points is uncorrelated, then

$$\langle N(\rho_j)\, N(\rho_\ell)\rangle = \nu^2(\rho_j)\, \delta_{j\ell} \qquad (5.6)$$

where $\delta_{j\ell}$ is the Kronecker delta and ν is the rms noise amplitude at ρ. Equation (5.6) is a correct description for example, if $B_\chi(\rho_j)$ and $B_\chi(\rho_\ell)$ are measured with two distinct pairs of photomultipliers. It is also a correct description if the logarithmic amplitude χ is recorded on a photographic film (as in our laboratory experiment described in Sec. VI) for which the grain size is small compared to the spacing $\Delta\rho$.

Substituting Eq. (5.6) in Eq. (5.5) one of the sums can be evaluated, resulting in the single sum

$$(\Delta\rho)^2 \sum_{j=0}^{M} \nu^2(\rho_j)\, Q\left(\frac{11}{6}, \rho_j; \frac{11}{6}, \rho_j\right)$$

$$\approx \Delta\rho \int_0^{\rho_m} d\rho\, \nu^2(\rho)\, Q\left(\frac{11}{6}, \rho; \frac{11}{6}, \rho\right) \qquad (5.7)$$

The sum in (5.7) is approximated by an integral. From the definition (5.3) and the asymptotic formula (3.5) it is seen that Q is proportional to $\rho^{16/3}$ for large ρ. Thus, unless $\nu^2(\rho)$ is proportional to a large negative power of ρ, the integral in Eq. (5.7) is dominated by values of ρ near ρ_m, where the asymptotic formula (3.5) is valid. We thus can approximate Q by its asymptotic form. Similarly, we can approximate $\nu^2(\rho)$ in the integrand by

$$\nu^2 = \nu^2(\rho_m) . \tag{5.8}$$

With these assumptions, we obtain for the right-hand side of Eq. (5.7),

$$\nu^2 \Delta\rho \int_0^{\rho_m} d\rho \left[\rho \operatorname{Im}\left\{e^{i\pi/12} F\left(\frac{11}{6} \,|1|\, \frac{i\rho^2 k}{4z}\right)\right\}\right]^2$$

$$\sim \nu^2 \Delta\rho \int_0^{\rho_m} d\rho \left[\frac{\rho}{\Gamma(11/6)} \left(\frac{\rho^2 k}{4z}\right)^{5/6} \sin\left(\frac{\rho^2 k}{4z}\right)\right]^2$$

$$\sim \nu^2 \Delta\rho \frac{1}{\Gamma^2(11/6)} \left(\frac{k}{4z}\right)^{5/3} \int_0^{\rho_m} d\rho\, \rho^{16/3} \frac{1}{2}\left(1 - \cos\frac{\rho^2 k}{2z}\right)$$

$$\sim \nu^2 \Delta\rho \frac{1}{\Gamma^2(11/6)} \left(\frac{k}{4z}\right)^{5/3} \left(\frac{3}{38}\right) \rho_m^{19/3} . \tag{5.9}$$

Using Eqs. (5.5), (5.7), and (5.9), we obtain for the first term in Eq. (5.2)

$$\frac{512\, k^{-7/3} z^{-5/3} \nu^2 (\Delta\rho/\rho_m) \left(\rho_m^2 k/4z\right)^{11/3}}{19\, \pi^2 \Gamma^2 (8/3)} . \tag{5.10}$$

The same calculation has been done for uniform spacing, $\Delta\rho^2$, in ρ^2 by making the appropriate modification to the finite sum approximation in Eq. (5.5). The corresponding result for the first term in Eq. (5.2) is

$$\frac{16\, k^{-7/3} z^{-5/3} \nu^2 \left(\Delta\rho^2/\rho_m^2\right) \left(\rho_m^2 k/4z\right)^{11/3}}{\pi^2 \Gamma^2 (8/3)} , \tag{5.10'}$$

which is 0.6 times as large as (5.10).

We have repeated the procedure of Eqs. (5.4) through (5.10) to determine the second and third terms in Eq. (5.2), for uniform ρ spacing. We merely give the results, which are

$$\frac{2^{2/3}\,\Gamma^2\left(\frac{7}{6}\right)\,k^{-7/3}\,z^{-5/3}\,\nu^2\,(\Delta\rho/\rho_m)\,\left(\rho_m{}^2 k/4z\right)^{5/3}\,\sin^2\left(\frac{\rho_m{}^2 k}{4z}\right)}{11\,\pi^2\,\Gamma^2\left(\frac{5}{6}\right)\,\Gamma^2\left(\frac{4}{3}\right)}, \tag{5.11}$$

$$\frac{(24)^3\,\Gamma^2\left(\frac{7}{6}\right)\,k^{-7/3}\,z^{-5/3}\,\nu^2\,(\Delta\rho/\rho_m)\,\left(\rho_m{}^2 k/4z\right)^{5/3}\,\sin^2\left(\frac{\rho_m{}^2 k}{4z}\right)}{50\,\pi^4\,\sqrt{3}\,\Gamma\left(\frac{5}{3}\right)}, \tag{5.12}$$

respectively. Expressions (5.11) and (5.12) are of magnitude $0.1(\rho_m{}^2 k/4z)^{-2}$ and $3(\rho_m{}^2 k/4z)^{-2}$ times (5.10), respectively, and hence are negligible compared to (5.10). Taking the square root of (5.10), we therefore have for the rms error in S(z), for uniform increments in ρ,

$$\left[\langle[\delta S(z)]^2\rangle\right]^{1/2} = \frac{16\,\sqrt{2}\,k^{-7/6}\,z^{-5/6}\,\nu\,\left(\rho_m{}^2 k/4z\right)^{11/6}}{\sqrt{19}\,\pi\,\Gamma(8/3)\,\sqrt{m}}, \tag{5.13}$$

and, taking the square root of Eq. (5.10'), for uniform spacing in ρ^2,

$$\left[\langle[\delta S(z)]^2\rangle\right]^{1/2} = \frac{4\,k^{-7/6}\,z^{-5/6}\,\nu\,\left(\rho_m{}^2 k/4z\right)^{11/6}}{\pi\,\Gamma(8/3)\,\sqrt{m}}. \tag{5.13'}$$

According to Eqs. (5.13) and (5.13'), the rms error in S(z) is proportional to the rms noise in $B_\chi(\rho)$, inversely to the square root of the number of sample points $m\left[\rho_m/\Delta\rho\right.$ in Eq. (5.13) and $\rho_m{}^2/(\Delta\rho)^2$ in Eq. (5.13')], and to $\left(\rho_m{}^2 k/4z\right)^{11/6}$.

B. Error in a Calculation of $B_\chi(\rho)$ from a Finite Intensity Record

The correlation function, $B_\chi(\rho)$, is determined by calculating the ensemble, time, or space average indicated by Eq. (1.1). It is necessary to perform the average over a logarithmic-intensity sample of infinite size, if $B_\chi(\rho)$ is to be determined exactly. In practice, one must settle for a finite

sample. The average over a finite sample, ℓ, of the logarithmic-amplitude is denoted by ${}^{\ell}B_{\chi}(\rho)$. The sample function ${}^{\ell}B_{\chi}(\rho)$ is a random function which approaches $B_{\chi}(\rho)$ as the sample size gets larger. The variance $\sigma^2_{B\chi}$ in a set of measurements of ${}^{\ell}B_{\chi}(\rho)$ is related to the sample size of the $\chi(r, t)$ record utilized in each measurement. If a one-dimensional spatial average is performed over a distance L, for a normal random noise process such as $\chi(r, t)$,

$$\sigma_{B_\chi}{}^2(\rho, L) = \frac{2}{L^2} \int_0^L (L-\xi)\left[B_\chi^2(\xi) + B_\chi(\rho+\xi)B_\chi(\rho-\xi)\right]d\xi \quad [11] . \quad (5.14)$$

Equation (5.14) gives the mean-square deviation of the correlation function calculated from a spatial average of a sample of length L, from the true correlation function (calculated from a sample of infinite length).

We will consider the effect of finite sample size on the calculation of the correlation function from empirical intensity data when the turbulence profile is a delta function. In this case, we have found from our numerical computation of $B_{\chi}(\rho)$ that the correlation function $B_{\chi}(\rho)$ has its first zero crossing at $\rho = 1.04\sqrt{4z_o/k}$ and for $\rho >> \sqrt{4z_o/k}$ it falls to zero rapidly (as $\rho^{-7/3}$). If the sample length is large, i.e., $L >> \sqrt{4z_o/k}$, the factor $(L-\xi)$ in Eq. (5.14) may be replaced by L and Eq. (5.14) approximated by,

$$\sigma_{B_\chi}{}^2(\rho, L) = \frac{2}{L} \int_0^L \left[B_\chi^2(\xi) + B_\chi(\rho+\xi)\, B_\chi(\rho-\xi)\right]d\xi . \quad (5.15)$$

Again, since $B_{\chi}(\rho)$ approaches zero rapidly for large ρ, when $\rho >> \sqrt{4z_o/k}$ the second term in brackets in Eq. (5.15) is negligible compared to the first and we obtain for large ρ,

$$\sigma_{B_\chi}{}^2(\rho >> \sqrt{4z_o/k},\ L) = \frac{2}{L} \int_0^L B_\chi{}^2(\xi)\,d\xi = \frac{1}{2}\,\sigma_{B_\chi}{}^2(0, L). \quad (5.16)$$

In obtaining the second equality in Eq. (5.16) we have used the fact that B_{χ} is an even function. The variance $\sigma_{B_\chi}{}^2(\rho, L)$ decreases from its value at $\rho = 0$

to one half that value when $\rho >> \sqrt{4z_o/k}$. If L is large, that is, $L >> \sqrt{4z_o/k}$, the variance becomes inversely proportional to L.

The function $B_\chi^2(\rho)$ for a delta-function turbulence profile is plotted versus $\rho\sqrt{k/4z_o}$ in Fig. 17. A numerical integration of this function yields

$$\sigma_{B_\chi}^2(0, L) = \frac{4}{L}\int_0^\infty B_\chi^2(\xi)\, d\xi = \frac{1.36\ \rho_o}{L} B_\chi^2(0) , \tag{5.17}$$

$$\sigma_{B_\chi}^2(\rho >> \rho_o, L) = \frac{.68\ \rho_o}{L} B_\chi^2(0) , \tag{5.18}$$

where we have defined ρ_o by $\rho_o = \sqrt{4z_o/k}$, and we have set the upper integration limit in Eq. (5.16) equal to infinity, which is a valid approximation for $L >> \rho_o$.

Formulas (5.16), (5.17) and (5.18) allow us to calculate the sample length, L, required for a given standard deviation, σ_{B_χ}, in an experimentally determined correlation function. We would now like to combine this with our earlier results in order to relate L to the standard deviation, $\sigma_S \equiv (\langle(\delta S)^2\rangle)^{1/2}$, in the integrated profile. From Eq. (5.13) we obtain for the ratio of the standard deviation in S(z) to the standard deviation in $B_\chi(\rho)$,

$$\frac{\sigma_S}{\sigma_{B_\chi}} = \frac{16\sqrt{2}\, k^{-7/6}\, z_o^{-5/6} \left(\rho_m^2\, k/4z_o\right)^{11/6}}{19\,\pi\,\Gamma(8/3)\sqrt{m}} \tag{5.19}$$

where we have replaced ν by σ_{B_χ} and let $z = z_o$. From Eq. (3.1) we obtain

$$B_\chi(0) = \frac{3\sqrt{3}}{20} \sin\left(\frac{\pi}{12}\right) \Gamma\left(\frac{8}{3}\right)\Gamma\left(\frac{1}{6}\right) k^{7/6}\, z_o^{5/6}\, S(0) ,$$

where S(0) = A is the total integrated turbulence. Using this formula in Eq. (5.19), we obtain

$$\frac{\sigma_S/S(0)}{\sigma_{B_\chi}/B_\chi(0)} = \frac{12\sqrt{6}}{5\,\pi\sqrt{19}}\Gamma\left(\frac{1}{6}\right)\sin\left(\frac{\pi}{12}\right)\frac{1}{\sqrt{m}}\left(\frac{\rho_m^2\, k}{4z_o}\right)^{11/6} . \tag{5.20}$$

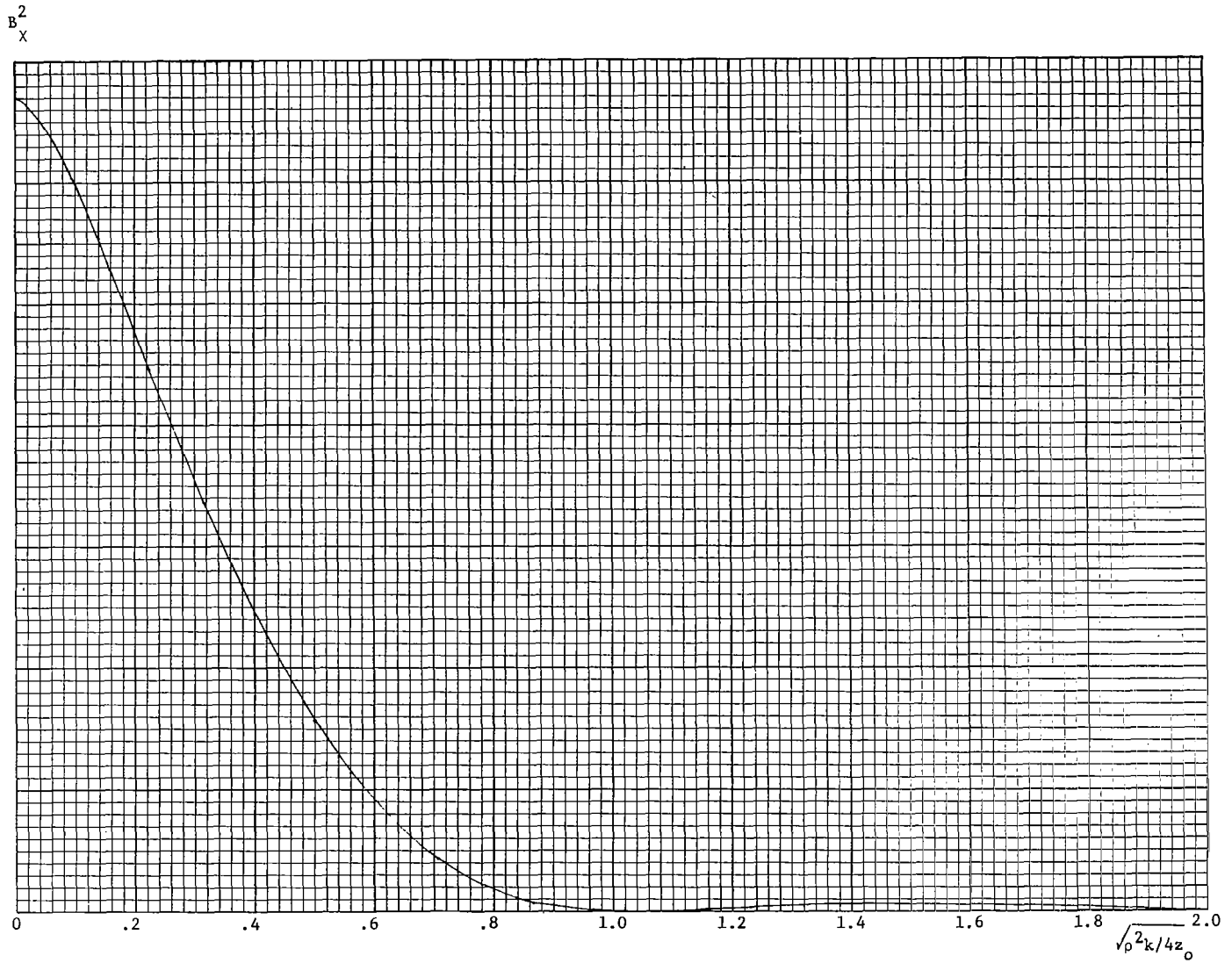

Figure 17. The square of the correlation function, $B_X^2(\rho)$, for delta-function profile, versus $\sqrt{\rho^2 k/4z_o}$ (arbitrary vertical scale).

Substituting the ratio $\sigma_{B_\chi}/B_\chi(0)$ for a sample of length L from Eq. (5.18) in Eq. (5.20), we find

$$\frac{\sigma_S}{S(0)} = \frac{12\sqrt{6}}{5\pi\sqrt{19}}\,\Gamma\left(\frac{1}{6}\right)\,\sin\,\frac{\pi}{12}\sqrt{\frac{.68\,\rho_o}{mL}}\,\left(\frac{\rho_m^{\,2}k}{4z_o}\right)^{11/6}\,, \qquad (5.21)$$

indicating that the relative error in the calculated value of $S(z_o)$ is inversely proportional to the square root of the number of discrete sample points, m, taken in the measured $B_\chi(\rho)$; inversely proportional to the square root of the intensity sample length, L, measured in units of ρ_o; and proportional to $(\rho_m^{\,2}k/4z_o)^{11/6}$.

To give a specific numerical example, we solve Eq. (5.21) for L, and calculate the required L for a ten percent rms error in the integrated profile i.e., $[\sigma_S/S(0) = 0.1]$; $\rho_m^{\,2}k/4z_o = 25$, which according to Eq. (3.12) corresponds to a spatial resolution of $D/z_o = 0.16$; and for 50 sample points in the correlation function. The result is $L/\rho_o = 1.3 \times 10^4$. The standard deviation of the correlation function in this numerical example, obtained from Eq. (5.20), is $\sigma_{B_\chi} = 3 \times 10^{-3}\, B_\chi(0)$.

We now consider application of these results to an experimental situation. First, let us consider the case of a laboratory experiment in which we have grid-generated turbulence in a wind tunnel at a distance z_o from a linear array of photomultipliers. A laser beam propagates through the turbulence. If D is the path length through the turbulence and $D \ll z_o$, the turbulence profile may be approximated by

$$C_n^{\,2}(z) = C_{no}^{\,2}\, D\, \delta(z-z_o)\,,$$

so that the above results for a delta-function profile are applicable. Taking the total propagation path length $z_o = 10^3$ cm, we obtain $\rho_o = \sqrt{4z_o/k} = 0.18$ cm, and hence $L = 2.3 \times 10^2$ cm.

The photomultipliers allow us to record intensity as a function of time at selected points along a line perpendicular to the propagation path. The correlation function can then be calculated by averaging over the time, the signals from pairs of photomultipliers,

$$ {}^{\ell}B_{\chi}(x_i - x_j, T) = \frac{1}{T} \int_0^T [\chi(x_i, t) - \langle\chi\rangle][\chi(x_j, t) - \langle\chi\rangle]\, dt , \qquad (5.22) $$

where

$$ \langle\chi\rangle = \frac{1}{T} \int_0^T \chi(x, t)\, dt . \qquad (5.23) $$

The true correlation function is given by

$$ B_{\chi}(\rho) = \lim_{T \to \infty} {}^{\ell}B_{\chi}(\rho, T) $$

$$ = \lim_{N \to \infty} \frac{1}{N} \sum_{\ell=1}^{N} {}^{\ell}B_{\chi}(\rho, T) . \qquad (5.24) $$

The turbulence is moving across the laser beam with the mean velocity, V, of the wind tunnel. As a consequence, the intensity pattern at the detector array is also moving with velocity V. (This makes the assumption that the changes in the turbulence is negligible in the time it takes to cross the beam, so that the time variation at a fixed point in space is due to convection.) We therefore have,

$$ \chi(x, t) = \chi(x - Vt, 0) , \qquad (5.25) $$

and hence, from Eq. (5.22),

$$ {}^{\ell}B_{\chi}(\rho, T) = \frac{1}{T} \int_0^T [\chi(x - Vt, 0) - \langle\chi\rangle]\ [\chi(x + \rho - Vt, 0) - \langle\chi\rangle] dt $$

$$ = \frac{1}{L} \int_0^L [\chi(x - Vt, 0) - \langle\chi\rangle]\ [\chi(x + \rho - Vt, 0) - \langle\chi\rangle]\, dx \qquad (5.26) $$

where $L = VT$. The time average, which is actually done over a time interval T, is therefore equivalent to a spatial average over the distance $L = VT$. The time interval required for averaging is $T = L/V = 3.4$ sec for $V = 15$ mph $= 660$ cm/sec, $\rho_o = 0.18$ cm, and $L/\rho_o = 1.3 \times 10^4$.

The second case we consider is the same laboratory configuration except that the detector is a photographic film plate which is exposed to the laser beam for a short time (during which the turbulence undergoes a negligible change). This is most easily accomplished using a pulsed laser. A spatial average is performed over the photograph, and if necessary, subsequently, an average over a number of photographs. To make efficient use of the information recorded on the photograph, to obtain a sample of $B_\chi(\rho)$, we can average over all pairs of points whose separation is $\rho = |\vec{\rho}|$, but there is no need to restrict the direction of $\vec{\rho}$ to be parallel to the x-axis as was done for the linear array of photomultipliers just discussed. It would be desirable, for the purpose of calculating the variance of B_χ measured from a single photograph, $\sigma_{B_\chi}^2(\rho, X, Y)$ (X and Y are the sides of a rectangular photograph) to generalize Eq. (2) to two dimensions. This will be done in the future. However, without this generalization, it is still possible to estimate $\sigma_{B_\chi}^2(\rho, X, Y)$. In Fig. 18 we show a photograph with a rectangular grid of points with spacing ρ_o. From each point we draw a semicircle of radius ρ as illustrated. If we neglect edge effects (or, if $\rho \ll X$ and Y) there are XY/ρ_o^2 such semicircles for each value of ρ. From each semicircle we can compute a sample of $B_\chi(\rho)$,

$$\ell B_\chi(\rho) = \frac{1}{\pi\rho} \int_0^\pi [\chi(x, y) - \langle\chi\rangle][\chi(x + \rho\cos\phi, y + \rho\sin\phi) - \langle\chi\rangle]\rho\, d\phi, \quad (5.27)$$

where φ is the polar angle about the center of the semicircle.

Because of the statistical isotropy of the intensity pattern on the photograph, the integral in Eq. (5.27) is equivalent to the integral in Eq. (5.26), with L replaced by $\pi\rho$. From Eq. (5.18), we obtain for the variance of the sample correlation functions obtained from each semicircular arc,

$$\sigma_{B_\chi}^2(\rho >> \rho_o, \pi\rho) = \frac{.68\,\rho_o}{\pi\rho} B_\chi^2(0). \quad (5.28)$$

Because the centers of the semicircles are separated by ρ_o, and there is no duplication of pairs of points (except for the end-points of the

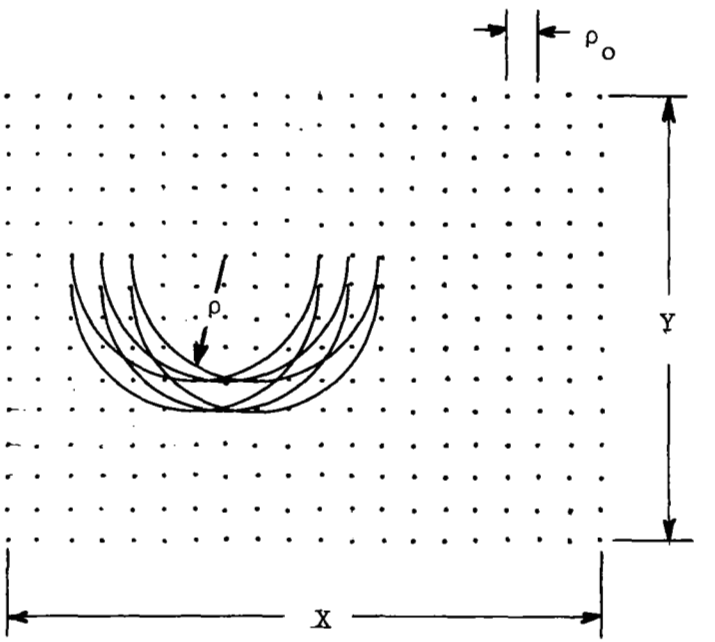

Figure 18. Diagram for estimating the effective sample size of a rectangular photographic intensity record.

semicircles), we obtain essentially independent samples from each arc. If we calculate the average of all the semicircles on the photograph, the variance of this average is Eq. (5.28) divided by the number of semicircles, XY/ρ_o^2,

$$\sigma_{B_\chi}^2(\rho >> \rho_o, X, Y) = \frac{.68\ \rho_o^3}{\pi \rho\ XY}\ B_\chi^2(0)\ . \tag{5.29}$$

If, as above, we require $\sigma_{B_\chi}/B_\chi(0) = 3 \times 10^{-3}$, and take $\rho_o = 0.18$ cm, then the required area of photograph is

$$XY = \frac{.68\ \rho_o^3}{\pi \rho}\ \frac{B_\chi^2(0)}{\sigma_{B_\chi}^2} = 7.3 \times 10^2\ \frac{\rho_o}{\rho} \tag{5.30}$$

Since the inversion is most sensitive to noise at the largest values of ρ used in the integration we calculate the area XY required to have $\sigma_{B_\chi}(5\rho_o, X, Y)/B_\chi(0) = 3 \times 10^{-3}$, which is

$$XY = 1.5 \times 10^2\ \text{cm}^2\ . \tag{5.31}$$

If each photograph is 10 cm^2 in area, 15 photographs are required.

VI. EXPERIMENT

A. General Description

The experimental efforts under this contract have been directed toward verifying the results of the theoretical study of clear-air turbulence detection by optical means. In general the experiment is designed to produce artificial turbulence, illuminate it with a laser beam, photograph the random diffraction pattern produced in the beam, reduce the optical-density-versus-position data to frequency modulated signals on magnetic tape, and from this, calculate the correlation function of Eq. (1.1). We have set up the complete system and have begun to obtain data. This system includes the laser light source, artificial turbulence source, camera and shutter, photodensitometer, associated f.m. equipment, and tape recorder, as well as the use of a suitable computer, digitizer system and associated computer program.

Figure 19 is a flow diagram of the clear-air turbulence detection experiment showing the necessary equipment and processes, including that required for data reduction and computation. The wind tunnel in the diagram is a slow-speed model with optical-glass windows and a 5 hp blower. A photograph of the tunnel is shown in Fig. 20. Preliminary tests were made using a 1 KW heater of approximately 4 square inches cross section substituted for the turbulence source.

The camera, shown in Fig. 21, is used to photograph the diffraction pattern of the laser beam which has passed through the turbulence. The photo transparency thus obtained is the primary data of the experiment. Although only one photo is shown in Fig. 19, actually many will be used to make one profile calculation, as indicated in Sec. V. B. As the diagram in Fig. 19 shows, the range, z_o, between the turbulence and the camera can be varied. This, along with variations in the intensity and type of turbulence will allow us to verify the theory of remote sensing of turbulence profiles.

B. Laser Light Source and Camera

The first experimental efforts were directed toward construction and testing of equipment. The pulsed argon-ion laser shown in Fig. 22, was

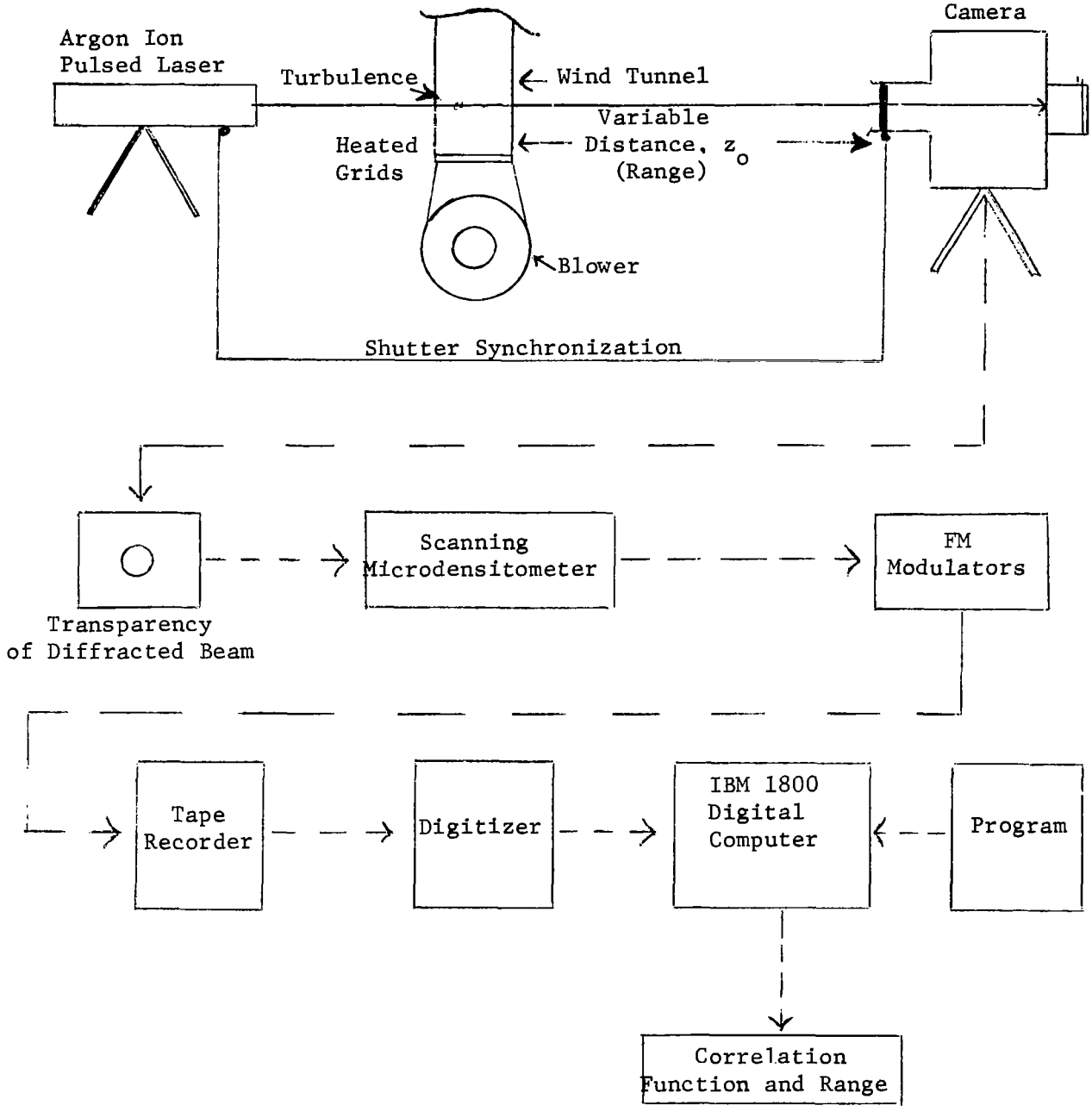

Figure 19. Flow Diagram of Clear-Air Turbulence Experiments

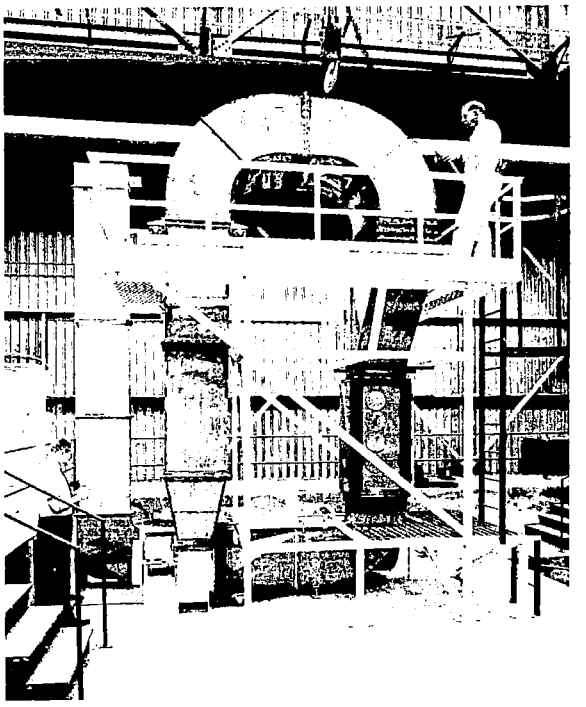

Figure 20. Wind Tunnel

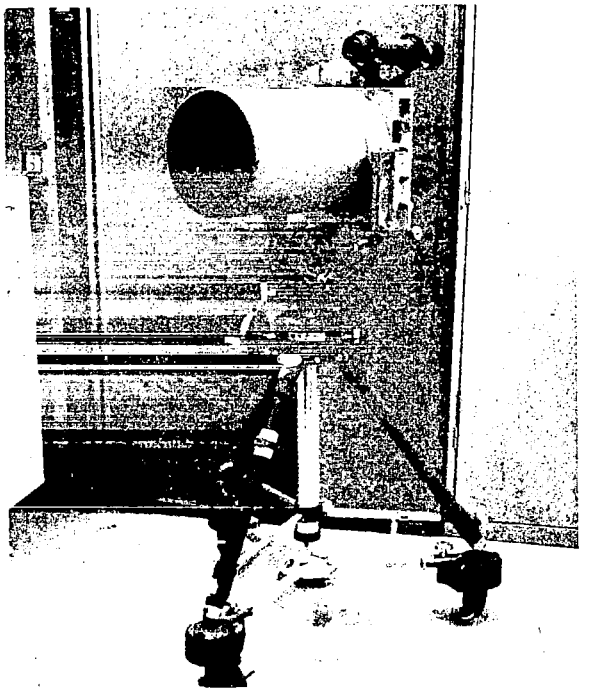

Figure 21. Camera with Synchronized Shutter

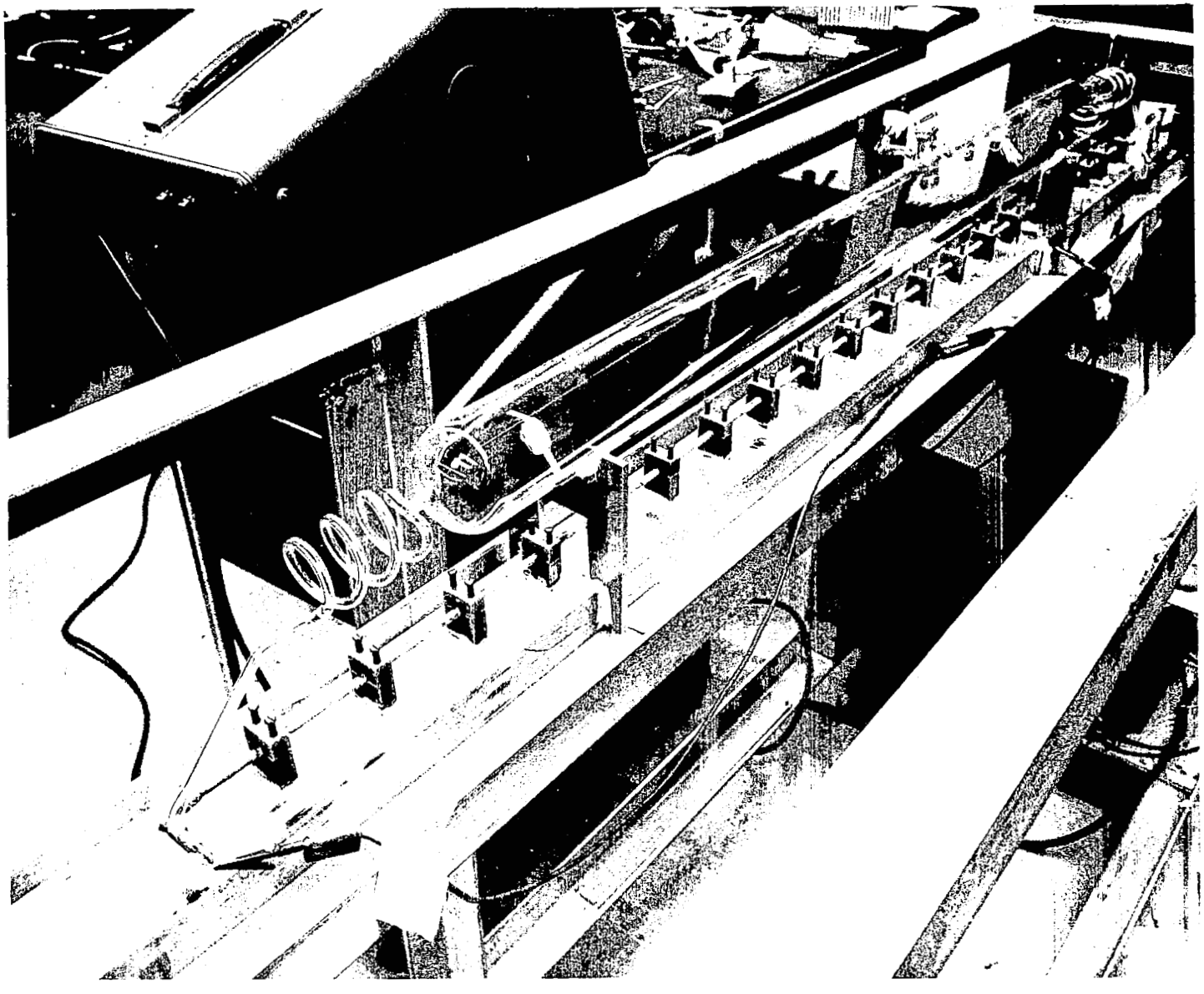

Figure 22. Argon-Ion Laser

tested with a modified aircraft camera and shutter. The lens was removed from the camera and only the synchronized shutter was used. This triggers a single pulse from the argon laser which exposes the film plate. The laser delivers approximately 50 watts peak power with a pulse length of approximately 30 microseconds. This is total power in all colors and all modes. We have not measured single-color, single-mode power. However we can assume that over 30% of the power is in the TEM_{oo} mode at 4880Å. This is more than enough energy to properly expose our film. We have planned several improvements to the system. These include beam scraping, filtering, and an aperture within the laser cavity for mode selection.

Using the optics and camera described in this report, we have photographed various forms of experimentally generated turbulence. Light intensities greater than necessary for proper exposures were obtained, so that neutral density filters were used in the beam for all photographs. At present, we feel that with planned improvements, the light source and optics will meet the requirements of the experiment.

A typical photo of our laser beam after traversing the laboratory-created turbulence is shown in Fig. 23. The granularity or scaly character of the disturbed beam is similar to observations of that produced by natural turbulence at a height of a few meters above the ground. The photo in Fig. 23 was obtained with the laser 13 meters from the film plane, and the turbulence source 1 meter from the laser. This gives a range of 12 meters for this film.

Other photographs, taken at a range of 8 meters, clearly contain a smaller scale size in the intensity pattern as indicated by the theory [Eq. (3.1) predicts scale size $\sim (z_o/k)^{1/2}$].

The beam has also been observed with the laser free-running. In this mode, images of the disturbed beam are observed and integrated by the eye. When observed in this manner, the image loses its granular nature and tends to have dark bands running through the beam. Although this time-integrated effect is interesting, only single-pulse photographs can be used to obtain the correlation function (1.1).

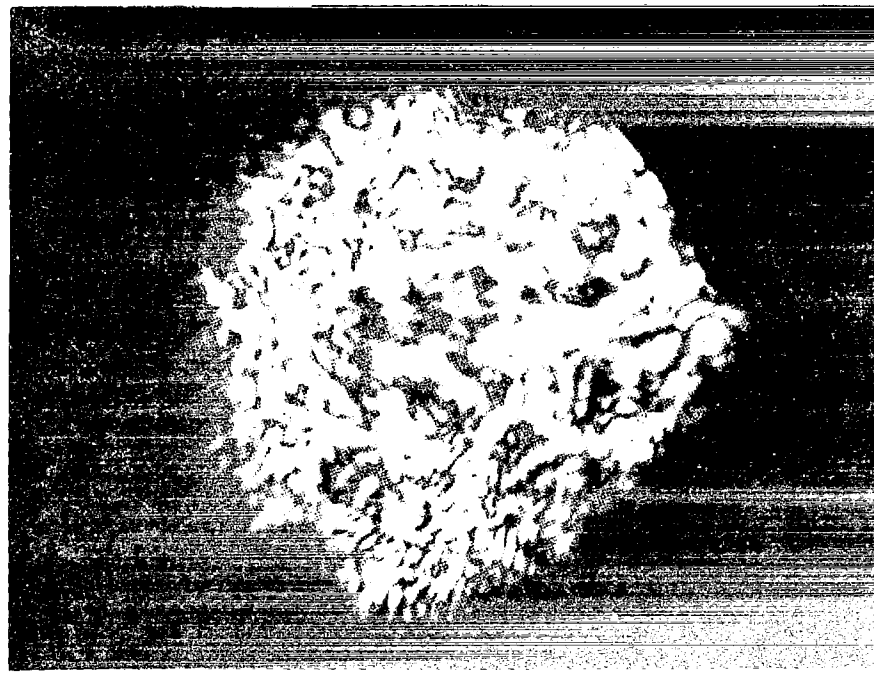

Figure 23. Photograph of laser beam after traversing experimentally generated turbulence

C. Turbulence and Grid Design

Considerable effort has been expended in the study and design of a heated-wire grid for generating turbulence. Our early efforts included use of a 3-kilowatt unidirectional grid and a wind tunnel flow velocity of 50 ft/sec. This arrangement did not create a visible change in the laser beam. The result substantiated a theoretical extrapolation of experimental data,[12] which predicted that a power of about 35 KW would be required for the tunnel as initially set up. It is not possible to obtain 35 KW of electrical power for this purpose at the present test site. Therefore, the wind tunnel velocity was reduced to 11 ft/sec (7.5 miles/hr) by changing the blower drive ratio. At this velocity, the initial 3 KW grid produced visible turbulence when illuminated with the laser beam. In the latter case, actual heating of the flow could be felt when one placed his hand in the operating tunnel.

This unidirectional grid was constructed strictly for power measurements, and the element spacing was too large to give the proper turbulence spectrum. We expect better efficiency and visible diffraction of the beam when we use the proper spacing. The grid we are presently constructing should do this as well as give us the proper turbulence spectrum.

In designing our latest heated grid we have attempted to follow established aerodynamic practice[12] to produce a known turbulence spectrum. In this way we may be able to eliminate the necessity for a hot-wire anemometer study and survey of the turbulence. The filling factor (ratio of blocked area to total area) for the grid was set at 1:5 so that existing data could be used to predict the turbulence spectrum. Scale size was held at approximately 0.10 inch between centers of #22 Nichrome wire.

Figures 24a and b give the important details of the grid's construction. It is designed to take approximately 10 KW maximum. We have shown only one unidirectional grid. The second grid is nearly identical except that the wires are strung across the long dimension of the frame and that the springs are also running in this direction to allow for the thermal expansion of the heated Nichrome wire.

When both grids are installed in the tunnel, the second downstream of the first, we will have a rectangular grid with a power capability of

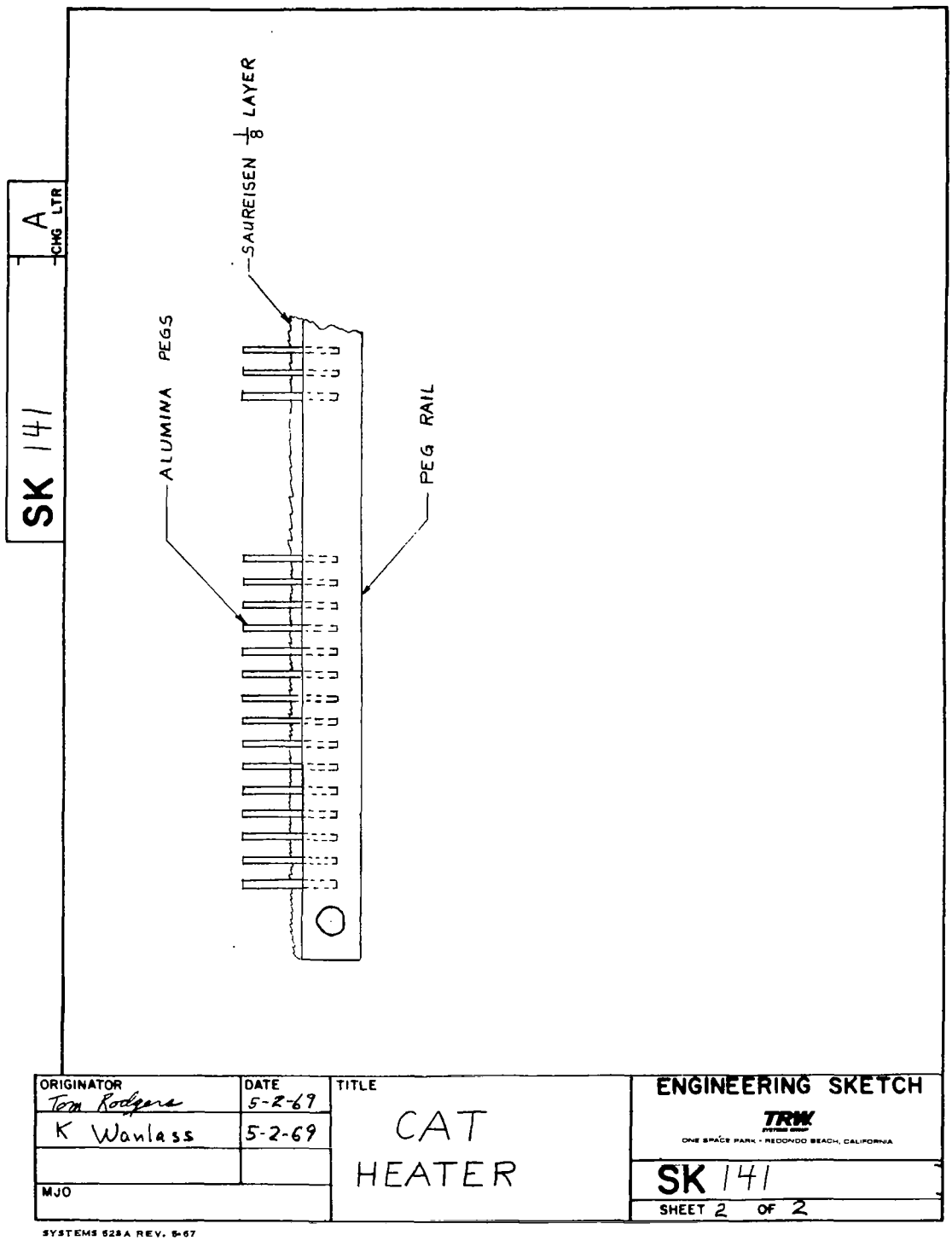

Figure 24a. Turbulence Grid Detail

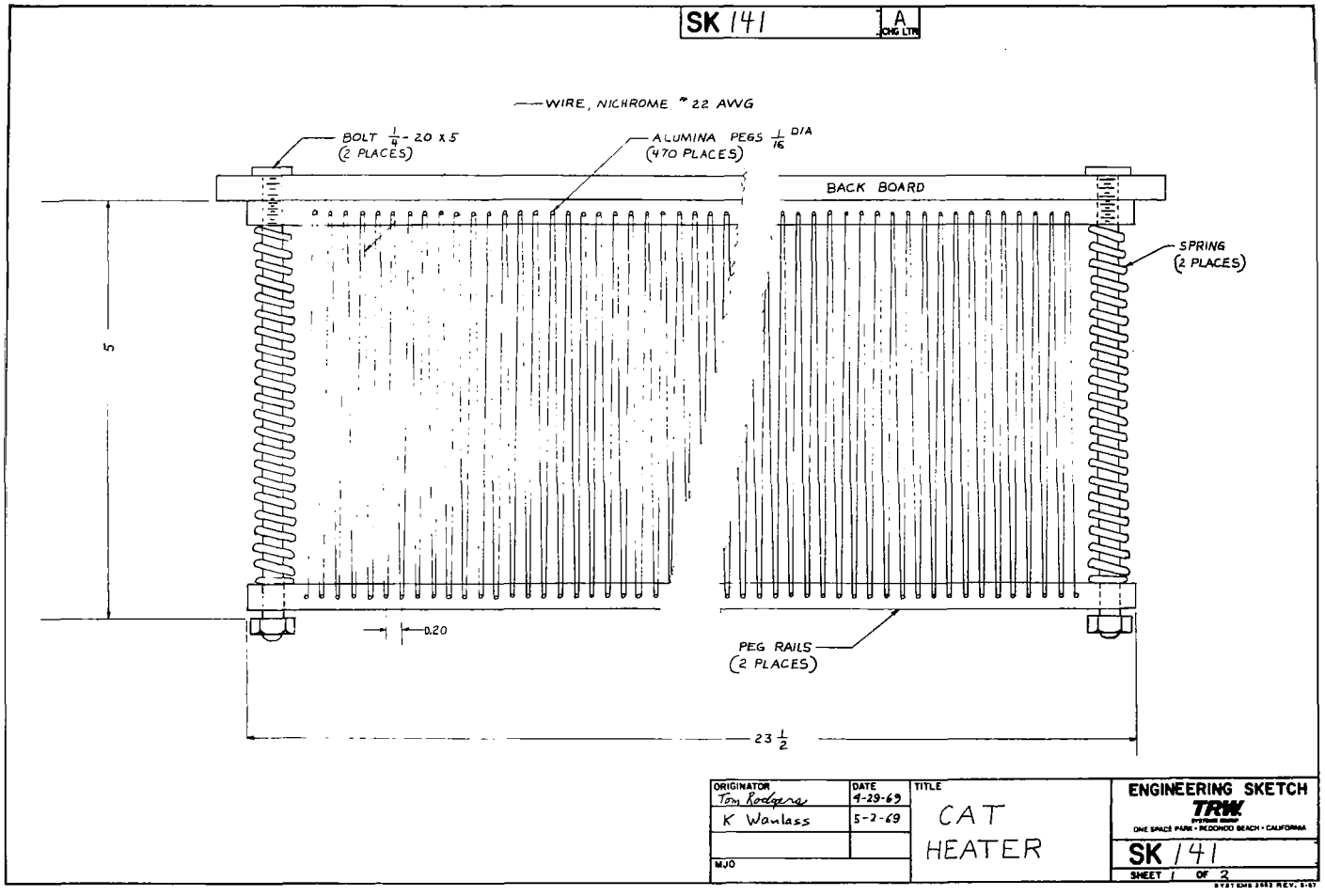

Figure 24b. Turbulence Grid

approximately 20 KW. The lateral displacement of the two unidirectional grids is consistent with previous designs.

D. Computation and Data Reduction

After the film plates were exposed and developed, they were read by means of a microphotodensitometer. The unit which we used had a variable speed drive on the traversing table which slowed when the recording pen was forced to displace quickly. This eliminated pen lag, but complicated the computer program. The negative was traversed 41 times with a spacing between lines of 0.5 mm. The coverage is shown in Fig. 25.

This method of surveying the film plate was used to give us the largest number of independent data points that could be stored in the IBM 1800 computer for the correlation computation. This is important since the results of Sec. V indicate approximately 15 frames will be needed to obtain good range accuracy. Furthermore, it takes about 90 minutes to scan and tape-record a single photo, so that any reduction in the number is a great saving.

Although most of the analytical and theoretical work was and will be done on the CDC 6500 computer, the IBM 1800 was chosen for interpretation of our preliminary data, because we felt that, on account of the 1800's greater accessibility, more could be accomplished on it in a limited time. This expectation was, unfortunately, not realized because of certain unexpected difficulties we encountered in adapting a tape-read subroutine. The 6500 has considerable advantages over the 1800 in memory capacity, programming flexibility, speed, and economy of operation, and will probably be relied on for most of our data processing in the future.

Figure 26 is a block diagram of the system built to measure the photographic data and transfer it to computer tape. The photodensitometer is a Joyce Model MK III C. The voltage-controlled oscillators were Wavetek Model 111's.

The on-off channel was used to indicate regions of valid data to the computer. It was turned off during the return of the table, in order to give an accurate count of the trace and so that spurious data would not be digitized.

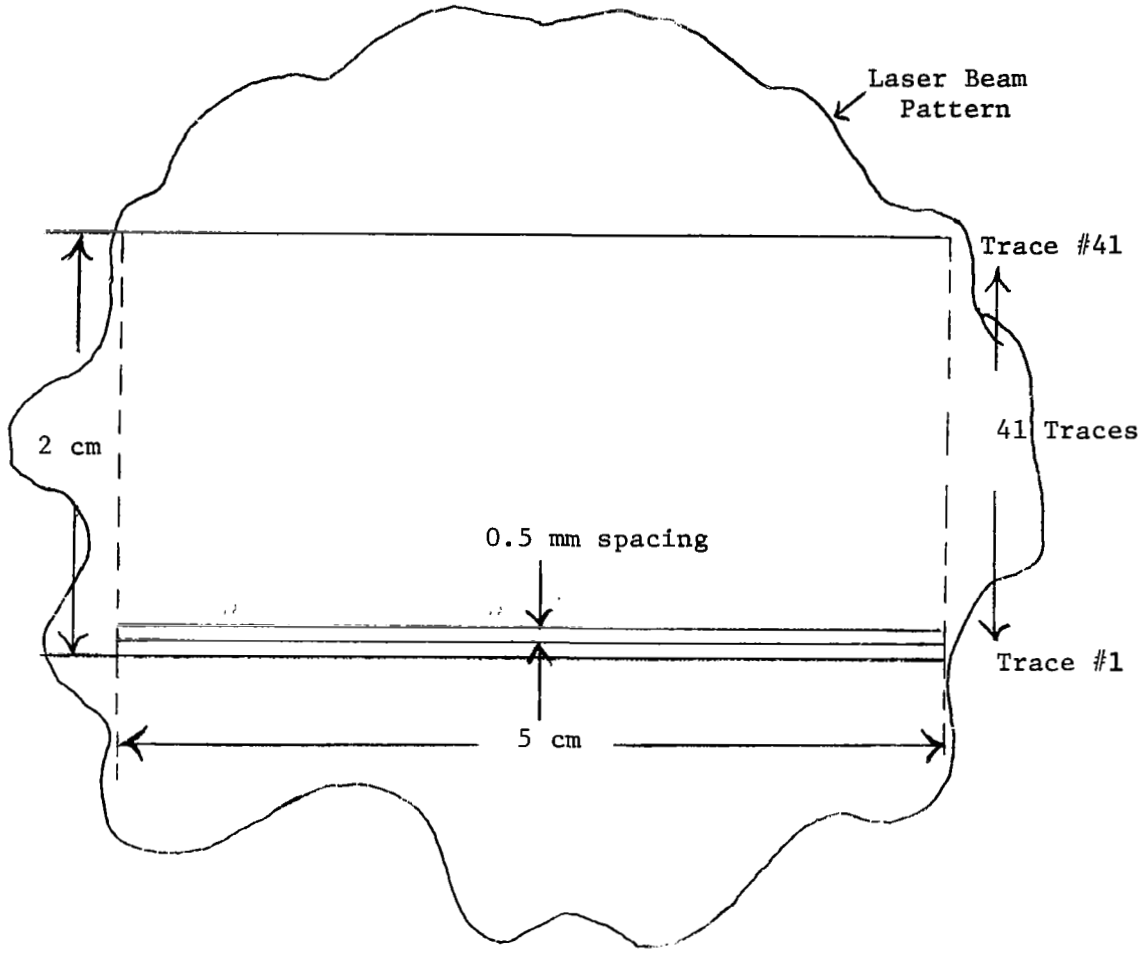

Figure 25. Standard Method for Scanning Film Transparencies

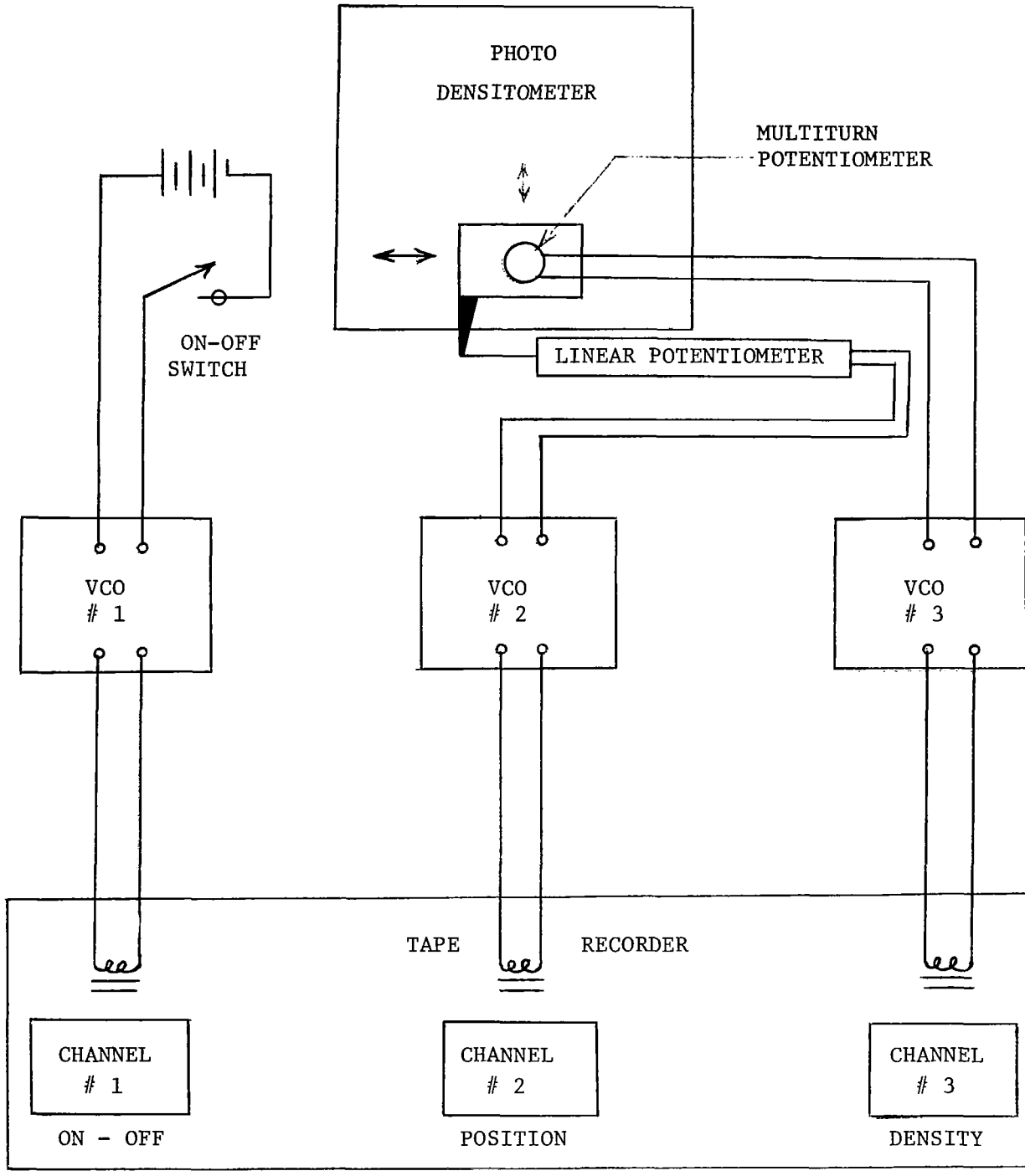

Figure 26. Block Diagram of Densitometer and Tape Recorder.

A linear potentiometer was used to read out the table position, as indicated in the block diagram. The full range of the potentiometer was not used in our initial runs, and greater accuracy if necessary can be obtained by attaching it to the drive arm rather than the film table. The density readout was obtained from a multiturn Helipot. This potentiometer was gear-driven by the pen drive servo. Its deflection can, therefore, be increased by changing the photodensitometer optical wedge. The center frequency for the density and position VCO's was 960 Hertz. The on-off frequencies were 2300 Hz. and 2000 Hz. respectively.

A normal frequency variation for the density was from 886 Hz. for a blocked beam to 1026 Hz. for clear film. For the displacement, the frequency range was from 902 Hz. to 1047 Hz.

During the initial run, a calibration was made for the computer on both the density and the displacement potentiometers. This calibration also insured that the density servo would remain on scale, and that the voltage-controlled oscillators were operating properly.

Figure 27 is a typical photodensitometer trace of a laser beam photo transparency as recorded by the servo driven pen. The transparency used for this trace was almost identical to that used for computer run #1, the only difference being the use of a less intense laser beam (attenuation added) to check for film saturation.

The full trace corresponds to approximately 5 cm on the film transparency. The optical density vs. displacement curve indicates that film saturation is not a problem at this exposure level. If indeed any film saturation does occur, only the center peak could possibly be effected, and it is quite sharp. On the photodensitometer traces used for the three computer runs, the slit width was set at .005 inches (127 microns) and the height was approximately the same. The optical wedges used in the densitometer are quite linear, and we have not corrected for any variation from linearity. However, we do have calibration curves on the wedges which can be used to correct this source of error if necessary.

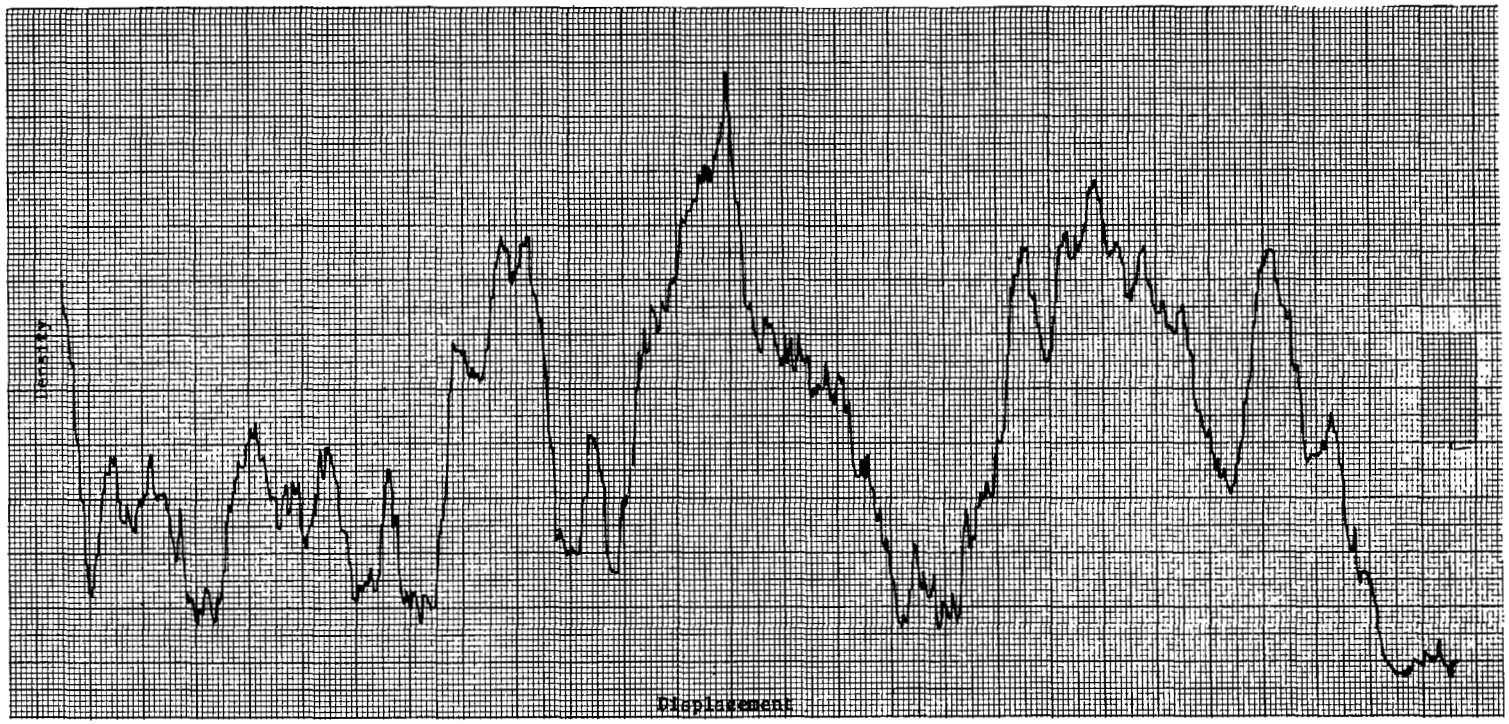

Figure 27. Typical Photodensitometer Trace

We are presently attempting calculations of the range using the initial data taken. Three film-to-tape runs of reasonable quality were made to check out the equipment and the computer program.

Run #1: Made on a photo transparency where the range was 12 meters

Run #2: Made on a photo transparency with a turbulence range of 8 meters

Run #3: Range again was 12 meters but intensity of turbulence was decreased.

The following data processing steps are required:

1. Analog-to-Digital Conversion

The analog tape containing the On-Off signal, the carriage position, and the film density on three separate channels is converted to a 9-track digital tape, suitable for input to the IBM 1800 computer.

2. Interpolation

The digitizing routine (1) samples the analog tape at uniform time increments. However, in order to calculate the correlation function, we require uniform increments of carriage displacement. As described above, the carriage displacement is not a linear function of time. Therefore, an interpolation is done to construct a second digital tape which contains the film density at uniform increments of displacement. The film is sampled at a horizontal spacing of 0.25 mm. This gives approximately 7 samples in the distance $\rho_o = \sqrt{4z_o/k}$. There are 160 sample points per line. There are 41 lines per photograph, with vertical spacing of 0.50 mm.

3. Correlation Computation

The correlation function is calculated in the manner illustrated in Fig. 18. The integral over a semicircle appearing in Eq. (5.17) is approximated by a sum over the sample points between two semicircular arcs with radii differing by 0.25 mm.

4. Profile Calculation

The correlation function is fed into the CDC 6500 and inverted by the program for Eq. (1.13). The resulting S(z) is differentiated to obtain $C_n^2(z)$.

When the computation was attempted, however, it was discovered that the tape-reading routine contained an error. This prevented our completing the calculation. We are currently awaiting an improved version of the tape-reading routine.

VII. CONCLUSIONS AND FUTURE PLANS

We have investigated the practicality of applying the integral transform of the logarithmic-amplitude correlation function given in Eq. (1.10), and the more rapidly converging form given in Eq. (1.13), for remote sensing of atmospheric turbulence profiles. With these equations the turbulence profile, $C_n^2(z)$ can be determined uniquely by calculating an integro-differential transform of the correlation function, $B_\chi(\rho)$. The determination of $C_n^2(z)$ is exact only if $B_\chi(\rho)$ is known exactly over the entire range $0 < \rho < \infty$. This, of course, is never true in practice, since, if $B_\chi(\rho)$ is obtained from a measurement there is always noise present.

We have begun a study of the effect of practical limitations in measurement of the correlation function on the profile calculation. A computer program has been written for performing the mathematical operations of Eqs. (1.10) and (1.13) on correlation functions. This requires the calculation of confluent hypergeometric functions of imaginary argument since these are not available in tables. A number of important practical questions have been answered by applying the computer program to the correlation function of a delta-function turbulence profile, $C_n^2(z) = A\delta(z-z_o)$. This is the mathematical representation of a thin layer of turbulence for which the observer-to-turbulence distance is much greater than the layer thickness, and is a convenient profile for studying the properties of Eqs. (1.10) and (1.13). A computer calculation was made to obtain the delta-function profile correlation function, which is also expressible in terms of a confluent hypergeometric function of imaginary argument.

The correlation function $B_\chi(\rho)$ thus calculated (Fig. 1), and in fact any correlation function, according to Eq. (1.11), approaches zero rapidly as $\rho \to \infty$. Hence, for separations greater than some value $\rho = \rho_m$, any experimental measurement of $B_\chi(\rho)$ will be overshadowed by noise. In a practical application it will thus be necessary to truncate $B_\chi(\rho)$ at some value $\rho_m < \infty$. We have studied the effect of truncation by applying Eqs. (1.10) and (1.13) to the correlation function calculated for a delta-function profile whose correlation function is truncated at ρ_m. The result of the computation is that, as one

would expect, the inversion formulas predict a finite layer thickness D (rather than the zero thickness of the delta function) if ρ_m is not infinite. The predicted layer thickness is found to be related to ρ_m and the distance, z_o, to the layer by Eq. (3.12), $D = 16\, z_o^2/\rho_m^2 k$. This result is applicable to any arbitrary profile, if D is interpreted as the size of the smallest scale variation in $C_n^2(z)$ near $z = z_o$ that can be resolved.

To give a specific numerical example, let us say we are interested in calculating $C_n^2(z)$ in the tropopause by using ground-based stellar scintillation measurements to obtain $B_\chi(\rho)$. The distance is $z_o = 8$ km. If we wish to distinguish features in the profile larger than 1 km, by applying Eq. (3.12), we obtain $\rho_m = 4z_o/\sqrt{kD} = 30$ cm. The correlation function can therefore be measured within the desired spatial resolution by using an array of telescopes in which the maximum separation required between a pair of telescopes is 30 cm.

The correlation function $B_\chi(\rho)$ is sampled by the telescope array at a discrete set of points ρ_i. The integral transforms (1.10), (1.13) [or (3.10), which is the specialization of (1.13) to the delta-function case] are approximated by sums in the computer calculation. Each term in the sum contains the correlation function at one sample point. We can thus predict the number of sample points required by studying the effect of varying the number of terms used in the computer program. The results are shown in Fig. 10 for $\rho_m^2 k/4z_o = 100$ (for which $D = .04z_o$). The figure indicates that as the range of z over which the profile is calculated increases, the number of sample points in the correlation function must increase. For example, if we calculate the profile from Eq. (3.10) in the range $0.9z_o < z < 1.2z_o$, 100 sample points suffice, whereas if we calculate it in the larger range $0.2z_o < z < 1.2z_o$, 1000 points are needed. The number of telescopes required is much less than these numbers. (The minimum number of telescopes that can be arranged in a straight-line array such that the separation between different telescopes are integral multiples 1, 2, ... m can be determined.[13] For example, to obtain separations 1, 2, ... 45, only eleven telescopes are required, spaced with successive separations: 18, 1, 3, 9, 11, 6, 8, 2, 5, 28.) If we relax the resolution requirement at z_o (i.e., $D > 0.04z_o$), fewer points will be needed. A study of the computer calculations for various

numbers of sample points (a selection of which is shown in Figs. 7-9) indicates that with a different arrangement of sample points we can improve the calculation, for a given number of sample points. In all our calculations we have positioned the sample points so that they are uniformly spaced in the variable ρ^2. This makes the density of points greater at large ρ. In the calculations using a smaller number of sample points (e.g., Fig. 8d) the calculation is seen to break down at small ρ. We will therefore repeat our calculations using other spacing arrangements which place relatively more points at small ρ. We will first try uniform spacing in ρ. We expect this to increase the accuracy of the profile calculation for a given number of sample points. This will, in turn, reduce the number of telescopes required.

For studying the spatial resolution, the delta-function profile was the obvious choice. It places all the turbulence at a single range, z_o, thus allowing us to see clearly the range dependence of the inversion technique. It has zero width, so that the width of the calculated profile is a direct measure of the loss in spatial resolution introduced by the inversion calculation. Because of its singular nature, it is also the most difficult inversion to perform. That is, we should expect slower convergence of the transforms (1.10) and (1.13) for inversion of $B_\chi(\rho)$ for a delta-function profile than any other $B_\chi(\rho)$, and if the calculation converges in this case, it should converge for any other profile. It is of interest, however, to apply the inversion formulas to the correlation function of a smooth turbulence profile, which more closely resembles those expected in practice.

We have obtained an analytic expression for the correlation function of turbulence profiles of the form $C_n^2(z) \sim (\mu z/z_o)^\mu e^{-\mu z/z_o}$, shown in Fig. 11. These profiles have their maximum value at $z = z_o$ and have increasingly narrower width as μ increases. The expression for the corresponding correlation function (4.14) is in terms of a generalized hypergeometric function. We have presented the computer calculation of this $B_\chi(\rho)$ for $\mu = 1, 2$ and 4 in Figs. 12a, b, c, which were obtained using the power series for the hypergeometric function. (For larger μ the power series calculation breaks down and it is necessary to use asymptotic expansions for the hypergeometric functions which are apparently not available, but we hope to derive in the future.) Comparing the correlation functions in Figs. 12a, b, c with the delta-function

correlation in Fig. 1, we find comparatively little oscillation for large ρ in the former.

We have inverted these three correlation functions utilizing the inversion formulas (1.10) and (1.13) and obtain the results shown in Figs. 14 - 16. We find, as expected, that the integrals converge much more rapidly (for smaller ρ_m) than in the delta-function case. We also find that the improved convergence of (1.13) (lower curves) compared to (1.10) (upper curves) is more significant when applied to the smooth-profile case.

Improved convergence is obtained with Eq. (1.13) by adding a first-order approximation to the portion of the integral in Eq. (1.10) from ρ_m to ∞. This procedure works better for the smooth correlation functions because it is better able to approximate the tail of the correlation function, which has less of the oscillatory behavior of the delta-function case. We anticipate that measured correlation functions of real turbulence profiles will more closely resemble Figs. 12a, b, c than Fig. 1 and that the added complication of using Eq. (1.13) rather than (1.10) will pay off. We have not yet written the computer program for Eq. (1.12) which can be used to calculate the correction term in Eq. (1.13) directly from an integral transform of $B_\chi(\rho)$ but will do so in the near future.

Equations (5.2) - (5.5), relate the error, $\sigma_s = \left(\langle(\delta s)^2\rangle\right)^{\frac{1}{2}}$, in the calculated integrated profile to the autocorrelation function $\langle N(\rho_i)\, N(\rho_j)\rangle$, of the noise, $N(\rho_i)$, in a measured logarithmic - intensity correlation function. The integrals in Eq. (5.2) are evaluated explicitly when the noise autocorrelation has the form $\langle N(\rho_i)N(\rho_j)\rangle = \nu^2(\rho_i)\delta_{ij}$, i.e., when the noise at two distinct sample points is uncorrelated. For this type of noise, we thus have the relation (5.13) or (5.13') which indicate that σ_s is proportional to $\nu(\rho_m)$, inversely proportional to the square root of the number of sample points, m, and proportional to $\left(\rho_m^2 k/4z\right)^{11/6}$. Because of the strong dependence of σ_s on ρ_m it is important in any application to have ρ_m as small as possible [subject to the constraint that ρ_m be large enough to obtain the desired spatial resolution determined by Eq. (3.12)]. The strong dependence of σ_s on m occurs because the kernel function in Eq. (1.10) or (1.13) (shown in Fig. 2) increases with increasing ρ and hence magnifies the effect of the noise in $B_\chi(\rho)$ at large ρ.

Equation (5.14) relates ${}^{\ell}B_{\chi}$ to the spatial extent, L, of the intensity sample used in a measurement of $B_{\chi}(\rho)$. Combined with Eq. (5.13), in the special case of delta-function turbulence, we obtain Eq. (5.21) which indicates that σ_s is inversely proportional to the sample length, L. If we consider the case, discussed above, of sensing turbulence in the tropopause at a distance of 8 km, assuming a velocity of about V = 150 mph in the tropopause, we will require an averaging time (T = L/V) of about 10 seconds in order to have the rms error in the calculated profile equal to 10%, i.e., $\sigma_s = 0.1$.

We have assumed that the noise occurring in the measurement of $B_{\chi}(\rho)$ has an autocorrelation function of the form (5.6). This assumption must break down if the number of sample points, m, becomes too large. Further study will be required to determine the range of m over which this assumption is justified or what modification is necessary to Eq. (5.21) if we are outside this range. We also must extend our results to other sources of measurement noise (stray light, photomultiplier noise, etc.).

We have set up a laboratory experiment to verify the predictions of the theoretical study. The experimental arrangement consists of a wind tunnel fitted with a heated-wire grid for generating turbulence, a laser light source, and a photographic system for recording the random intensity pattern which is induced in the laser beam by passage through the turbulence. The photograph is scanned by a photodensitometer and the correlation function calculated using the resultant data and a digital computer.

We do not yet have a satisfactory operational heated-grid, but have made preliminary photographs using a small heater as the turbulence source. We have scanned these photographs with the densitometer and written most of the program for obtaining the correlation function from the data. We have, however, encountered difficulties with a tape-read computer routine and have been unable to complete the calculation. We hope to overcome this difficulty in the near future. In addition, we expect to have the heated-grid installed in the wind tunnel and to obtain additional photographs for analysis.

REFERENCES

1. A. Peskoff, "Theory of Remote Sensing of Clear-Air Turbulence Profiles," J. Opt. Soc. Amer. 58, 1032-1040 (August 1968) Eq. (20).

2. V. I. Tatarski, "Wave Propagation in a Turbulent Medium," McGraw-Hill Book Company, New York, 1961.

3. M. Abramowitz and I. A. Stegun, "Handbook of Mathematical Functions," NBS Appl. Math. Ser. 55, U. S. Dept. Commerce, June 1964, Chapter 13.

4. Ref. 1, Eqs. (22)-(24).

5. Ibid., Eq. (A5).

6. Ref. 3, formula 13.1.2.

7. Ibid., formula 13.5.1.

8. W. Grobner and N. Hofreiter, Integraltafeln, Zweiter Teil, Bestimmte Integralen, Springer-Verlag, Vienna and Innsbruck, 1950, p. 196 formula #1.

9. A. Erdelyi, ed., Tables of Integral Transforms, Vol. II, McGraw-Hill Book Co., New York, 1954, p. 24, formula #2.

10. K. Pearson, "Tables of the Incomplete Gamma-Functions," Cambridge Univ. Press, 1951.

11. J. S. Bendat, "Principles and Applications of Random Noise Theory," New York, John Wiley and Sons, Inc., 1958, Chapter 7.

12. R. Mills, N. A. C. A. TN 4288, August 1958

13. J. Leech, "On the Representation of 1, 2, ... n by Differences," J. London Math. Soc. 31, 160 (1956).